5-2018

Parametric Study of a 7◦ Half-Angle Cone with Highly-Swept Fins at Mach 6

Franklin D. Turbeville
Purdue University

PARAMETRIC STUDY OF A 7° HALF-ANGLE CONE WITH HIGHLY-SWEPT FINS AT MACH 6

A Thesis

Submitted to the Faculty

of

Purdue University

by

Franklin Drew Turbeville

In Partial Fulfillment of the

Requirements for the Degree

of

Master of Science in Aeronautics and Astronautics

May 2018

Purdue University

West Lafayette, Indiana

THE PURDUE UNIVERSITY GRADUATE SCHOOL
STATEMENT OF THESIS APPROVAL

Dr. Steven Schneider

School of Aeronautics and Astronautics, Purdue University

Dr. Sally Bane

School of Aeronautics and Astronautics, Purdue University

Dr. Bradley Wheaton

Johns Hopkins University Applied Physics Laboratory

Approved by:

Dr. Weinong Chen

Head of the School Graduate Program

To Amy, Trixie, Gracie, my family, old cars and new cars.

ACKNOWLEDGMENTS

I would like to thank my advisor Dr. Steven Schneider for guidance on my research. I also thank my committee members Dr. Sally Bane and Dr. Bradley Wheaton. Funding for this project was provided by the Office of Naval Research under Grant N00014-16-1-2452.

Machinists Robin Snodgrass, Jim Younts, and Jerry Hahn were invaluable and made everything I accomplished possible. Their knowledge and assistance is especially helpful when the window gets stuck in the tunnel, vacuum pumps begin to smoke, things whistle that should not, and screws get stuck in models.

Thanks to Neal Bitter at Sandia National Labs for finding the time to work with me. Thanks to Anthony Knutson and Dr. Graham Candler at the University of Minnesota for their high fidelity computations. Thanks to Dr. Helen Reed and Daniel Mullen for providing me with computations that informed my results. My fellow lab members have been valuable as distractions from what I should actually be doing: Brandon Chynoweth, Greg McKiernan, Josh Edelman, Cameron Sweeney, Katie Gray, Mark Wason, Varun Viswanathan, and Phil Portoni. As my productivity quadruples after I move to Dallas, I will think fondly on the time wasted on pointless arguments. Finally, thanks to Scott Gleason and Liz Benitez for joining our lab. I look forward to working with you over the next few years.

TABLE OF CONTENTS

Page

LIST OF TABLES vii

LIST OF FIGURES ix

SYMBOLS xvii

ABBREVIATIONS xix

ABSTRACT xx

1 INTRODUCTION 1
- 1.1 Corner Flow and Shock/Boundary-Layer Interaction 1
- 1.2 Laminar-Turbulent Transition 2
- 1.3 Quiet Tunnels 3
- 1.4 Fin-Cone Geometry 4
- 1.5 Overview of Experiments 5

2 REVIEW OF LITERATURE 6
- 2.1 Axial Corner Flow 6
- 2.2 Glancing Shock/Boundary-Layer Interaction 15
- 2.3 Fin Bluntness Effects 20
- 2.4 Fin Sweepback Effects 22
- 2.5 Fin-Cone Experiments 24

3 FACILITY, MODELS, AND INSTRUMENTATION 34
- 3.1 Boeing/AFOSR Mach-6 Quiet Tunnel 34
  - 3.1.1 Tunnel Condition Measurement and Computation 35
  - 3.1.2 Run Characteristics 37
- 3.2 Fin-Cone Models 38
  - 3.2.1 Single-Fin Model 38
  - 3.2.2 Three-Fin Model 39
- 3.3 Model Instrumentation, Setup, and Data Reduction 44
  - 3.3.1 PCB Fast Pressure Transducers 44
  - 3.3.2 Schmidt-Boelter Heat Transfer Sensors 45
  - 3.3.3 Oscilloscopes 45
  - 3.3.4 Temperature Sensitive Paint 46
  - 3.3.5 TSP Processing 47
  - 3.3.6 Typical Experimental Setups 51

4 RESULTS AND DISCUSSION 56

Page

4.1 General Flow Characteristics . . . 56
4.2 Quiet vs. Noisy Flow . . . 58
4.3 Effect of Reynolds Number . . . 60
4.3.1 TSP Data Over a Small Range of Reynolds Numbers . . . 60
4.3.2 Trouble Inferring Heat Transfer on the Fin and TSP Limitations 64
4.3.3 Pressure Fluctuation Data as the Streaks Spread Over the Sensors 68
4.3.4 TSP Data at Higher Reynolds Number . . . 74
4.4 Effect of Nose Bluntness . . . 76
4.4.1 TSP Data for Three Nosetip Radii . . . 76
4.4.2 Pressure Fluctuation Data for Three Nosetip Radii . . . 82
4.5 Fin Sweep . . . 89
4.5.1 Shock Attachment at the Fin Leading Edge . . . 89
4.5.2 TSP Data for Fin Sweeps of 70° and 75° . . . 91
4.5.3 Pressure Fluctuation Data for Fin Sweep of 70° and 75° . . . 95
4.6 Fin Bluntness . . . 100
4.6.1 TSP Data for Three Fin Leading Edge Radii . . . 100
4.6.2 Pressure Fluctuation Data for Three Fin Leading Edge Radii . 103
4.7 Pressure Fluctuations Far from the Fin Interaction Region . . . 106
4.8 Angle of Attack . . . 107
4.9 Comparison with Stability Analysis . . . 111

5 SUMMARY . . . 115
5.1 Future Work . . . 116

REFERENCES . . . 119

A Model Drawings . . . 123
A.1 Single-Fin Model . . . 123
A.2 Three-Fin Model . . . 126

B Data Reduction Codes . . . 132
B.1 PCB Code . . . 132
B.2 TSP Slicing Code . . . 138

C Sensor Calibrations and Locations by Entry . . . 143
C.1 Entry 1 . . . 143
C.2 Entry 2 . . . 146
C.3 Entry 3 . . . 149
C.4 Entry 5 . . . 152
C.5 Entry 6 . . . 155
C.6 Entry 7 . . . 158

D Tunnel Conditions and Model Configurations . . . 161

APPENDICES

LIST OF TABLES

Table Page

3.1 Tested fin-cone configurations. 43

4.1 Percent RMS pressure fluctuations for PCB1. 69

4.2 Percent RMS pressure fluctuations for PCB2. 70

4.3 Percent RMS pressure fluctuations for PCB3. 72

4.4 Percent RMS pressure fluctuations for all sensors in the corner region at a unit Reynolds number of 12.4 x 10^6 m^{-1}. 75

4.5 RMS pressure fluctuations ($\frac{P'_{RMS}}{P_{TM}}$) for three nosetip radii and 75° fin sweep. 84

4.6 RMS pressure fluctuations ($\frac{P'_{RMS}}{P_{TM}}$) for three nosetip radii and 70° fin sweep. 86

4.7 RMS pressure fluctuations ($\frac{P'_{RMS}}{P_{TM}}$) for two sweep angles and a sharp nosetip. 97

4.8 RMS pressure fluctuations ($\frac{P'_{RMS}}{P_{TM}}$) for two sweep angles and a 1 mm radius nosetip. 100

4.9 CFD simulation conditions 111

C.1 Entry 1 sensor positions and sampling rates. 144

C.2 Entry 1 sensor calibrations. 145

C.3 Entry 2 sensor positions and sampling rates. 147

C.4 Entry 2 sensor calibrations. 148

C.5 Entry 3 sensor positions and sampling rates. 150

C.6 Entry 3 sensor calibrations. 151

C.7 Entry 5 sensor positions and sampling rates. 153

C.8 Entry 5 sensor calibrations. 154

C.9 Entry 6 sensor positions and sampling rates. 156

C.10 Entry 6 sensor calibrations. 157

C.11 Entry 7 sensor positions and sampling rates. 159

C.12 Entry 7 sensor calibrations. 160

Table Page

D.1 Entry 0 run matrix. 162
D.2 Entry 1 run matrix. 162
D.3 Entry 2 run matrix. 162
D.4 Entry 3 run matrix. 163
D.5 Entry 5 run matrix. 163
D.6 Entry 6 run matrix. 163
D.7 Entry 7 run matrix. 164

LIST OF FIGURES

Figure Page

1.1 Damage due to shock impingement on the X-15 pylon [1]. 2

1.2 Noise radiated from the turbulent boundary layer on a cone at Mach 4.31 [3, 6]. Laminar regions do not show the same radiated noise. 4

1.3 Tested fin-cone geometry with blunt, highly-swept fins. 5

2.1 Shock structure in an axisymmetric corner formed by two wedges. Figure redrawn from Charwat and Redekopp [12]. 7

2.2 Corner flow structure at Mach 3.17 (Re = 1.75 x x 10^5 in^{-1}), redrawn from Watson and Weinstein [13]. Possible vortex where inner shock impinges on the boundary layer. 8

2.3 Corner flow structure at Mach 20.3 (Re = 14.17 x 10^6 m^{-1}). Structure is similar to Mach 3, however, it is distorted by large vortices and thick boundary layers. Redrawn from Watson and Weinstein [13]. 9

2.4 Asymmetry produces a shock structure distorted from the axisymmetric case but maintaining many of the basic features. The inner shock on the interference wedge approaches the two-dimensional shock of the base wedge. Redrawn from Charwat and Redekopp [12]. 10

2.5 Single triple point and two vortices seen by Cooper and Hankey for a wedge-plate axial corner. Redrawn from Cooper and Hankey [14]. 11

2.6 Reexamination of the oil flow data replaces the initial finding of two vortices with this interpretation of a secondary vortex. Redrawn from Korkegi [15]. 11

2.7 Flowfield constructed with four separations and reattachments corresponding with measured peaks in heating (Re = 15 x 10^6 m^{-1}). Figure redrawn from Papuccuoglu [16]. 13

2.8 A laminar boundary layer will have a larger increase in heating over theoretical flat plate values than a turbulent boundary layer [17]. This is due to separation being more likely in the laminar interaction and the subsequent heating due to reattachment. 13

Figure Page

2.9 Lateral extent of the interaction is greater for laminar interactions. The oil accumulation line approaches the turbulent case as the boundary layer transitions. Figure redrawn from Korkegi [19]. 15

2.10 Example of glancing SBLI experimental model. A wedge is mounted on a flat plate with an existing fully-developed boundary layer. The inviscid shock wave interacts with the boundary layer. 16

2.11 Attached flow field redrawn from Kubota and Stollery [25]. 17

2.12 Separated flow field redrawn from Kubota and Stollery [25]. 17

2.13 Lambda shock and stream tube observed by Alvi and Settles [26]. Figure redrawn from Stollery [23]. 19

2.14 Horseshoe vortices formed by separation of boundary layer ahead of a blunt fin redrawn from Kaufman et al. [28]. 20

2.15 Non-dimensional extent of separation at the leading edge decreases as D/δ increases. Figure redrawn from Figure 64 in Fomison [29]. 21

2.16 Increasing sweep significantly reduces the maximum heat transfer in an axial corner. Data presented taken from Figure 10 in Möllenstädt [30]. . . 22

2.17 Sweep reduces the strength of the shock-shock interaction at the fin leading edge. Taken from Figure 4 in Bushnell [32]. 24

2.18 Side view of isoheating contours at Re = 4.5 x 10^6 ft^{-1} shows that the heating levels are much reduced for both the fin and cone surfaces. Values shown are heat transfer coefficients (h x 10^3 BTU/ft^2-sec-°R). Figure taken from Figures 4 and 6 in Gillerlain [36]. 26

2.19 Top view of isoheating contours at Re = 4.5 x 10^6 ft^{-1} shows that the heating levels are much reduced for cone surface. The lateral extent of the heating is much less for the swept fin than the unswept fin. Values shown are heat transfer coefficients (h x 10^3 BTU/ft^2-sec-°R). Figure taken from Figures 5 and 7 in Gillerlain [36]. 26

2.20 Pressure on cone surface upstream of the fin normalized by the pressure for a straight cone at Re = 26 x 10^6 ft^{-1}. The peak in pressure 2D upstream of the the unswept fin indicates a shock-induced separation upstream of the fin. No such peak is seen for the swept fin. Figure redrawn from Gillerlain [36]. 27

2.21 Top view of fin mounted on the cone. The fin is outlined in blue to highlight the wedge cross section near the front of the fin. Image taken from Figure A.10 in Abney and Rochlitz [37]. 28

Figure Page

2.22 Side view of fin mounted on the cone. The fin is outlined in blue to highlight the sweep and leading edge of the fin. Image taken from Figure A.11 in Abney and Rochlitz [37]. 29

2.23 Surface heat transfer measurements indicated hot streaks on the cone and fin surface. The streak pattern is significantly different between quiet and noisy flow at a similar Reynolds number. Images taken from Figures 16 and 17 in Berridge et al. [8]. 30

2.24 Schematic of the 73° sweep fin. Figure taken from Figure 36 in Chynoweth et. al [38]. 31

2.25 Heat transfer for the cone with the 73° sweep fin at a unit Reynolds number of 9.68 x 10^6 m^{-1}. Figure taken from Figure 4 in Chynoweth et. al [7]. . . 32

2.26 Pressure fluctuation power spectra for the sensor near the streak with a 78° sweep fin. Figure taken from Figure 8 in Chynoweth et. al [7]. 33

2.27 Pressure fluctuation power spectra for the sensor near the streak with a 73° sweep fin. Figure taken from Figure 9 in Chynoweth et. al [7]. 33

3.1 Schematic of the BAM6QT. 34

3.2 Example contraction Kulite calibration from Entry 5. 37

3.3 Example hot film and stagnation pressure trace for a max quiet run at 170 psia intial stagnation pressure. Spikes near 1.5 seconds are turbulent bursts. 38

3.4 Schematic of the single-fin model designed by Abney and Rochlitz [37]. The model is a 7° half-angle cone with a sharp nosetip. One fin was tested with R_{LE} = 0.175" and 75° sweep. Dimensions are in inches. 40

3.5 Schematic of the three-fin model. The model is a 7° half-angle cone with interchangeable nosetips. Six fins were tested with variable leading edge radius and sweep. Dimensions are in inches. 40

3.6 Nosetip radii measured with Moticam 3 microscope camera. 42

3.7 Model ready to install in tunnel with TSP applied. 47

3.8 Example TSP image of the three-fin model. The patch chosen for calibration is indicated by a red square. 49

3.9 Example thermocouple heat transfer trace shown in black. Red triangles are the points chose for calibration. 50

3.10 Example linear fit of heat transfer data. 50

3.11 PCBs around the azimuth used for aligning during Entry 6. 52

Figure Page

3.12 Model alignment using the second-mode frequency and the fine angle of attack adapter. 53

3.13 Typical camera and model set up for 0° angle of attack. 54

3.14 The camera and model set up for 4° angle of attack with the fin on the windward ray. 55

3.15 The camera and model set up for 4° angle of attack with the fin on the yawside. 55

4.1 Typical TSP image of the fin-cone flowfield (Run 109, unit Re = 12.4 x 10^6 m^{-1}). Three-fin model shown with R_{LE}=1/8", 75° fin sweep, and a sharp nosetip. Flow is from right to left. 56

4.2 Quiet flow at Re = 8.69 x 10^6 m^{-1} (Run 028). Single-fin model shown with R_{LE}=0.175", 75° fin sweep, and a sharp nosetip. 59

4.3 Noisy flow at Re = 8.69 x 10^6 m^{-1} (Run 032). Single-fin model shown with R_{LE}=0.175", 75° fin sweep, and a sharp nosetip. 59

4.4 Cone streaks spread as the Reynolds number increases from 6.02 x 10^6 m^{-1} to 8.12 x 10^6 m^{-1} in quiet flow. Three-fin model shown with R_{LE}=1/8", 75° fin sweep, and a sharp nosetip. 61

4.4 (cont'd) Cone streaks spread as the Reynolds number increases from 6.02 x 10^6 m^{-1} to 8.12 x 10^6 m^{-1} in quiet flow. Three-fin model shown with R_{LE}=1/8", 75° fin sweep, and a sharp nosetip. 62

4.5 Slices of TSP images at x = 0.375 meters for Runs 703, 705, 706, and 707. The streaks spread on the cone surface and the heat transfer increases as Reynolds number increases. 63

4.6 Identical runs show different heat transfer on the fin and close to the corner. Three-fin model shown under quiet flow with R_{LE}=1/8", 75° fin sweep, and a sharp nosetip. 65

4.7 Power spectral density of the pressure fluctuations show that the heating in the corner is not due to transition. 66

4.8 Streak spreading reduces space between the streaks. TSP resolution limits the ability to define the edges of the streaks. Three-fin model shown with R_{LE}=1/8", 75° fin sweep, and a sharp nosetip. 67

4.9 PSD of sensor 15° from fin (PCB1) at increasing unit Reynolds number. This sensor location is closest to the fin. 69

4.10 PSD of sensor 30° from fin (PCB2) at increasing unit Reynolds number. This sensor location is between the streaks and the fin. 70

Figure Page

4.11 PSD of sensor 45° from fin (PCB3) at increasing unit Reynolds number. This sensor location is on the far side of the streaks from the corner. . . . 71

4.12 PSD of a PCB sensor on the three-fin model with no fins installed and a sharp nosetip. Second-mode instability measured at Re = 9.48 x 10^6 m^{-1}. 73

4.13 The second-mode frequency estimated using STABL increases linearly with the square root of unit Reynolds number. 73

4.14 Three heating streaks and extensive streak spreading are seen at higher Reynolds number. (Run 109, unit Re = 12.4 x 10^6 m^{-1}). Three-fin model shown with R_{LE}=1/8", 75° sweep, and a sharp nosetip. 74

4.15 At maximum quiet Reynolds number there are three streaks on the cone surface. Slice of TSP image for Run 109 at x = 0.356 meters. Data from Run 706 overlaid to show that the two streaks on the cone surface indicated by the arrows have the same location. 75

4.16 Increasing nosetip radius reduces streak spreading at a similar Reynolds number. Three-fin model shown with R_{LE}=1/8" and 75° sweep. 77

4.16 (cont'd) Increasing nosetip radius reduces streak spreading at a similar Reynolds number. Three-fin model shown with R_{LE}=1/8" and 75° sweep. 78

4.17 Increasing nose radius narrows the streak on the cone surface and reduces heat transfer. Slices of TSP images at x = 0.375 meters for Runs 703, 709, and 715 at similar Reynolds number. Three-fin model with R_{LE}=1/8" and 75° sweep. 78

4.18 Increasing nosetip radius reduces streak spreading at a similar Reynolds number. Three-fin model shown with R_{LE}=1/8" and 70° sweep. 79

4.18 (cont'd) Increasing nosetip radius reduces streak spreading at a similar Reynolds number. Three-fin model shown with R_{LE}=1/8" and 70° sweep. 80

4.19 Increasing nose radius narrows the streak on the cone surface, however, there is little effect on heat transfer. Slices of TSP images at x = 0.375 meters for Runs 719, 724, and 729 at a similar unit Reynolds number. Three-fin model with R_{LE}=1/8" and 70° sweep. 81

4.20 Increasing nosetip radius significantly decreases the broadband amplitude of the pressure fluctuations, indicating delayed transition. Measurements on three-fin model with R_{LE}=1/8" and 75° sweep. 83

4.20 (cont'd) Increasing nosetip radius significantly decreases the broadband amplitude of the pressure fluctuations, indicating delayed transition. Measurements on three-fin model with R_{LE}=1/8" and 75° sweep. 84

Figure Page

4.21 Increasing nosetip radius significantly decreases the broadband amplitude of the pressure fluctuations, indicating delayed transition. Measurements on three-fin model with R_{LE}=1/8" and 70° sweep. 85

4.21 (cont'd) Increasing nosetip radius significantly decreases the broadband amplitude of the pressure fluctuations, indicating delayed transition. Measurements on three-fin model with R_{LE}=1/8" and 70° sweep. 86

4.22 Second-mode instability suppressed both inside and outside of the streak with increased nose radius. Low-frequency instability seemingly unchanged by nose radius. Three-fin model with R_{LE}=1/8" and 75° fin sweep. 88

4.23 Conditions for an attached shock at the root of a blunt, swept fin reproduced from Stollery [23]. 91

4.24 Increasing fin sweep decreases streak spreading at a similar Reynolds number. Three-fin model shown with R_{LE}=1/8" and a sharp nosetip. 92

4.25 Increasing fin sweep narrows the streaks and moves the fin streak closer to the corner. Slices of TSP images at x = 0.368 meters. Three-fin model with R_{LE}=1/8" and a sharp nosetip. 93

4.26 Increasing fin sweep decreases streak spreading at a similar Reynolds number. Three-fin model shown with R_{LE}=1/8" and R_{NT}=1 mm. 94

4.27 Increasing fin sweep narrows the streaks and moves the fin streak closer to the corner. Slices of TSP images at x = 0.356 meters. Three-fin model with R_{LE}=1/8" and R_{NT}=1 mm. 95

4.28 Increasing fin sweep decreases the amplitude of the pressure fluctuation power spectra, indicating delayed transition. Three-fin model shown with R_{LE}=1/8" and a sharp nosetip. 96

4.28 (cont'd) Increasing fin sweep decreases the amplitude of the pressure fluctuation power spectra, indicating delayed transition. Three-fin model shown with R_{LE}=1/8" and a sharp nosetip. 97

4.29 Increasing fin sweep decreases the amplitude of the pressure fluctuation power spectra, indicating delayed transition. Three-fin model shown with R_{LE}=1/8" and R_{NT}=1 mm. 98

4.29 (cont'd) Increasing fin sweep decreases the amplitude of the pressure fluctuation power spectra, indicating delayed transition. Three-fin model shown with R_{LE}=1/8" and R_{NT}=1 mm. 99

4.30 Increasing fin bluntness moves the streak on the cone surface away from the corner. Three-fin model shown with a sharp nosetip and 70° sweep. . 101

Figure Page

4.30 (cont'd) Increasing fin bluntness moves the streak on the cone surface away from the corner. Three-fin model shown with a sharp nosetip and 70° sweep.102

4.31 Increasing fin bluntness moves the streak on the cone surface away from the corner. Slice of TSP images at x = 0.373 meters for Runs 518, 608, and 231 at Re = 8.36 x 10^6 m^{-1}. 102

4.32 Power spectra corresponding with vortex system very near the corner. Measurements on three-fin model with R_{LE}=1/16", 70° sweep, and a sharp nosetip. 104

4.33 Power spectra corresponding with vortex system coincident with the sensor at 30° from the fin. Measurements on three-fin model with R_{LE}=3/32", 70° sweep, and a sharp nosetip. 105

4.34 Power spectra for sensors far from the corner region for Run 605 (unit Re = 8.5 x 10^6 m^{-1}). Three-fin model shown with sharp nosetip, 75° sweep, and R_{LE}=3/32". 106

4.35 Power spectra for sensors around the azimuth of a 7° straight cone for a unit Reynolds number of 9.27 x 10^6 m^{-1}. Shows same peaks as sensors away from fin interaction region. Measurements were made while aligning the model during Entry 6. 107

4.36 Temperature change for the fin-cone at 4° angle of attack with the fin on the windward ray (Run 314, Re = 12.1 x 10^6 m^{-1}). Three-fin model shown under quiet flow with a sharp nosetip, 75° fin sweep, and R_{LE} = 1/8". . 108

4.37 Temperature change for the fin-cone at 0° angle of attack (Run 109, Re = 12.4 x 10^6 m^{-1}). Three-fin model shown under quiet flow with a sharp nosetip, 75° fin sweep, and R_{LE} = 1/8". 109

4.38 Temperature change for the fin-cone at 4° angle of attack with the fin on the yaw side (Run 316, Re = 10.1 x 10^6 m^{-1}). Camera is viewing the side of the cone where the fin is attached. Three-fin model shown under quiet flow with a sharp nosetip, 75° fin sweep, and R_{LE} = 1/8". 110

4.39 Temperature change for the fin-cone at 4° angle of attack with the fin on the yaw side (Run 321, Re = 9.97 x 10^6 m^{-1}). Camera is viewing the lee ray of the cone. Three-fin model shown under quiet flow with a sharp nosetip, 75° fin sweep, and R_{LE} = 1/8". 110

4.40 Mach contour computed for fin-cone geometry with 75° fin sweep, R_{NT}= 2 mm, and R_{LE}=1/8" at Re = 7.4 x 10^6 m^{-1}. 112

4.41 Vortices present in the corner on the cone and fin surfaces. 112

Figure Page

4.42 Heating pattern computed for fin-cone geometry with 75° fin sweep, R_{NT}= 2 mm, and R_{LE}=3/32" at Re = 7.4 x 10^6 m^{-1}. 113

4.43 Heating pattern matches qualitatively with CFD (Run 508, Re = 7.38 x 10^6 m^{-1}). Three-fin model shown with with 75° fin sweep, R_{NT}= 2 mm, and R_{LE}=1/8" 113

C.1 Entry 1 PCB and SB locations. View from back end of cone. 143

C.2 Entry 2 PCB and SB locations. View from back end of cone. 146

C.3 Entry 3 PCB and SB locations. View from back end of cone. 149

C.4 Entry 5 PCB and SB locations. View from back end of cone. 152

C.5 Entry 6 PCB and SB locations. View from back end of cone. 155

C.6 Entry 7 PCB and SB locations. View from back end of cone. 158

SYMBOLS

f	generic function
I_{dark}	intensity for "dark" images
I_{off}	intensity for "off" images
I_{on}	intensity for "on" images
M	Mach number
p	static pressure, $psia$
p'	pressure fluctuations, $psia$
p_0	stagnation pressure, $psia$
$p_{0,i}$	initial stagnation pressure, $psia$
p_{TM}	Taylor-Maccoll pressure, $psia$
$\dot{q}$	heat transfer, kW/m^2
R	specific gas constant, $Jkg^{-1}K^{-1}$
R_{LE}	fin leading edge radius, in
R_{NT}	nose tip radius, mm
Re	unit freestream Reynolds number, m^{-1}
T	static temperature, K
T_0	stagnation temperature, K
$T_{0,i}$	initial stagnation temperature, K
T_{model}	model temperature, K
T_{ref}	reference temperature, K
T_w	model wall temperature, K
x	downstream location along the central axis of the cone, in
α_i	angle for incipient separation, deg
β	shock angle, deg
δ	boundary layer thickness

ΔT	change in temperature, K
γ	specific heat ratio
κ	thermal conductivity
Λ	sweep angle, deg
μ	dynamic viscosity or Mach angle
θ	turn angle, deg

ABBREVIATIONS

AAE	Aeronautical and Astronautical Engineering
AOA	angle of attack
ASL	Aerospace Sciences Lab
BAM6QT	Boeing/AFOSR Mach 6 Quiet Tunnel
CFD	computational fluid dynamics
DPLR	Data Parallel Line Relaxation
FLDI	Focused Laser Differential Interferometry
LED	light emitting diode
LPSE	linear parabolized stability equations
LST	linear stability theory
PCB	PCB132A31 fast pressure transducers
PSD	power spectral density
SB	8-1-0.25-48-20835TBS Schmidt-Boelter heat transfer gauge
SBG	Spatial BiGlobal methods
SBLI	shock/boundary-layer interaction
STABL	Stability and Transition Analysis for hypersonic Boundary Layers
TSP	temperature sensitive paint

ABSTRACT

Turbeville, Franklin Drew MSAA, Purdue University, May 2018. Parametric Study of a 7° Half-Angle Cone with Highly-Swept Fins at Mach 6. Major Professor: Steven P. Schneider.

Boundary-layer instability and transition was measured on a 7° cone with highly-swept fins at 0° angle of attack in a Mach-6 quiet tunnel. Effects of fin sweep angle, fin bluntness, and nosetip radius were assessed. Using temperature-sensitive paint and piezoelectric fast pressure transducers, transition was measured in all configurations. Some features present under quiet flow were not seen under noisy flow. Multiple streaks of heat transfer with peaks near 5 kW/m^2 were noted on the cone surface. More streaks appeared and the streaks spread as the Reynolds number increased. Power spectral density plots were calculated from the pressure transducer data displaying two possible instabilities, one at low frequency and another at high frequency. Several heat-transfer streaks are also seen on the fin surface. The number of streaks appears invariant with Reynolds number. Increasing sweep, decreasing fin bluntness, and increasing nose radius delayed transition.

1. INTRODUCTION

1.1 Corner Flow and Shock/Boundary-Layer Interaction

Hypersonic vehicles often have complex three-dimensional configurations resulting in viscous-inviscid interactions. Many three-dimensional configurations include corner flows, which exist at wing-body, fin-body, and engine cowl junctions among other cases, and often have areas of high compression which can lead to separation of boundary layers. Reattachment associated with separated regions and shock/boundary-layer interactions (SBLI) cause areas of intense heating that can cause failure of structural components.

The X-15 experimental aircraft provides an example of where shock impingement on a boundary layer resulted in catastrophic failure. A ramjet suspended below the aircraft created shock waves that impinged upon the pylon supporting the ramjet [1]. The resulting high heating on the pylon caused the structure to fail, as shown in Figure 1.1. Knowledge of the location of SBLI and the corresponding high heat flux is therefore of the utmost importance when designing a hypersonic flight vehicle.

Three-dimensional flow fields containing SBLI are notoriously hard to predict, and designers must often depend on experiments to determine regions of high heating. Experiments with hypersonic corner flow have primarily involved turbulent boundary layers. Very few have considered interactions with laminar boundary layers and even fewer with transitional boundary layers. Dolling stated in his 2001 SBLI review, "Predicting transition to turbulence in supersonic and hypersonic boundary layers and understanding fully how the process is influenced by basic flow and geometric parameters ... is a goal yet to be reached" [2]. The effect of the transitional boundary layer on the corner interaction and the effect of the corner interaction on laminar-

Figure 1.1. Damage due to shock impingement on the X-15 pylon [1].

turbulent boundary-layer transition is not well known. Simulation does not seem likely to predict these flows with any confidence in the near future.

1.2 Laminar-Turbulent Transition

Boundary-layer transition is critical to the design of hypersonic vehicles due to its effect on heat transfer, boundary-layer separation, and other phenomena. It is also important with regards to SBLI. The severity of the viscous-inviscid interaction depends on the incoming state of the boundary-layer. SBLI induces large pressure gradients, which can separate the flow. Laminar boundary layers are more likely to separate than turbulent boundary layers. Subsequent reattachment results in increased heating. The flow field is complicated and prediction of transition is difficult. Though computational methods have improved, experiments remain the most reliable way to generate data on three-dimensional geometries. Experimental data can then be used to aid development of improved computational prediction methods.

1.3 Quiet Tunnels

Transition prediction from first principles has remained elusive, which drives the need for empirical correlations, flight tests, and wind tunnel experiments. Ground-based testing is much more cost and time-effective than expensive flight test programs. Wind tunnels attempt to replicate flight conditions, though no wind tunnel can fully replicate hypersonic flight, and allow for testing more conditions and orientations than might be accomplished in relatively few flight tests. Conventional hypersonic wind tunnels present a problem as they have freestream pressure fluctuations several orders of magnitude higher than what is seen in flight. Typically, conventional tunnels have pitot pressure fluctuation levels on the order of 1% or greater [3]. Fisher and Dougherty found that the flight disturbance level varied between 0.005% and 0.03% [4]. The tunnel noise in these conventional tunnels can lead to earlier transition than would be seen in flight, which affects many aspects of design.

Laufer determined that the pressure fluctuations were primarily due to acoustic noise radiated from the turbulent boundary layer on the nozzle wall [5]. Figure 1.2 shows a shadowgraph obtained by Reda in the Naval Ordnance Lab ballistic range [3, 6]. Along the bottom of the cone is a completely turbulent boundary layer. Radiated noise can be seen as acoustic waves. Along the top of a cone is a laminar boundary layer with two turbulent spots. In the laminar portion of the boundary layer there are no obvious radiated waves. However, noise is radiated from the turbulent spots. This figure demonstrates that acoustic noise causes freestream fluctuations, as Laufer found.

The development of quiet tunnels is vital to the investigation of laminar-turbulent transition. Quiet tunnels achieve freestream pressure fluctuations less than 0.05% by maintaining a laminar boundary layer on the nozzle wall [3]. The decreased pressure fluctuations increase the transition Reynolds number closer to what would be seen in flight.

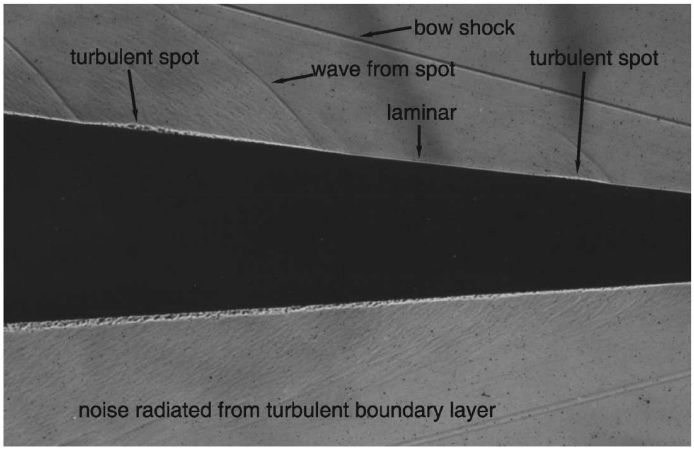

Figure 1.2. Noise radiated from the turbulent boundary layer on a cone at Mach 4.31 [3,6]. Laminar regions do not show the same radiated noise.

1.4 Fin-Cone Geometry

Tests of a slender cone with highly-swept fins in a quiet tunnel have been carried out to study transition and hypersonic corner flow. Figure 1.3 shows an isometric view of the geometry, whose main features include highly-swept fins with blunt leading edges. Many hypersonic vehicles have corners similar to the fin-cone junction, which combines two common corner flow problems: (1) the interaction of the glancing fin-shock and the boundary layer on the body, and (2) axial corner flow between the fin and body. Both problems have been studied extensively, however, the available data on transitional boundary layers is small. In addition, the literature for interactions with leading edge sweep largely considers moderate sweep angles of less than 60° at supersonic Mach numbers.

Little data exists for highly-swept fins at hypersonic Mach numbers. Some of the only data of this type that exists publicly were gathered by Chynoweth et al. and Abney and Rochlitz at Purdue University in Mach 6 quiet flow [7,8]. The fins in these experiments had complicated geometries with limited applicability to flight. The blunted fins tested in the present experiments are relevant to many hypersonic flight vehicles. Computational simulations and stability analyses are also needed.

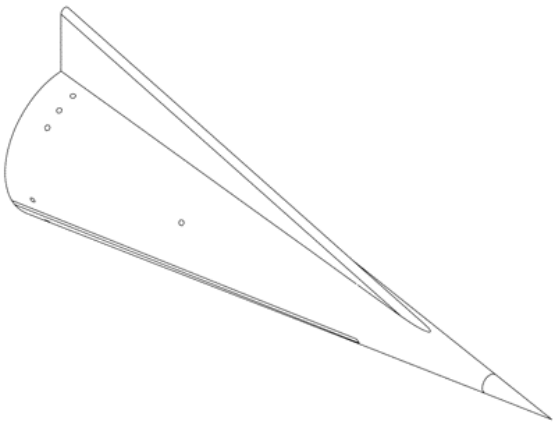

Figure 1.3. Tested fin-cone geometry with blunt, highly-swept fins.

1.5 Overview of Experiments

Instability and transition in flow past highly-swept fins is not well understood. The current research consists of a series of experiments to evaluate the fin-cone flow field, the heating levels in the corner, the instabilities of the boundary layer in the corner, and how these are affected by geometric parameters. The objectives of the experimental program were as follows:

1. Determine whether transition occurs naturally under quiet tunnel conditions for the fin-cone geometry.

2. Measure global heat transfer in the fin-cone interaction region with temperature sensitive paint.

3. Search for possible boundary-layer instabilities by measuring pressure fluctuations using fast pressure sensors in the fin-cone interaction region.

4. Evaluate the effect of geometric parameters such as nose bluntness, fin bluntness, and fin sweep on transition, heat transfer rates, and boundary layer instabilities.

2. REVIEW OF LITERATURE

The fin-cone geometry combines aspects of two well established corner flow problems: axial corner flow and glancing shock/boundary-layer interaction. Axial corner flow in its most general form consists of two intersecting wedges with coincident leading edges. A complex flow field results from the intersection of the wedge bow shocks. The glancing SBLI problem is a special case of axial corner flow where the lip of one wedge is extended far upstream. The bow shocks no longer interact, and the interaction consists solely of a swept shock and the boundary layer on the opposite surface.

2.1 Axial Corner Flow

Many detailed reviews of high-speed axial corner flow have been written, notably those by Korkegi [9], Hummel [10], and Panaras [11]. Experimental configurations primarily take the form of intersecting wedges or the intersection of a wedge and a flat plate with coincident leading edges. The wedge-wedge case consists of an interaction between two strong shocks, whereas the wedge-plate case consists of a strong shock interacting with a relatively weak bow shock off the lip of the flat plate.

Charwat and Redekopp conducted the first detailed investigation of the flow field in the corner between two wedges [12]. They tested a symmetrical corner model composed of two sharp wedges with 12.2° incidence to the freestream. Measurements of surface and flow-field pressures as well as oil flow visualizations were performed at Mach numbers between 2.5 and 4. The corresponding Reynolds number range was between 1.0 x 10^5 in^{-1} at Mach 4 and 2.5 x 10^5 in^{-1} at Mach 2.5. The boundary layers on the wedges were laminar and their thickness was small compared to the shock distance from the surface. The investigators were able to determine the shock

structure as shown in Figure 2.1. A third shock, or corner shock, is formed at the intersection of the wedge bow shocks. From the intersection of the corner shock and bow shocks emanate two inner shocks, or embedded shocks. The point at which the bow shock, corner shock, and embedded shock intersect is called the triple point. Slip lines also initiate at the triple point, separating the flow behind the embedded shock from the flow behind the corner shock. Increasing the Mach number was shown to move the entire shock structure closer to the corner.

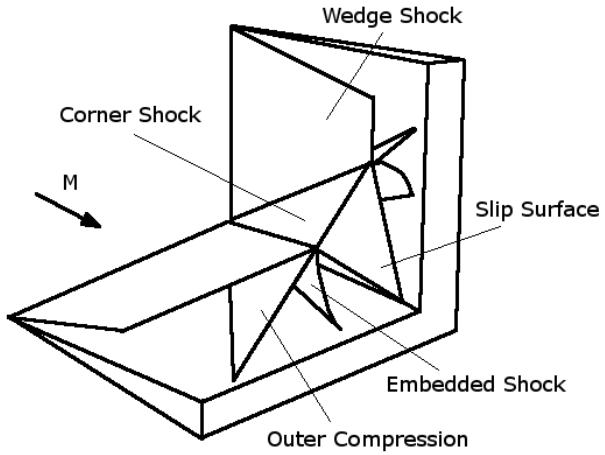

Figure 2.1. Shock structure in an axisymmetric corner formed by two wedges. Figure redrawn from Charwat and Redekopp [12].

Further experiments by Watson and Weinstein [13] showed that a similar structure is present in hypersonic flow. They tested symmetrical corner configurations composed of two sharp wedges with 0°, 5°, and 10° incidence to the freestream. They performed measurements of surface and flow field pressure, heat transfer, oil flow visualization, and electron beam imaging at Mach 20 in the NASA Langley 22-inch helium tunnel. The Reynolds number could be adjusted between 5.12 x 10^6 m^{-1} and 26.38 x 10^6 m^{-1} by changing the stagnation pressure and stagnation temperature. The boundary layers were laminar on the wedge surfaces. They found that the features at Mach 20 are much the same as at Mach 3 but are distorted by large vortices and thick boundary layers. Figure 2.2 shows Watson and Weintein's interpretation

of the Mach 3 results of Charwat and Redekopp. Peaks in heating are observed near where the embedded shock impinges on the boundary layer. They suggest that the low pitot pressure measured in this region indicates a vortex which causes the peaks in heating.

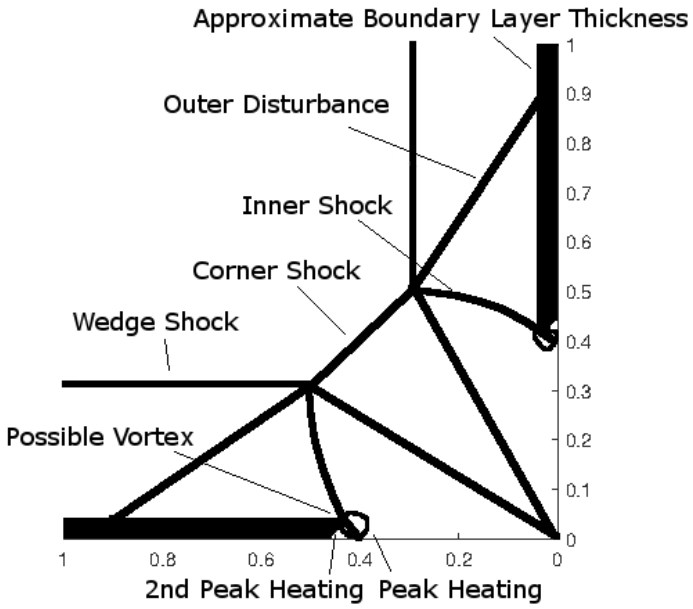

Figure 2.2. Corner flow structure at Mach 3.17 (Re = 1.75 x x 10^5 in^{-1}), redrawn from Watson and Weinstein [13]. Possible vortex where inner shock impinges on the boundary layer.

Figure 2.3 shows the Mach 20 flow field measured by Watson and Weinstein. They were able to verify the existence of a vortex in the corner and a corresponding peak in heating. A second peak in heating is found corresponding with a disturbance originating from the embedded shock. They suggest that this disturbance resembles one leg of a lambda shock. This lambda shock is formed by the embedded shock, the compression of the flow at the vortex separation, and the compression of the flow at the vortex reattachment. The lambda shock gets its name from its resemblance to the Greek letter λ.

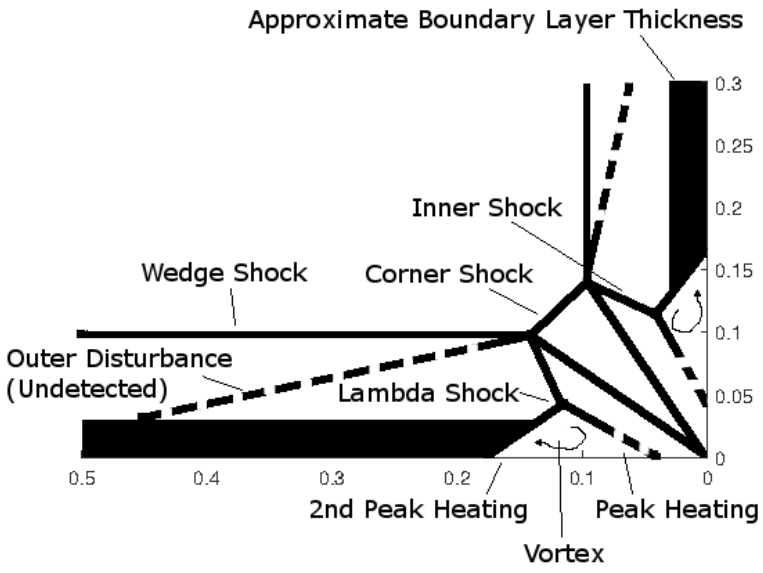

Figure 2.3. Corner flow structure at Mach 20.3 (Re = 14.17 x 10^6 m^{-1}). Structure is similar to Mach 3, however, it is distorted by large vortices and thick boundary layers. Redrawn from Watson and Weinstein [13].

Charwat and Redekopp performed preliminary experiments with asymmetry [12]. They tested a model with one wedge at 12.2° incidence to the freestream, called the base wedge, and another wedge at incidences of 3.5°, 7.5°, and 12.2° to the freestream, called the interference wedge. Their measurements showed that as the interference wedge angle decreases the static pressure on the base wedge decreases. The effect of interference wedge angle on the shock structure is shown in Figure 2.4. As the interference wedge angle decreases, the embedded shock location approaches the two-dimensional oblique shock for the base wedge. On the base wedge, the triple point and the location where the shock intersects the surface remains unchanged.

Cooper and Hankey investigated highly asymmetric corner flow [14]. They tested a wedge with 15° incidence to the freestream mounted on a flat plate with coincident leading edges. The model was tested in the ARL 20-inch Hypersonic Wind Tunnel at Mach 12.5 and a freestream unit Reynolds number of 0.95 x 10^6 ft^{-1}. The boundary layers on the wedge and plate surfaces were fully laminar. Surface pressure measure-

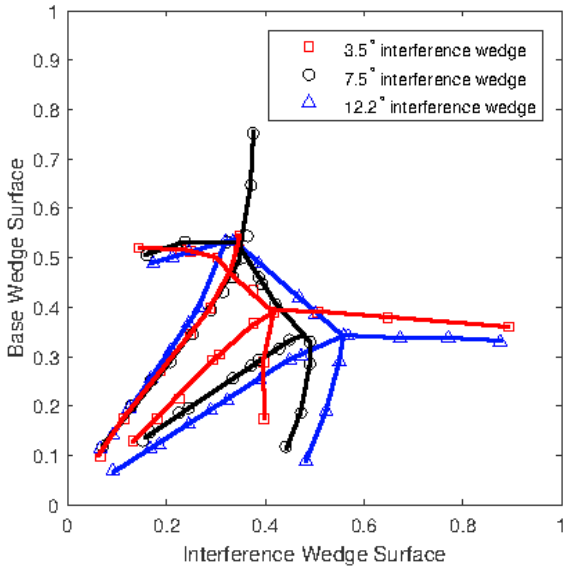

Figure 2.4. Asymmetry produces a shock structure distorted from the axisymmetric case but maintaining many of the basic features. The inner shock on the interference wedge approaches the two-dimensional shock of the base wedge. Redrawn from Charwat and Redekopp [12].

ments were made on the flat plate in addition to a flow field pitot survey and oil flow visualization, from which they were able to construct the inviscid flow structure. Figure 2.5 shows the shock structure determined by Cooper and Hankey as well as separation and reattachment points found from the oil flow. Rather than seeing two triple points as found by Charwat and Redekopp, Cooper and Hankey found only one. The wedge shock interacted with the flat plate bow shock resulting in an embedded shock impinging on the flat plate surface. Oil flow visualization led to the determination that there were two separated regions indicating two separate vortices on the flat plate surface. These vortices correspond with areas of high heating and pressure. The inboard vortex has significantly higher heating and pressure than the outboard vortex. Reexamination of the oil flow data by Korkegi concluded that there was a secondary separation underneath the primary vortex, rather than two separate

vortices [15]. Figure 2.6 details this corrected flow field. The shock structure is not shown, as it is unchanged from Cooper and Hankey's interpretation.

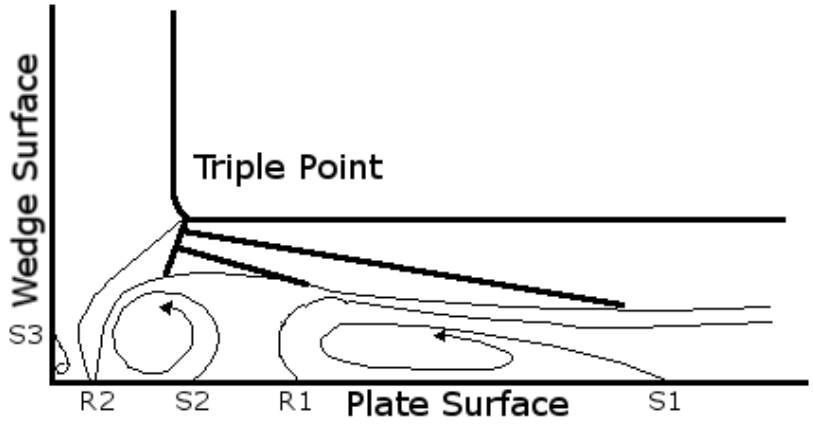

Figure 2.5. Single triple point and two vortices seen by Cooper and Hankey for a wedge-plate axial corner. Redrawn from Cooper and Hankey [14].

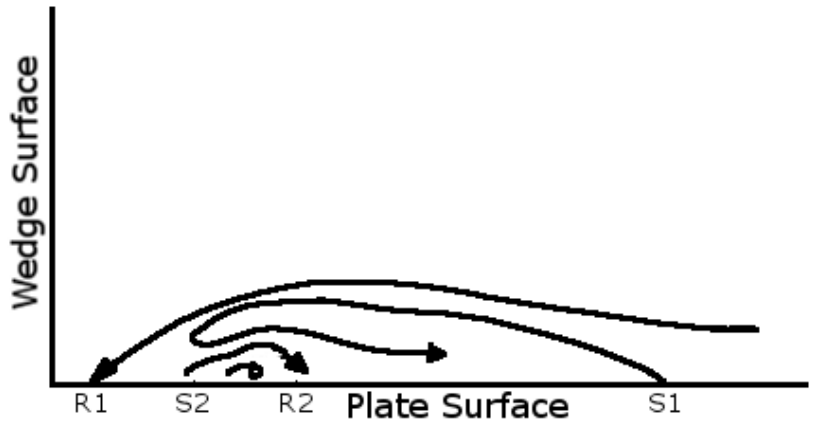

Figure 2.6. Reexamination of the oil flow data replaces the initial finding of two vortices with this interpretation of a secondary vortex. Redrawn from Korkegi [15].

Papuccuoglu performed heat transfer and oil flow visualization on an axisymmetric wedge-wedge model and an asymmetric wedge-plate model. The wedges for both the wedge-wedge model and wedge-plate model have 9° incidence to the freestream. The tests were performed at Mach 6 over a unit Reynolds number range of 7.0 to 22.5 x 10^6 m^{-1} [16]. Oil flow visualization indicated that the model surface boundary layers were initially laminar and would transition to turbulent at some unspecified point downstream. At the lowest Reynolds number, the transition point was very near the aft end of the model. The transition location moved upstream with increasing unit Reynolds number. He measured the heat transfer at 7.5 centimeters from the leading edge using infrared thermography techniques verified using a sublimation method. He was able to identify as many as four peaks in heating for the wedge-plate model and three peaks for the wedge-wedge model, both at a unit Reynolds number of 15 x 10^6 m^{-1}. He also measures a decrease in aerodynamic heating near the corner centerline. The heat transfer measured for the wedge-wedge model was generally 1.5 times more than for the wedge-plate model. Using the oil flow images, he was able to visualize a system of separated regions corresponding to the peaks in heating as shown in Figure 2.7. The physical phenomena of the shock interacting with the surface is qualitatively similar for both models.

Up until 1967, the vast majority of axial corner flow experiments involved laminar boundary layers with the exception of some preliminary experiments by Stainback and Weinstein with turbulent boundary layers [17]. They performed heat transfer measurements at Mach 8 on a model consisting of a 5° incident wedge mounted on a flat plate. Their data in Figure 2.8 shows that the increase in heating in the corner above the theoretical heating on a flat plate will be less for turbulent boundary layers than for laminar boundary layers. This is explained by the fact that turbulent boundary layers are much less likely to separate than laminar boundary layers. The resulting heating at reattachment would increase heat transfer.

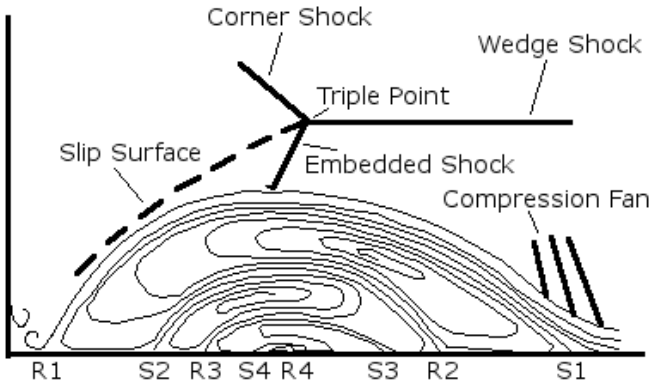

Figure 2.7. Flowfield constructed with four separations and reattachments corresponding with measured peaks in heating (Re = 15 x 10^6 m^{-1}). Figure redrawn from Papuccuoglu [16].

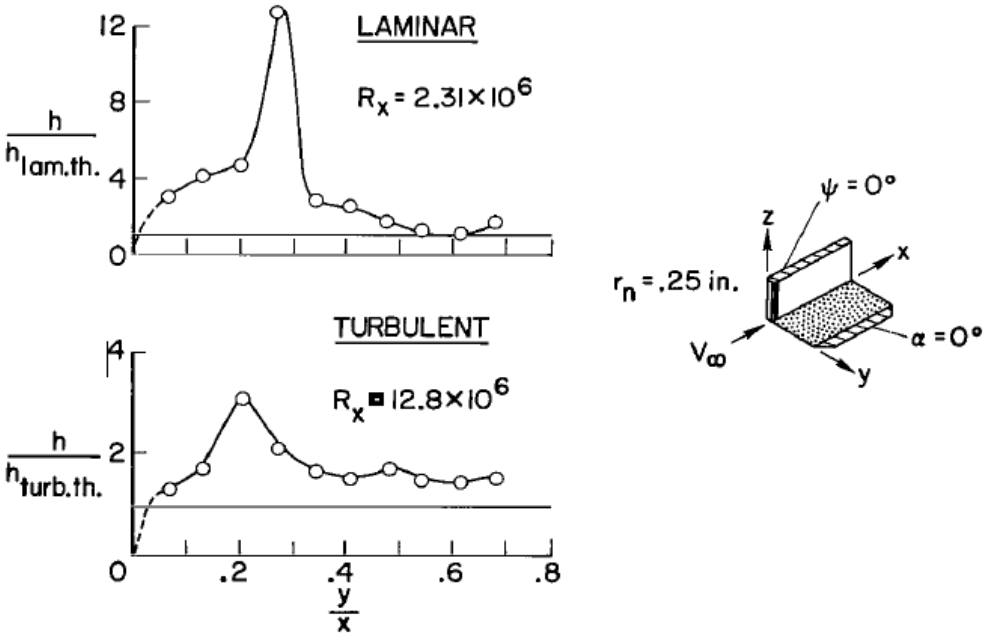

Figure 2.8. A laminar boundary layer will have a larger increase in heating over theoretical flat plate values than a turbulent boundary layer [17]. This is due to separation being more likely in the laminar interaction and the subsequent heating due to reattachment.

Much later, Papuccuoglu made similar measurements at Mach 6 for a wedge-wedge configuration and found that the number of separated regions decreased due to the turbulent boundary layer [16]. Heat transfer measurements with a turbulent boundary layer at a unit Reynolds number of 21 x 10^6 m^{-1} show only one separated region, whereas in the laminar case as many as three were seen. The magnitude of this turbulent heat transfer is between 2 and 3 times higher than for a laminar boundary layer at a lower unit Reynolds number of 15 x 10^6 m^{-1}. He reports no direct comparisons of turbulent and laminar flow data at similar Reynolds number.

West and Korkegi presented some of the first data showing the effect of transition on an axial corner flow [18]. Oil flow visualization was performed on a corner formed by intersecting 9.5° incidence wedges at Mach 3 over a unit Reynolds number range of 0.86 x 10^5 in^{-1} to 1.2 x 10^7 in^{-1}. Lines of accumulation in the oil on the surface correspond with separation lines. Figure 2.9 shows the oil accumulation lines for a single case with laminar, transitional, and turbulent regions. The dark line indicates boundary-layer separation upstream of the embedded shock location. The lateral extent of the separation for the laminar flow region is much greater than for the turbulent flow region. When the boundary layer transitions, the characteristics of the flow converge to those expected for a turbulent flow.

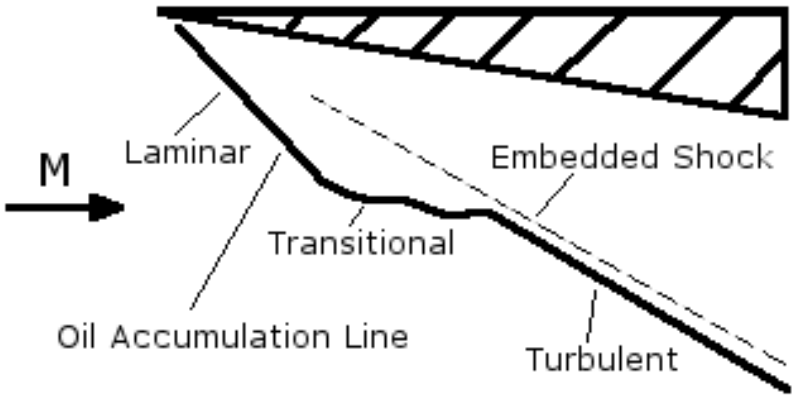

Figure 2.9. Lateral extent of the interaction is greater for laminar interactions. The oil accumulation line approaches the turbulent case as the boundary layer transitions. Figure redrawn from Korkegi [19].

2.2 Glancing Shock/Boundary-Layer Interaction

Glancing shock/boundary-layer interaction has been studied extensively due to its applicability to wing-body and fin-body geometries. Reviews by Green [20], Korkegi [9], Settles and Dolling [21], Panaras [11], Dolling [2], and Stollery [22,23] cover the problem in great detail. In the glancing shock wave case, there is one surface, called the shock generator surface, that projects a shock onto another surface with a laminar, turbulent, or transitional boundary layer that could be either fully developed or developing. Experimentally, this configuration often takes the form of a fin mounted on a flat plate or on the wall of a wind tunnel. The fin is usually either a wedge or a flat plate at angle of attack. Figure 2.10 shows a generic example of this interaction. Most of the experiments were performed at high Reynolds number so that the shock impinges on a turbulent boundary layer.

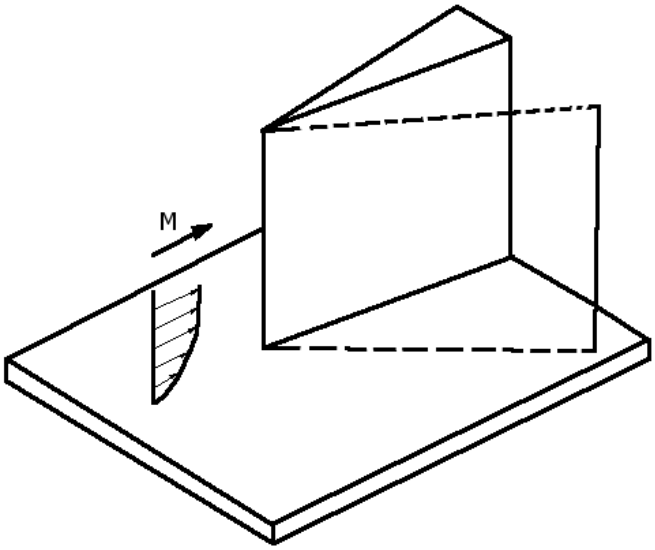

Figure 2.10. Example of glancing SBLI experimental model. A wedge is mounted on a flat plate with an existing fully-developed boundary layer. The inviscid shock wave interacts with the boundary layer.

Kubota and Stollery performed a series of experiments to describe the flow field of a glancing shock wave interacting with a turbulent boundary layer [24, 25]. They tested a variable angle-of-attack shock generator mounted on a tunnel wall with a turbulent boundary layer that was 1.6 centimeters thick. The test section Mach number was 2.3 and the unit Reynolds number was 3.1 x 10^4 cm^{-1}. Using oil flow visualization they were able to construct a flow pattern. For small wedge angles, the flow takes the form of the attached flow field in Figure 2.11. The high pressure zone on the shock generator surface escapes to the low pressure zone on the side wall. Crossflow induced by the pressure difference manifests as a corner vortex. When the wedge angle becomes great enough, the side-wall boundary layer separates and rolls up into a vortex as in Figure 2.12. The flow field now consists of two counter-rotating vortices: one tight vortex on the shock generator and one long, weak vortex on the side wall.

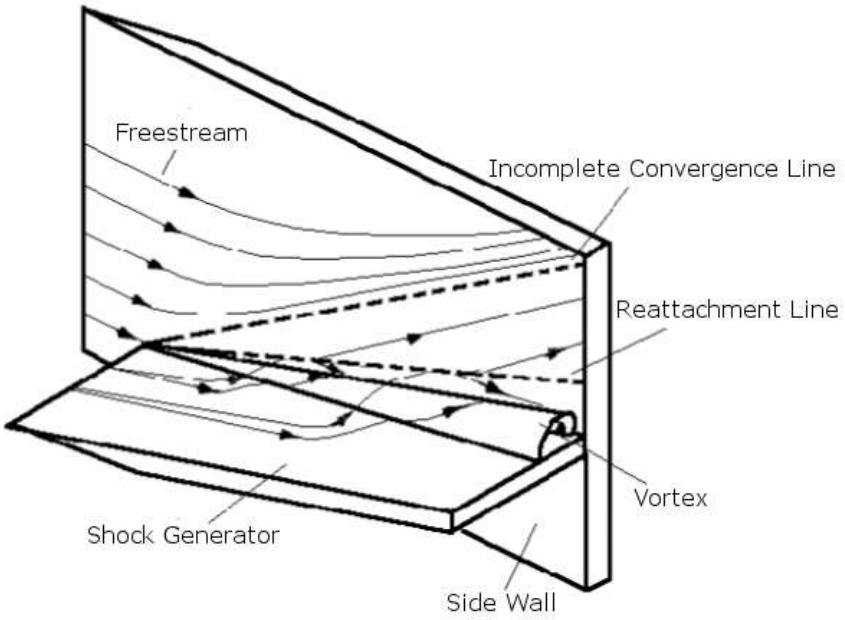

Figure 2.11. Attached flow field redrawn from Kubota and Stollery [25].

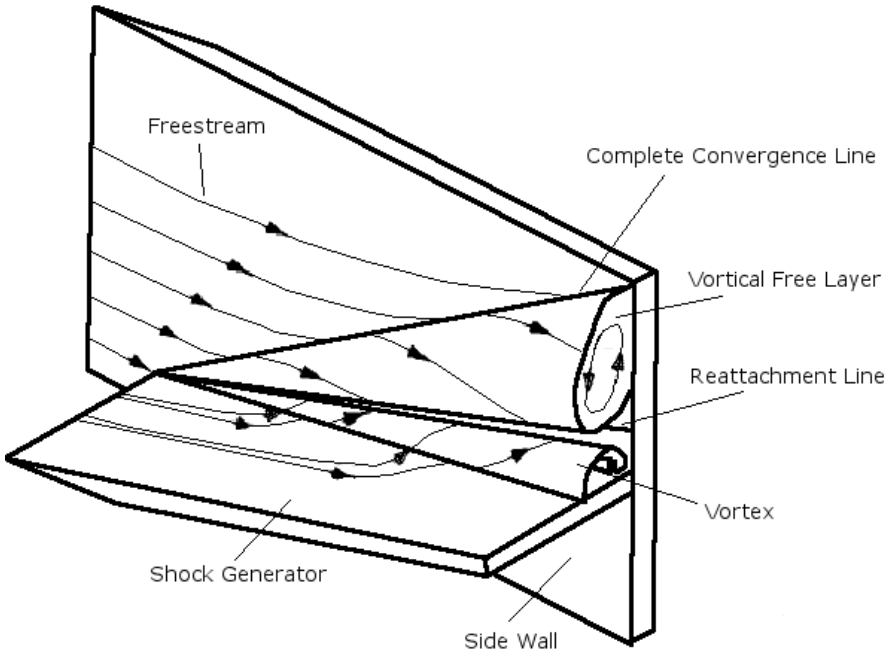

Figure 2.12. Separated flow field redrawn from Kubota and Stollery [25].

Experiments by Alvi and Settles resulted in a physical model of the interaction flow field [26]. Their test article consisted of a shock generator mounted on a flat plate. The incidence of the shock generator with respect to the fin stream was varied between 10° and 25°. The model was tested at Mach 3 and 4, and the boundary layer on the flat plate was turbulent with a 3 millimeter thickness near the leading edge of the shock generator. The unit Reynolds number varied from 58 x 10^6 m^{-1} to 72 x 10^6 m^{-1}. Planar light scattering was used to visualize the flow in a plane normal to the undisturbed inviscid shock. The image produced differentiates between areas of high and low density, which highlights the shock structure. Images were taken for several different interaction strengths, which are varied by changing the Mach number and shock generator angle of attack.

Figure 2.13 shows the shock structure obtained by Alvi and Settles for a strong interaction. A separated region is observed and a lambda shock structure is formed by the inviscid shock wave, the separation shock, and the rear shock. A slip line emanates from the triple point and curves around the separation bubble, terminating at the flat plate surface. An impinging jet structure is formed by the streamtube processed through the lambda shock. This jet is bounded on one side by the separated region and on the other side by the slip line. The flow turns through this jet region via isentropic Prandtl-Meyer expansions which reflect from the slip line as compression fans. As the strength of the interaction increases, the flow in the jet turns through a larger angle. When the compression becomes strong enough, a normal shock is formed. It is suggested that this jet is the cause of peak heating associated with the separation region. Alvi and Settles note that at high enough interaction strengths a secondary separation region appears and supersonic reverse flow is observed. Stollery, commenting on this work, notes that this interaction is similar to one half of the flow in an axial corner [23].

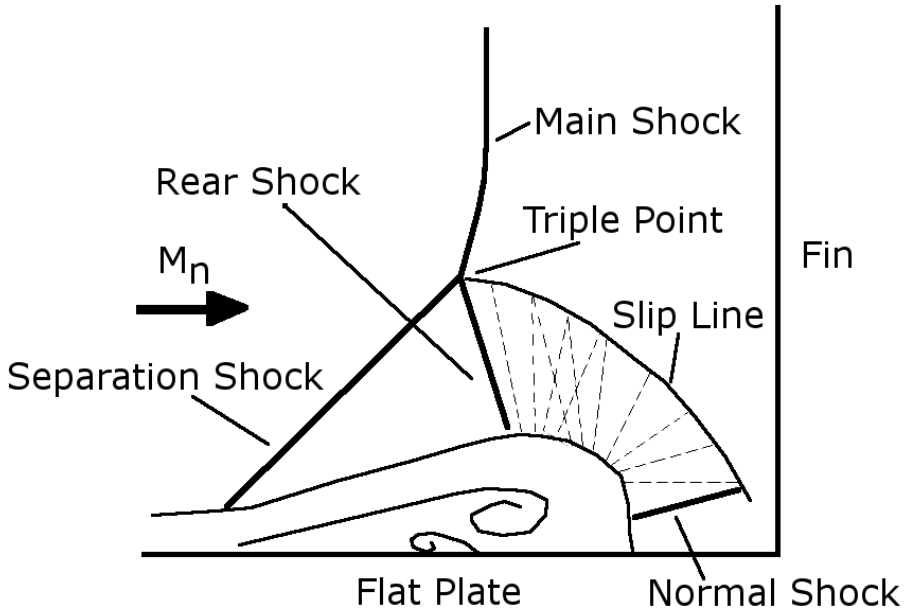

Figure 2.13. Lambda shock and stream tube observed by Alvi and Settles [26]. Figure redrawn from Stollery [23].

Very few experimental studies have been made with laminar boundary layers. Degrez and Ginoux produced the most notable laminar glancing shock experiment [27]. Their experiment consisted of a series of wedges with different angles mounted on a flat plate in Mach 2.25 flow over a unit Reynolds number range of 1.2 x 10^6 m^{-1} to 2.4 x 10^6 m^{-1}. The boundary layer thickness on the flat plate varied between 1.1 and 2.2 millimeters depending on the downstream location at which the wedges were mounted on the plate. They collected surface static pressures and performed surface flow visualization with an oil-graphite mixture. They found that extensive separation existed for all conditions tested. At their lowest wedge angle of 4° they were able to see separation, whereas the angle for incipient separation in turbulent flow is around 10° [23].

2.3 Fin Bluntness Effects

Blunting a fin causes the fin shock to stand off from the leading edge of the fin. This means that the shock is normal to the flow heading into the stagnation point. The pressure increase due to the strong normal shock can separate the boundary layer on the adjacent surface ahead of the fin, further complicating the shock structure.

Kaufman et al. performed a review of their own experiments and others to describe the flow ahead of blunt fins [28]. The data they examine spans a Mach number range from 1.2 to 21. They describe the lambda shock structure that forms at the fin leading edge due to the fin bow shock, as shown in Figure 2.14. The fin bow shock induces a large pressure rise causing the boundary layer to separate. A shock is then present at the upstream and downstream ends of the separation bubble. Within this separation bubble many horseshoe shaped vortices form and spiral downstream. The separation occurs approximately two fin leading edge diameters upstream of the fin for turbulent flow. This is insensitive to Mach number, Reynolds number, or boundary-layer thickness. Separation of laminar flow is much more extensive but is also dependent on fin leading edge diameter, Mach number, and Reynolds number making it hard to predict.

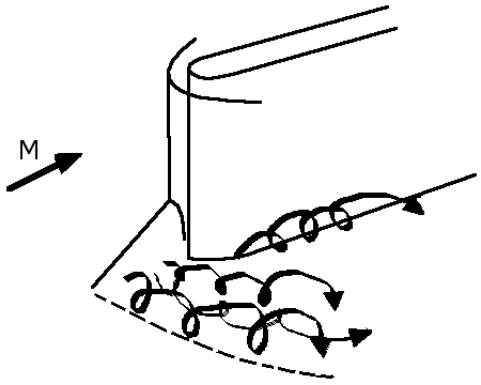

Figure 2.14. Horseshoe vortices formed by separation of boundary layer ahead of a blunt fin redrawn from Kaufman et al. [28].

Fomison performed experiments on the effects of fin bluntness at Mach 2.4 and a unit Reynolds number of 2.6 x 10^6 m^{-1} [29]. He tested six hemicylindrically-blunted, unswept fins mounted on the side wall of the wind tunnel with a turbulent boundary layer. Oil flow measurements indicated four vortices emanating from the fin root, wrapping around the fin, and heading downstream. Stollery notes that as many as 6 of these vortices have been seen in other experiments [23]. Fomison found that the main effects of reducing the ratio of cylinder diameter to boundary-layer thickness, D/δ, are to lower the peak surface pressures and increase the non-dimensional mean extent of the surface flow, x_{LE}/D, as shown in Figure 2.15.

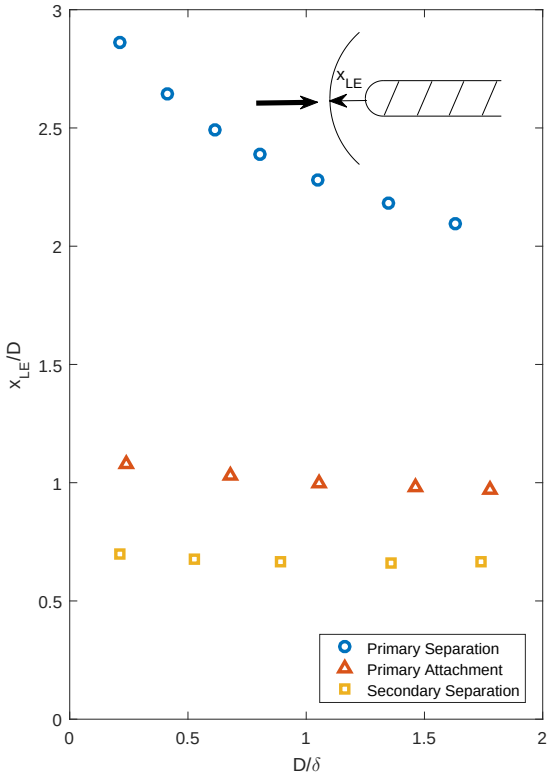

Figure 2.15. Non-dimensional extent of separation at the leading edge decreases as D/δ increases. Figure redrawn from Figure 64 in Fomison [29].

2.4 Fin Sweepback Effects

Möllenstädt examined the effect of sweep on an axial corner configuration at Mach 12.3 and a unit Reynolds number of 5 x 10^6 m^{-1} in the gun tunnel at TU Braunschweig [30, 31]. An English language summary of the data was written by Hummel [10]. Sweepback from 0° to 60° was tested for a 90° corner formed by sharp wedges with 8° incidence to the freestream. Flowfield pitot pressure, wall pressure, heat flux, and oil flow images were obtained. When the fins were unswept, primary and secondary vortices were apparent in the oil flow. As the fin sweep is increased, the strength of these vortices decreases until the secondary separation is no longer present at a sweep of 60°. The shock system is also weakened and moves towards the corner. With increasing sweep angle the maximum pitot pressure and maximum heat transfer is significantly reduced as shown in Figure 2.16.

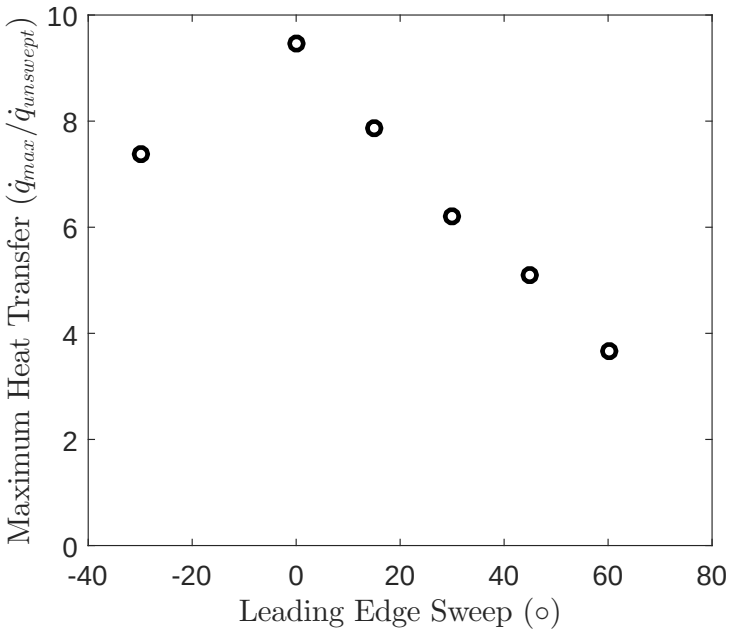

Figure 2.16. Increasing sweep significantly reduces the maximum heat transfer in an axial corner. Data presented taken from Figure 10 in Möllenstädt [30].

Bushnell tested cylinders swept as much as 60° interacting with a wedge shock at Mach 8 over a unit Reynolds number range of 0.77 x 10^5 in^{-1} to 8.7 x 10^5 in^{-1} [32]. The model consisted of cylinders mounted a flat plate inclined 12° to the freestream. The 1-inch-diameter cylinders were swept between 45° and 60° with the respect to the freestream. The undisturbed wedge boundary-layer thickness, for the lowest Reynolds number tested, was 0.15 inches at a location 12 inches from the leading edge of the plate. This is aft of where the cylinders were mounted. The cylinders were instrumented with thermocouples and pressure orifices connected to mercury manometers. Schlieren photography was used to visualize the flow field. The focus of this study was primarily on the interaction of the wedge shock and cylinder shock, and its effect on the boundary layer near leading edge. The downstream flow field was not examined. He found that the extent of the separation upstream of the cylinder is small for the tested conditions and that the interaction at the leading edge was a Type VI shock-shock interaction rather than the lambda shock shown by Stollery [23]. The shock structure ahead of the swept cylinder is shown in Figure 2.17. Similarly, Kaufman et al. note that fin sweep greatly reduces the peak pressure and heat transfer at the fin leading edge [28].

An investigation of the effect of leading edge sweep on a swept turbulent interaction at Mach 2.4 was carried out by Fomison [29] and Fomison and Stollery [33]. Sharp fins with sweep angles from 30° to 75° were tested. Surface pressure measurements indicated that the overall surface pressure level drops and the lateral extent of the interaction decreases slightly with increasing sweep. The application of sweep did not qualitatively change the process by which shock-induced boundary-layer separation occurs. The increase of sweep merely changes the rate of development of the flow field.

Aso et al. tested sweepback of as much as 45° at Mach 3.8 on blunt fins [34]. The unit Reynolds number varied between 2.95 x 10^7 m^{-1} and 3.21 x 10^6 m^{-1}. The fins were mounted on a flat plate with a turbulent boundary layer. The authors noticed a significant decrease in the extent of the interaction with increasing sweep angle.

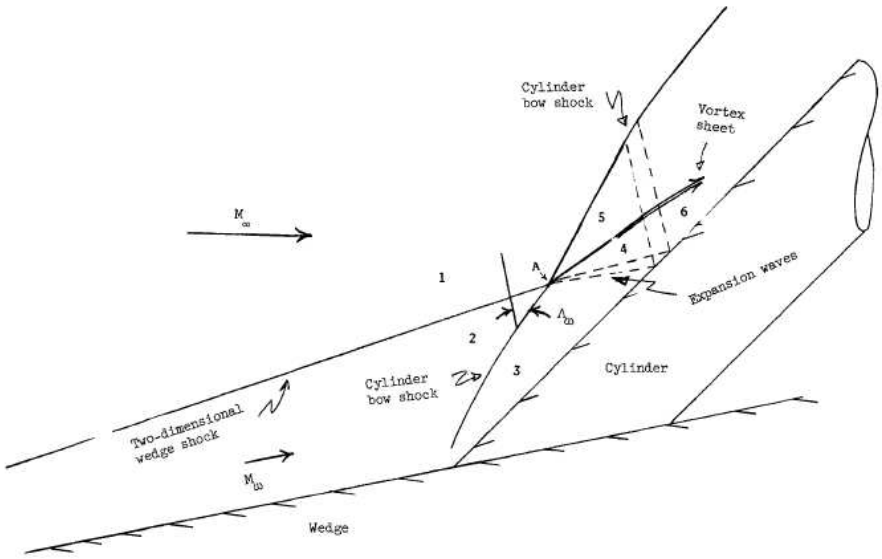

Figure 2.17. Sweep reduces the strength of the shock-shock interaction at the fin leading edge. Taken from Figure 4 in Bushnell [32].

Secondary separations were seen at lower sweep angles, but only primary separations were seen for sweeps of 30° and 45°. Correspondingly, the number of heating peaks reduced from two to one as sweep increased.

2.5 Fin-Cone Experiments

Bramlette et al. performed the earliest study, known to this author, of a cone with swept fins in high Mach number flow [35]. The fins were small and mounted near the aft end of the cone unlike the fins in the present experiments. The maximum fin sweep was 60°, which is not as highly swept as the present fins. Their results focus primarily on the incidence of the fin with respect to the freestream rather than other parameters such as fin sweep or fin leading-edge radius. They note that fin sweep, out of all of the fin geometrical parameters, had the most pronounced effect on their measurements. Little data, however, is presented to clarify this statement.

Later, Gillerlain performed more detailed measurements of the fin-cone flowfield at Mach 5 and at unit Reynolds numbers of 4.5 x 10^6 ft^{-1}, 13 x 10^6 ft^{-1}, and 26 x 10^6 ft^{-1} [36]. The cone model tested had a half angle of 5° and the boundary layer was likely turbulent. Two fins were constructed with 0.125-inch leading-edge radii: one was unswept and the other had 60° sweep. The fins were mounted at the aft end of the cone, on opposite sides of the cone, and were only 2 inches long compared to the 18.5 inch total length of the cone. The height of the fins was such that the cone bow shock never intersected the fins. He conducted heat transfer measurements using a phase-change temperature-sensitive paint. The model was instrumented with pressure taps on the fin leading edge and on the cone several fin leading-edge diameters upstream. Oil flow visualization was also used to provide data on the surface flow. He notes that qualitatively, the fin-cone flow field is not much different than that for a fin mounted on a flat plate. Also, the quantitative measurements of peak heat transfer and peak pressure are on the same order of magnitude for both the fin-cone and fin-plate configurations.

Figures 2.18 and 2.19 show isoheating contours for both fins. The values shown are the heat transfer coefficients obtained from the temperature-sensitive paint. The level of heat transfer is greatly reduced, by 25% for the fin leading edge and by 40% on the cone surface, for the swept interaction compared to the unswept interaction. The lateral extent of the heating is also reduced as fin sweep is increased. Examination of the oil flow indicated two separation lines for both fins. The lateral extent of the disturbance is significantly reduced for the swept fin configuration compared to the unswept, similar to the heating patterns.

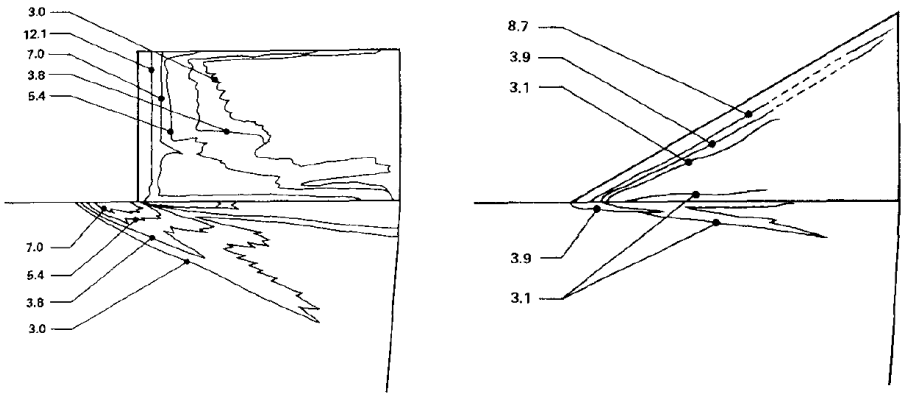

Figure 2.18. Side view of isoheating contours at Re = 4.5 x 10^6 ft^{-1} shows that the heating levels are much reduced for both the fin and cone surfaces. Values shown are heat transfer coefficients (h x 10^3 BTU/ft^2-sec-°R). Figure taken from Figures 4 and 6 in Gillerlain [36].

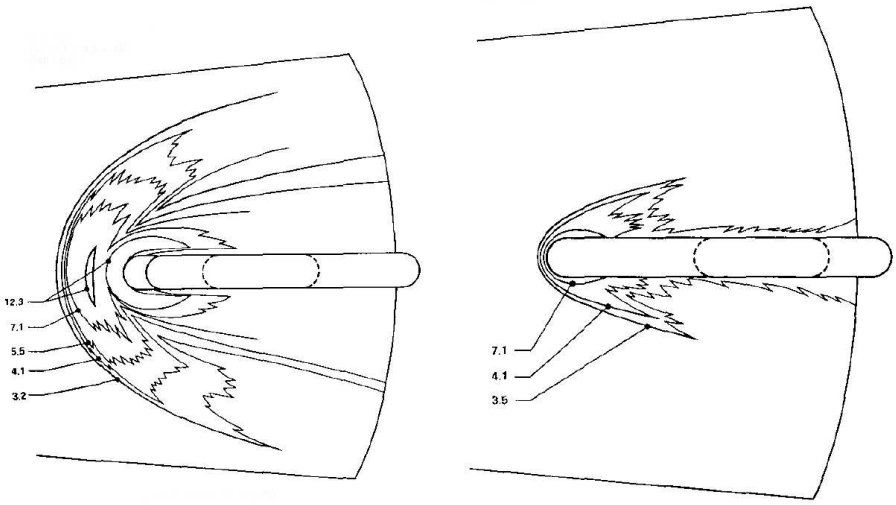

Figure 2.19. Top view of isoheating contours at Re = 4.5 x 10^6 ft^{-1} shows that the heating levels are much reduced for cone surface. The lateral extent of the heating is much less for the swept fin than the unswept fin. Values shown are heat transfer coefficients (h x 10^3 BTU/ft^2-sec-°R). Figure taken from Figures 5 and 7 in Gillerlain [36].

Figure 2.20 shows the cone pressure upstream of the fin leading edge normalized by the straight cone pressure, versus the distance upstream of the fin normalized by the fin leading-edge diameter. The unswept fin shows a peak in pressure around two diameters upstream of the fin indicating a shock-induced separation. The location of the separation is consistent with previous experiments with turbulent boundary-layer separation ahead of blunt protuberances. No such separation is seen for the swept fin case.

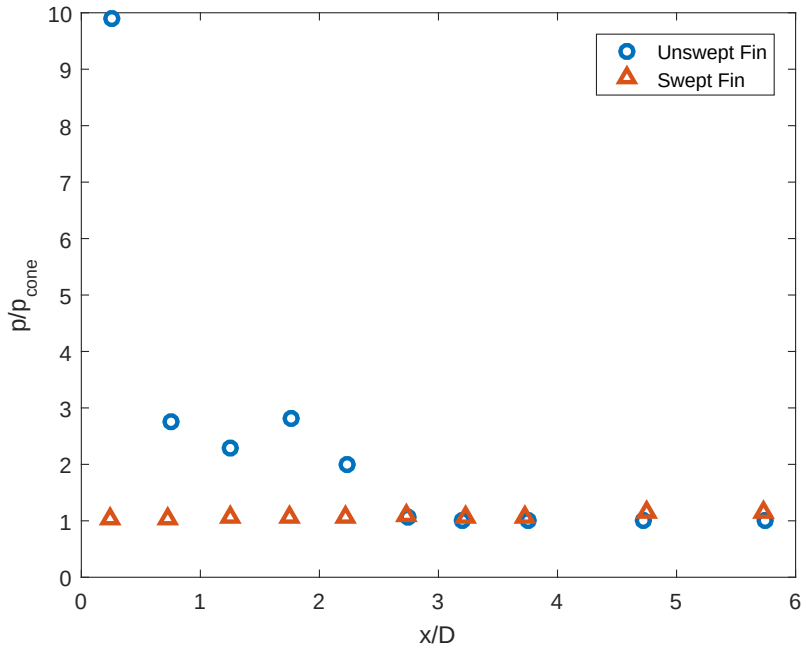

Figure 2.20. Pressure on cone surface upstream of the fin normalized by the pressure for a straight cone at Re = 26 x 10^6 ft^{-1}. The peak in pressure 2D upstream of the the unswept fin indicates a shock-induced separation upstream of the fin. No such peak is seen for the swept fin. Figure redrawn from Gillerlain [36].

Abney and Rochlitz performed experiments on a fin-cone model similar to the geometry used in the present experiments [8,37]. The model consisted of a fin mounted on a 7° half-angle cone. The fin was designed to simulate the inlet cowling of the X-51 scramjet aircraft. Figures 2.21 and 2.22 show the complex fin geometry mounted on the cone. The fin was designed to be completely within the cone bow shock. The model was coated with temperature-sensitive paint to make global heat transfer measurements. The experiments were carried out in the Boeing-AFOSR Mach-6 Quiet Tunnel at Purdue University over a unit Reynolds number range of 7.7 x 10^6 m^{-1} to 11.83 x 10^6 m^{-1}. The tunnel is capable of running with a laminar boundary layer on the nozzle wall (quiet) or with a turbulent boundary layer on the nozzle wall (noisy).

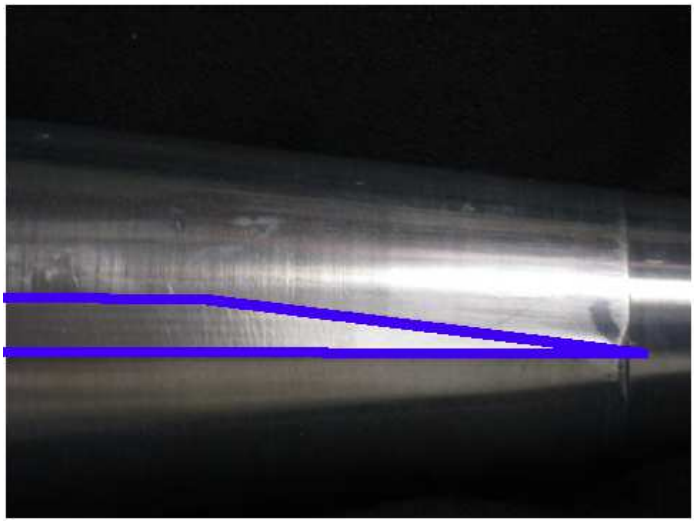

Figure 2.21. Top view of fin mounted on the cone. The fin is outlined in blue to highlight the wedge cross section near the front of the fin. Image taken from Figure A.10 in Abney and Rochlitz [37].

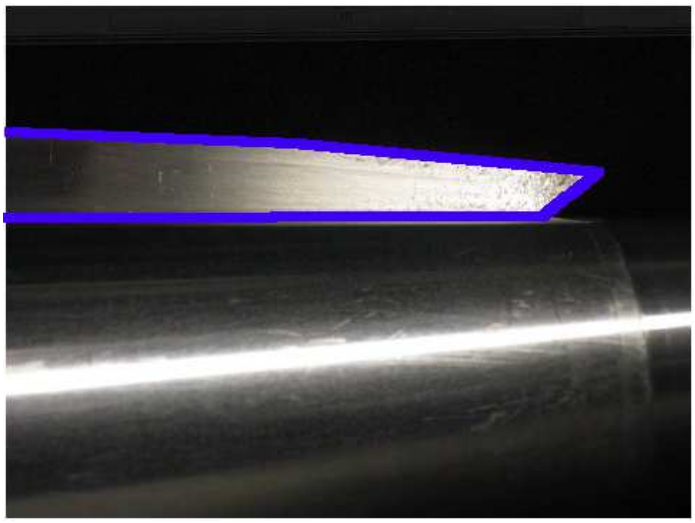

Figure 2.22. Side view of fin mounted on the cone. The fin is outlined in blue to highlight the sweep and leading edge of the fin. Image taken from Figure A.11 in Abney and Rochlitz [37].

Figure 2.23 shows the heat transfer measurements under both quiet and noisy flow. In both images a system of hot streaks is apparent on the cone and fin surface. These streaks spread laterally farther downstream and show an increase in heat transfer. Abney and Rochlitz contend that this is due to boundary-layer transition, however, no pressure fluctuation data are presented to support this. They call the location where spreading begins the "transition front". This front moves upstream as Reynolds number increases. At a similar Reynolds number, the transition front is much farther upstream under noisy flow than under quiet flow. The lateral extent is also much greater.

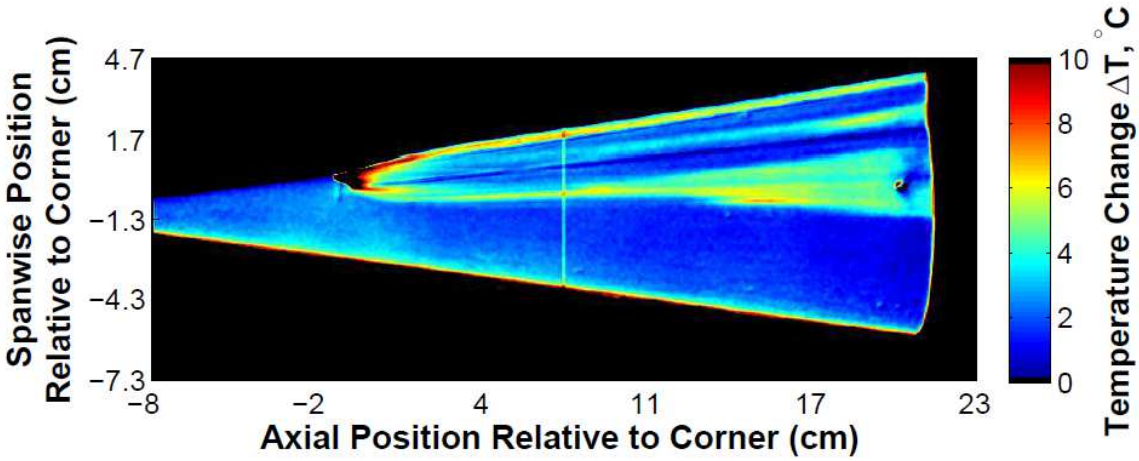

(a) Quiet Flow, unit Re = 10.94 x 10^6 m^{-1}

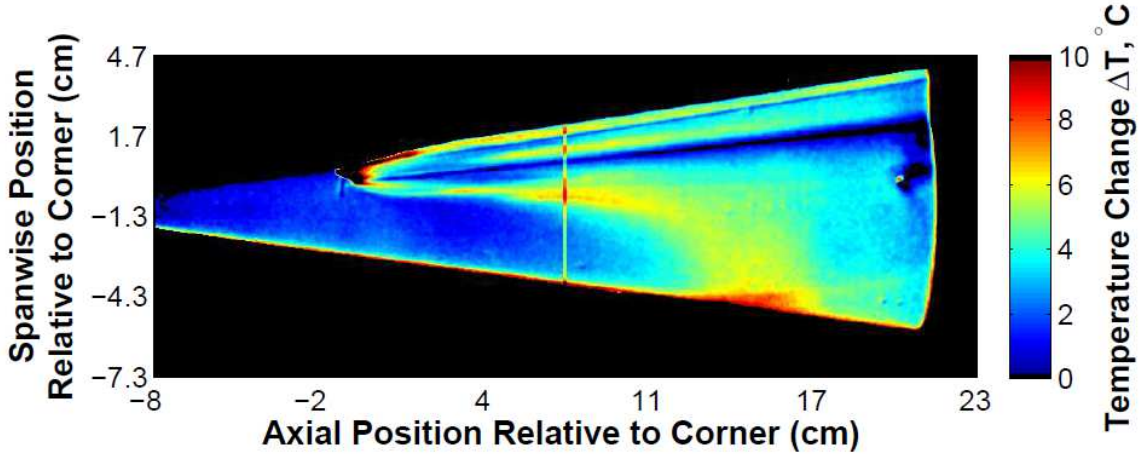

(b) Noisy Flow, unit Re = 10.81 x 10^6 m^{-1}

Figure 2.23. Surface heat transfer measurements indicated hot streaks on the cone and fin surface. The streak pattern is significantly different between quiet and noisy flow at a similar Reynolds number. Images taken from Figures 16 and 17 in Berridge et al. [8].

Chynoweth et al. followed up on the experiments of Abney and Rochlitz by making heat transfer and pressure fluctuation measurements with different fin geometries [7, 38]. The 7° half-angle cone used for the experiment was the same as used by Abney and Rochlitz. The fins had sweep angles of 78°, 75.5°, and 73° and were symmetrically tapered to a sharp leading edge. A schematic of the 73° sweep fin is shown in Figure 2.24 for clarification. The model was tested under quiet flow in the Boeing-AFOSR Mach-6 Quiet Tunnel over a unit Reynolds number range of 6.33 x 10^6 m^{-1} to 9.97 x 10^6 m^{-1}. Heat transfer was measured using the same temperature-sensitive paint technique as Abney and Rochlitz. The model was instrumented with PCB132A31 fast pressure transducers in the corner region to make boundary-layer pressure fluctuation measurements. Figure 2.25 shows heat transfer measurements for the cone with a 73° sweep fin. A vortex structure was measured, similar to that found by Abney and Rochlitz. For larger fin sweep angles, the measured heat transfer was reduced.

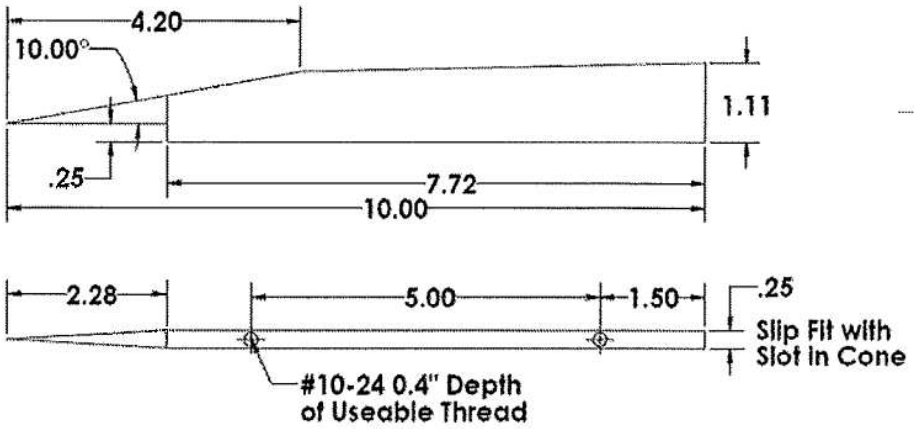

Figure 2.24. Schematic of the 73° sweep fin. Figure taken from Figure 36 in Chynoweth et. al [38].

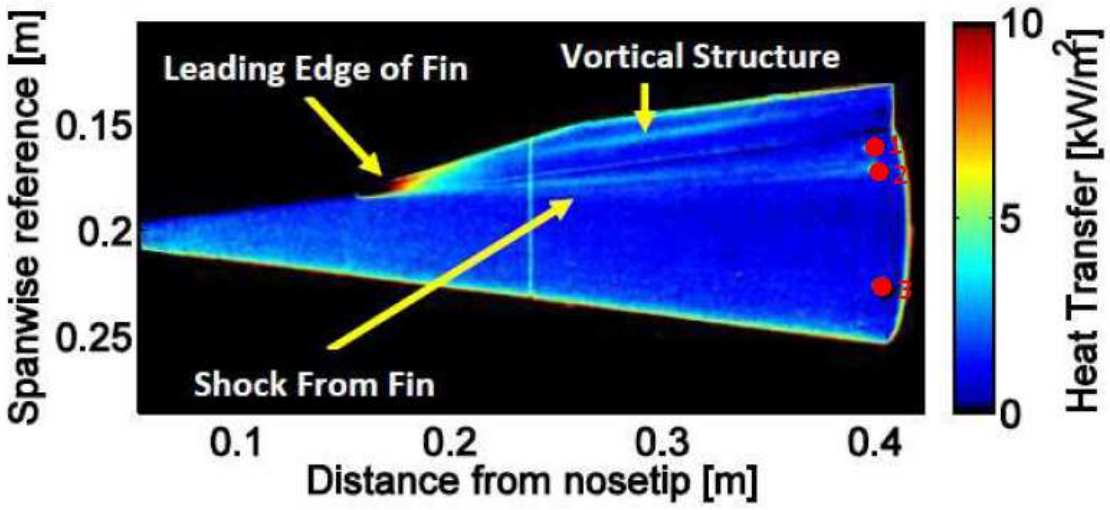

Figure 2.25. Heat transfer for the cone with the 73° sweep fin at a unit Reynolds number of 9.68 x 10^6 m^{-1}. Figure taken from Figure 4 in Chynoweth et. al [7].

Also shown in Figure 2.25 are the locations of the pressure sensors shown as red dots. The sensor at location 2 is very close to the outside of the streak. Power spectra of the pressure fluctuations for the sensor at this location is shown in Figure 2.26 for a range of unit Reynolds numbers and a 78° sweep angle. The power spectra show a peak at a frequency in the range expected for the second-mode instability. This peak becomes larger as the unit Reynolds number increases. Figure 2.27 shows power spectra for the same sensor with a 73° sweep fin. The second-mode peak amplifies with increasing unit Reynolds number along with the broadband pressure fluctuations, indicating boundary-layer transition. At a unit Reynolds number of 8.4 x 10^6 m^{-1}, transition is measured at the sensor near the streak for the 73° sweep fin, but not for the 78° fin. The results indicate that increasing sweep delays transition.

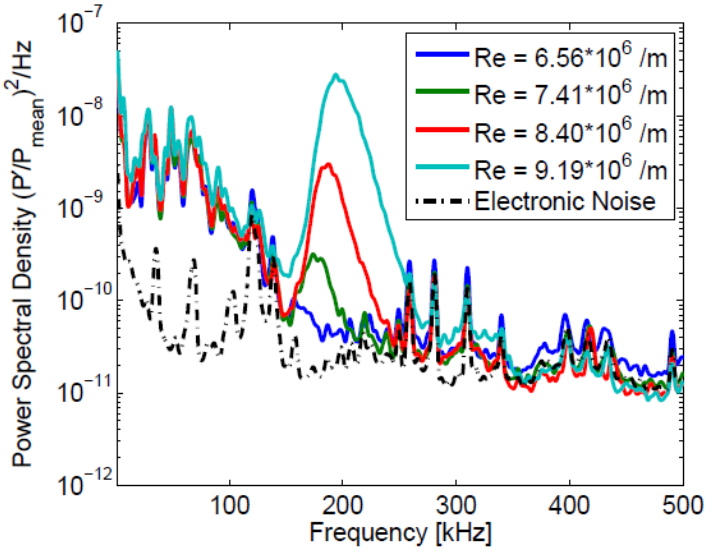

Figure 2.26. Pressure fluctuation power spectra for the sensor near the streak with a 78° sweep fin. Figure taken from Figure 8 in Chynoweth et. al [7].

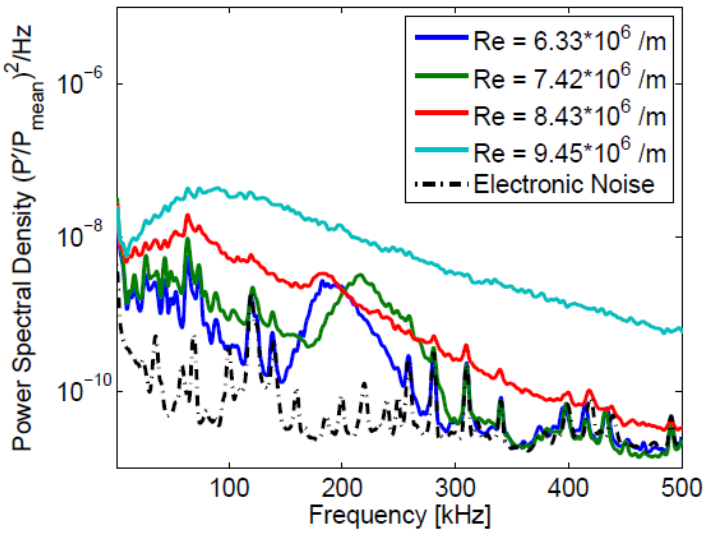

Figure 2.27. Pressure fluctuation power spectra for the sensor near the streak with a 73° sweep fin. Figure taken from Figure 9 in Chynoweth et. al [7].

3. FACILITY, MODELS, AND INSTRUMENTATION

3.1 Boeing/AFOSR Mach-6 Quiet Tunnel

The Boeing/AFOSR Mach-6 Quiet Tunnel (BAM6QT) is one of two hypersonic quiet tunnels in the United States. The BAM6QT is a Ludwieg tube design with a long driver tube, converging-diverging nozzle, and a vacuum tank at the downstream end. A schematic of the tunnel is shown in Figure 3.1. This design allows for short times between runs and low operational costs. Whereas many conventional tunnels may only be capable of a few runs per day, the BAM6QT is capable of about one run per hour.

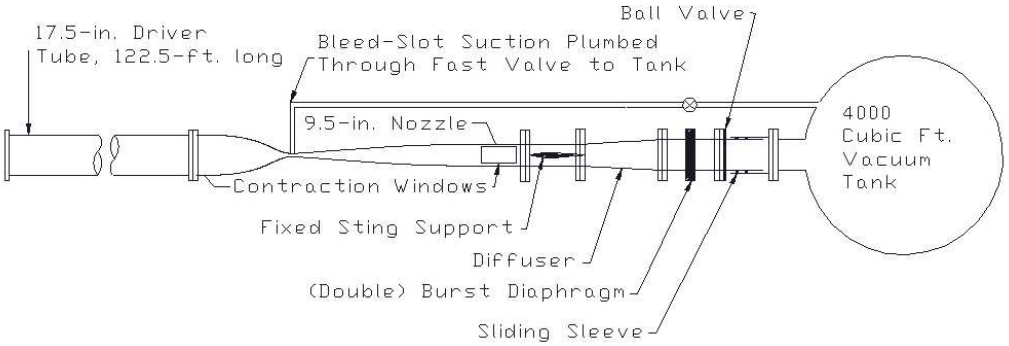

Figure 3.1. Schematic of the BAM6QT.

Flow is initiated by bursting two aluminum diaphragms that separate the pressurized driver tube from the vacuum tank. A gap between the two diaphragms is maintained at half the difference between the driver pressure and the vacuum pressure. When the gap is evacuated, the diaphragms burst, a shock propagates downstream into the vacuum tank, and an expansion wave propagates upstream into the driver tube initiating Mach 6 flow as it passes through the throat. Each time the expansion

wave reflects between the two ends of the driver tube the stagnation pressure drops 1-2%, resulting in a 200 ms period of quasi-constant flow conditions. The tunnel remains started for approximately 4 seconds under quiet flow.

Turbulent boundary layers on the nozzle wall are the primary reason for pitot fluctuations in wind tunnels [3]. The nozzle of the BAM6QT is specially designed to achieve quiet flow by maintaining a laminar boundary layer. The nozzle has a slow expansion with a large radius of curvature to reduce the growth of Görtler vortices. The throat is also polished to a mirror finish reducing the possibility of roughness-induced transition. The throat is equipped with bleed slots that remove the existing boundary layer from the contraction section and initiate a new laminar boundary layer. The tunnel can be run in noisy mode simply by closing the bleed-slot valves, in which case the Mach number is 5.8 due to the thicker wall boundary layer. The nozzle-wall boundary layer remains laminar past the end of the nozzle up to the maximum quiet freestream Reynolds number. When testing began, the maximum quiet Reynolds number was roughly 12.4 x 10^6 m^{-1} which corresponds to an initial stagnation pressure of 170 psia. Tunnel performance was diminished when the tunnel was opened for maintenance upstream of the throat. After this maintenance was completed, the maximum quiet Reynolds number was restored to only about 10.5 x 10^6 m^{-1} with an initial stagnation pressure around 135 psia. Presumably, this is due to a reduction in the quality of the throat finish. The first four entries of this test program were conducted with the original maximum quiet Reynolds number.

3.1.1 Tunnel Condition Measurement and Computation

The tunnel flow properties at any point in time during the run can be calculated using the initial stagnation temperature along with stagnation pressure measurements. A thermocouple at the far upstream end of the driver tube is used to measure the pre-run stagnation temperature. The temperature is measured after the tunnel is allowed to equilibrate for 10 minutes after filling. Uncertainties in the measurement

due to streamwise and radial temperature variations is assumed to be small after this settling process. The pressure is measured with several devices. A Kulite XTEL-190-500A sensor mounted on the wall at the contraction inlet is used to measure the stagnation pressure. The pressure in the driver tube during the tunnel filling process is monitored with a Paroscientific Inc. model 740 Digiquartz Portable Standard pressure gauge. A linear calibration of the contraction Kulite voltage is made every tunnel entry, by comparing to the pressure measured by the Paroscientific gauge. An example calibration is given in Figure 3.2. In addition, a Kulite XCQ-062-15A sensor in the diffuser section is used to trigger the scopes at the beginning of the run. The scopes are triggered by the drop in pressure as the expansion fan moves upstream.

Making isentropic and perfect gas assumptions, the stagnation temperature at any time can be calculated using Equation 3.1,

$$T_0 = T_{0,i}\left(\frac{p_0}{p_{0,i}}\right)^{\frac{\gamma-1}{\gamma}} \tag{3.1}$$

The initial stagnation temperature ($T_{0,i}$) is recorded at the beginning of the run. The stagnation pressure (p_0) and initial stagnation pressure ($p_{0,i}$) are measured by the Kulite in the contraction.

The static temperature, static pressure, and freestream Reynolds number can be calculated using the following equations. Viscosity (μ) is found as a function of temperature using Sutherland's law.

$$T = T_0\left(1 + \frac{\gamma-1}{2}M^2\right)^{-1} \tag{3.2}$$

$$p = p_0\left(1 + \frac{\gamma-1}{2}M^2\right)^{-\frac{\gamma}{\gamma-1}} \tag{3.3}$$

$$Re = \frac{pM}{\mu(T)}\sqrt{\frac{\gamma}{RT}} \tag{3.4}$$

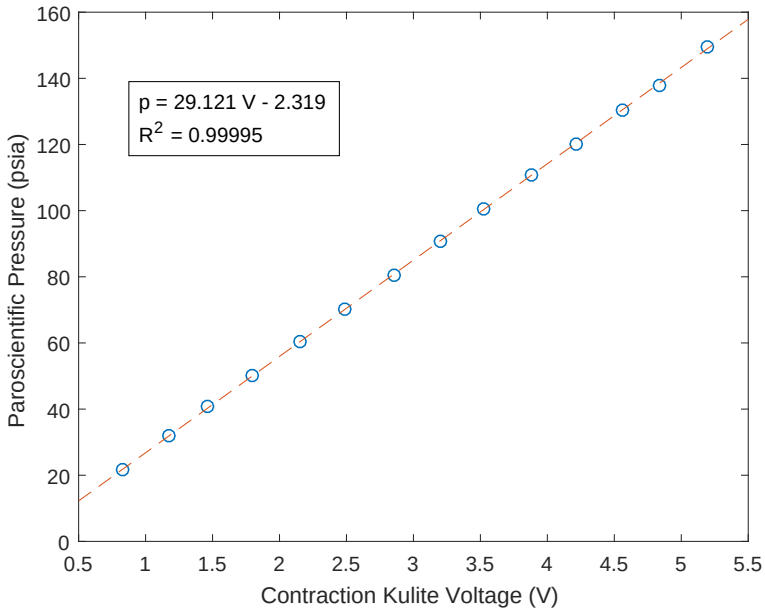

Figure 3.2. Example contraction Kulite calibration from Entry 5.

3.1.2 Run Characteristics

The stagnation pressure drops throughout the run as the expansion wave reflects back and forth between the contraction and the end of the driver tube. This results in periods of quasi-steady stagnation pressure as shown in Figure 3.3. As the pressure drops, so does the temperature and Reynolds number. Therefore, data can be collected over a range of Reynolds numbers during one run.

A Senflex hot film array on the nozzle wall was used to verify that the flow was quiet and to check for turbulent bursts on the nozzle wall. Data during a turbulent burst is not analyzed. Figure 3.3 shows some of these turbulent bursts at around 1.5 seconds and between 2.8 and 3.7 seconds. The hot film also shows tunnel startup and unstart as indicated by the large voltage fluctuations near the start and end of the signal, 0.25 and 3.7 seconds respectively. A wave from this hot film array has been shown to cause streaks of increased heating on the aft end of some large models [39].

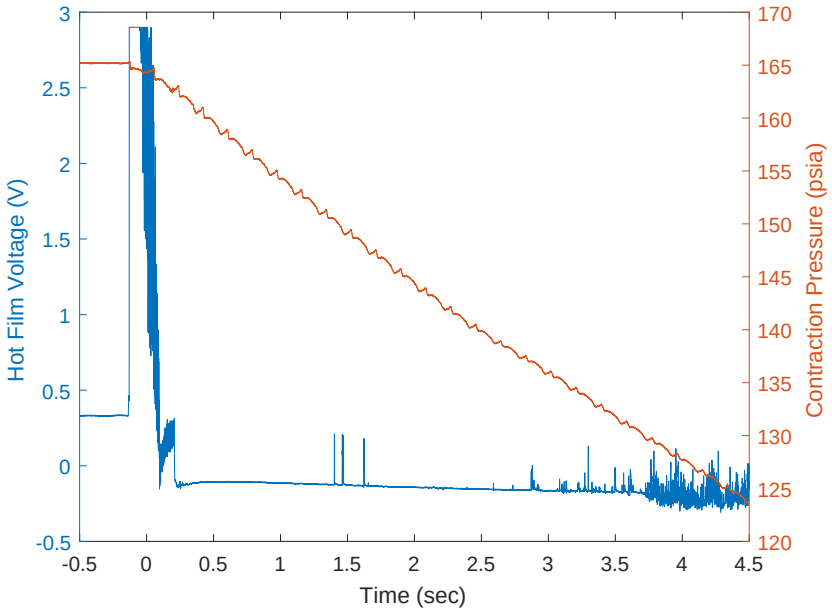

Figure 3.3. Example hot film and stagnation pressure trace for a max quiet run at 170 psia intial stagnation pressure. Spikes near 1.5 seconds are turbulent bursts.

3.2 Fin-Cone Models

Two models were used during testing. The first was developed for class projects in the AAE 520 course at Purdue University. The second model was developed specifically for the present experiment. Both are 7° half-angle cones and were fabricated out of 6061-T6 aluminum in the ASL machine shop at Purdue University. The drawings are included in the Appendix.

3.2.1 Single-Fin Model

The single-fin model was originally developed by Andrew Abney and Henry Rochlitz to test inlet geometries [37]. It was subsequently used by Brandon Chynoweth, Ryan Henderson, and George Moraru for testing sharp highly-swept fins [38]. Both of these projects were helpful when designing how the fins are attached and when choosing

sensor locations for the present three-fin model. For the purposes of this test program, the older single-fin model was used to make comparisons between quiet and noisy flow.

A schematic of the single-fin model is shown in Figure 3.4. This model is a sharp 7° half-angle cone with a slot machined to accept a fin which is attached via two screws. Holes drilled on the opposite side of the cone from the fin provide access to the screws. These holes are filled with dental plaster and sanded smooth before any runs are made. The fin used with this model has a hemispherically blunted leading edge. The slot width is machined to 0.35 inches, setting the fin leading edge radius to 0.175 inches. The fin starts 4 inches from the sharp nosetip and is swept back 75°. It intersects the cone surface at right angles with no fillets. Rope caulk was used to fill any gaps between the fin and the cone surface near the fin root. Alternatively, a blank that is flush with the surface can be used to test a simple straight-cone case. There are three 0.128-inch diameter sensor holes on both sides of the slot at 17°, 34°, and 90° azimuthally from the fin slot center line. The holes at 17° and 34° are 0.563 inches from the base. The outermost hole is 0.50 inches from the base. Holes drilled in the base of the cone make a path for the sensor wires. The model is attached to the sting mount via threads machined into the back of the model. It is nominally at 0° angle of attack during testing, but the capability for adjustment is minimal. The full drawings are included in the Appendix.

3.2.2 Three-Fin Model

To test a wider parameter space, a second fin-cone model was designed as shown in Figure 3.5. Three slots were machined, spaced equally around the azimuth of the model. The slot thicknesses were chosen to be 1/8 inches, 3/16 inches, and 1/4 inches. Fins of 70° and 75° sweepback were made for each slot size. These fins have hemispherical bluntness making the leading edge radii 1/16 inches, 3/32 inches, and 1/8 inches. The fin intersects the cone at right angles with no fillets. The slots are

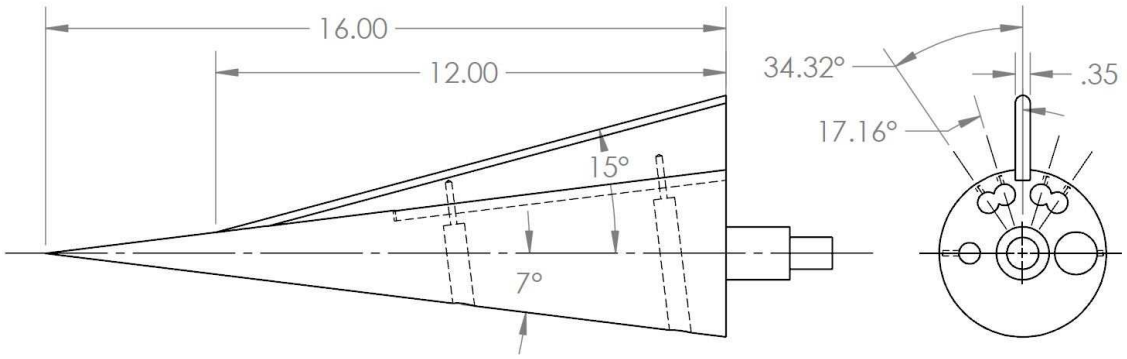

Figure 3.4. Schematic of the single-fin model designed by Abney and Rochlitz [37]. The model is a 7° half-angle cone with a sharp nosetip. One fin was tested with $R_{LE} = 0.175$" and 75° sweep. Dimensions are in inches.

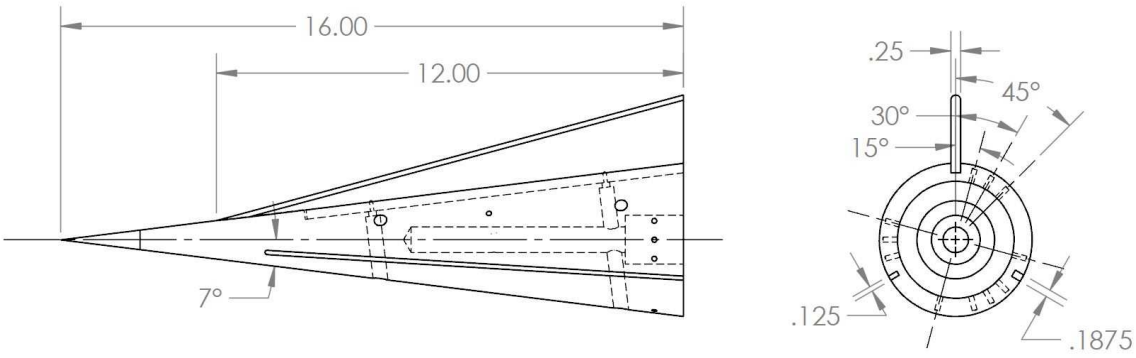

Figure 3.5. Schematic of the three-fin model. The model is a 7° half-angle cone with interchangeable nosetips. Six fins were tested with variable leading edge radius and sweep. Dimensions are in inches.

fitted with blanks when not in use. The blanks are flat-topped rather than machined flush for ease of manufacture, however at most they are only 0.003 inches above the surface. The fins and blanks are attached via screws through two access holes drilled from the opposite side of the cone. Like the single-fin model, these holes are filled with dental plaster and sanded before testing. These access holes appear in temperature-sensitive-paint images as black areas. Any gaps between the fin and cone surface are filled using rope caulk. Three stainless-steel interchangeable nosetips were created. The nosetip radii were measured using a Moticam 3 microscope camera. The measurements are shown in Figure 3.6. The circles were drawn using the Moticam software after calibrating to a manufacturer-supplied slide.

In total there were 18 different configurations possible for each angle of attack, of which 14 were tested. Table 3.1 lists the configurations tested at 0° angle of attack. In addition, a few runs at 4° angle of attack were made as shown in Table 3.1.

There are a total of 14 sensor holes on the three-fin model. Eleven of these holes are spaced around the azimuth at 0.75 inches from the aft end of the model. There are three sensors in the vicinity of the corner region, at 15°, 30°, and 45° from each fin centerline. Four PCBs are spaced equally around the azimuth to aid alignment of the model within the tunnel as detailed by Chynoweth [40]. Three sensors are placed between the fins further upstream, at 5 inches from the aft end of the cone. All of the sensors can be accessed from the aft end of the cone.

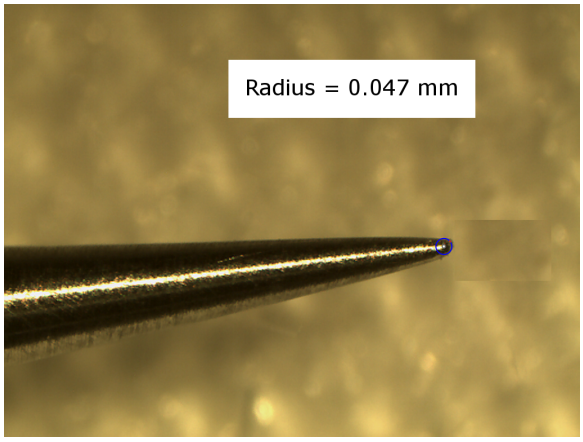

(a) Nominally sharp nosetip.

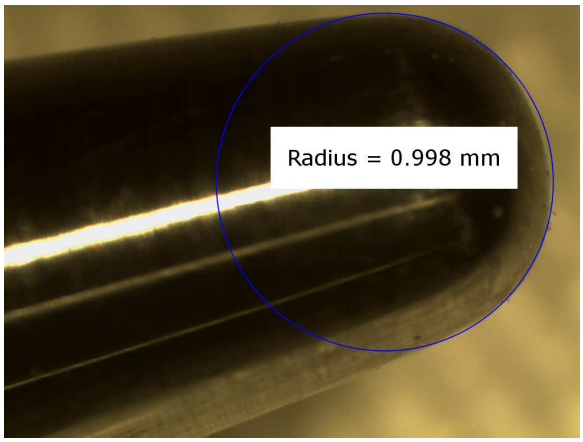

(b) 1mm radius nosetip.

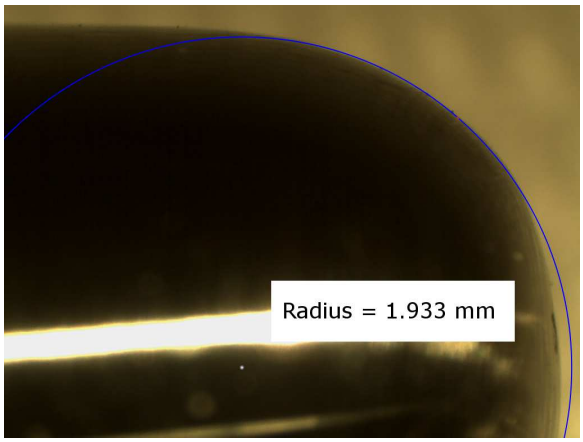

(c) 2mm radius nosetip.

Figure 3.6. Nosetip radii measured with Moticam 3 microscope camera.

Table 3.1. Tested fin-cone configurations.

LE Radius (in.)	Fin Angle (deg.)	Nosetip Radius (mm)
1/16	15	Sharp
		1
	20	Sharp
		1
3/32	15	Sharp
		1
	20	Sharp
		1
1/8[1]	15[1]	Sharp[1]
		1
		2
	20	Sharp
		1
		2

[1] Also run at 4° angle of attack

3.3 Model Instrumentation, Setup, and Data Reduction

The models are instrumented with Schmidt-Boelter heat transfer gauges and PCB132A31 fast pressure sensors. The single-fin model has 6 potential sensor locations, 3 on either side of the fin. The three-fin model has 14 potential sensor locations, however only a subset of these was used for each entry. The sensor calibrations and the locations for each entry are included in Appendix C. The models are painted with temperature sensitive paint to make global heat-transfer measurements.

3.3.1 PCB Fast Pressure Transducers

PCB132A31 (PCB) fast pressure transducers made by PCB Piezotronics, Inc. have been used extensively in past experiments in the BAM6QT to measure high-frequency boundary-layer instabilities. The sensors are high-pass filtered at 11 kHz with a resonant frequency exceeding 1 MHz. The sensor is 0.125 inches in diameter with a 0.03 inch square sensing element. The location of the sensing element on the sensor face is not known. Therefore, the exact measurement location is only known within $\pm 2^{\circ}$ azimuthally at 0.75 inches from the base.

When the sensor casing is in contact with the aluminum model, significant electrical noise is introduced. Several methods were used to insulate the sensor from the model. Paint overspray into the sensor holes act as an insulating layer. The sensors are installed using nail polish which also acts as insulation. Nail polish is used as an adhesive for the sensors because it is strong yet can be easily dissolved using acetone for removal. However, the acetone can remove the epoxy on the face of the sensor which covers the sensing element. It is not well understood how the epoxy transmits pressure to the sensing element, but degradation of the epoxy could conceivably affect the sensor accuracy [41]. The PCBs are calibrated by PCB Piezotronics, Inc. The accuracy of these calibrations is uncertain as they are made using a single point measurement. Continuing efforts at Purdue University attempt to better calibrate these sensors [41, 42].

Computing a power spectral density (PSD) of the pressure fluctuations can reveal high-frequency fluctuations within the boundary layer. Each PSD is calculated using Welch's method for a 0.1 second time sample with a Hamming window, a frequency resolution of 2 kHz, and a 50% overlap. Prior to analysis, the mean is subtracted from the pressure fluctuations and they are normalized by the static pressure on a 7° half-angle sharp cone, as determined using a Taylor-Maccoll solution at 0° angle of attack. This normalization is used for all geometries tested and for data from all of the sensor locations. Future improvements in normalization might require the mean pressure from a CFD solution.

3.3.2 Schmidt-Boelter Heat Transfer Sensors

Model number 8-1-0.25-48-20835TBS Schmidt-Boelter (SB) gauges manufactured by the Medtherm Corporation were used to measure heat transfer and to calibrate the temperature sensitive paint. The SB sensors are 0.125 inches in diameter. The sensors consist of a series of thermocouples called a thermopile. The heat transfer can be determined by measuring the temperature difference between the thermocouples. The T-type thermocouple at the face of the sensor, flush with the cone surface, is measured before each run to be used as a reference temperature during temperature-sensitive-paint data reduction. This value is collected using an Agilent 34401A digital multimeter. The heat transfer voltage is amplified using a SR560 Stanford Research Systems Low Noise Preamplifier with a gain of 100 and a low-pass filter cutoff frequency of 30 Hz. The sensor is mounted outside of the fin interaction region on the model to give a better temperature-sensitive-paint calibration. Two sensors are sometimes used when several fin leading-edge radii are tested.

3.3.3 Oscilloscopes

Measurements of tunnel conditions, PCB pressure fluctuations, and SB heat transfer were all collected using oscilloscopes. A combination of Tektronix DPO7054,

DPO7104, and DPO5034B oscilloscopes were used. DPO7054 and DPO5034B model scopes are capable of storing 5 seconds of data at a 5 MHz sampling rate. The DPO7104 model scope has less internal memory and is only capable of storing 1.8 seconds of data at a 5 MHz sampling rate. Pressure data scopes were usually sampled at 2 MHz which satisfies the Nyquist criteria for a 1 MHz measurement. Generally one scope, set to sample around 20 kHz, was used for tunnel-condition measurements and the camera signal. The oscilloscopes were set to sample in Hi-Res mode, which increases the vertical resolution by sampling at the maximum rate and digitally averaging. Hi-Res mode also acts as an anti-aliasing filter. Data were collected for 0.5 seconds before the trigger and 4.5 seconds during the run. The sampling rates for each entry are given in Appendix C.

3.3.4 Temperature Sensitive Paint

The model is coated in temperature sensitive paint (TSP) to obtain global heat transfer measurements. The TSP consists of a luminophore molecule dissolved in ethanol and combined with a clear coat which can then be sprayed onto the model. A layer of white paint is applied between the model and the TSP layer to act as insulation and to provide a better signal-to-noise ratio [43]. The TSP can be excited with a blue LED which causes the luminophore molecule to release a photon at a longer wavelength. The temperature of the luminophore is inversely proportional to the intensity of the light emitted. The luminophore molecule used in the BAM6QT is 99.95% Tris(2,2-bipyridyl)ruthenium(II) chloride hexahydrate, also known as Ru(bpy). Figure 3.7 shows the painted and instrumented model while the nozzle exit is open. When the tunnel is closed the model slides into view of a 14 inch by 7 inch plexiglass window for imaging.

The paint thickness was measured using an Elcometer 456 capacitance gauge and typically averaged around 100 microns. The paint thickness increases the leading-edge radius of the fin by roughly 0.004 inches. A forward-facing step is formed

on the cone surface upstream of the fin due to the paint thickness. This step was sanded smooth and was measured to be less than 20 microns using a Zego ZeGage optical profilometer, which is an order of magnitude smaller than the boundary layer thickness at that location. The TSP is also sanded smooth near the intersection of the fin and cone surfaces to reduce any chance of discontinuities in the corner.

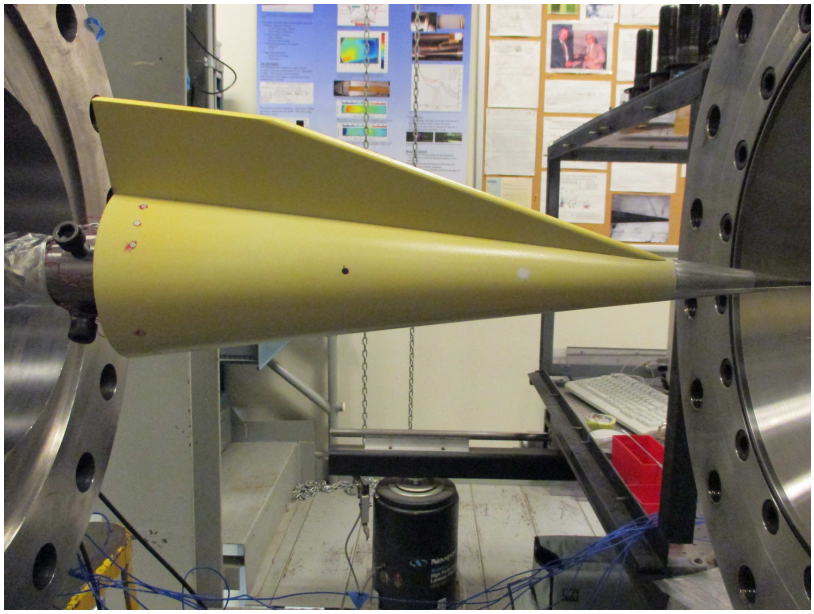

Figure 3.7. Model ready to install in tunnel with TSP applied.

3.3.5 TSP Processing

Images are obtained using an ISSI PSP-CCD-M 14-bit camera. The 465 nm blue LED light used to excite the TSP molecule is filtered from the image using an orange 550 nm long-pass filter. Images with all the lights off, or "dark" images, and images with the LED on and no flow, or "off" images, are taken prior to the run after the 10 minute settling period. Normally 15 dark and off images were taken and averaged. During the run, between 75 and 90 "on" images were taken. The camera was triggered using a 15 Hz signal from a function generator. The exposure time was altered between runs to keep the intensity of the image just below saturation levels.

The images are a matrix of the intensity of the pixels. The change in temperature from the "off" to the "on" condition can be calculated as a function of the intensity of the images, I:

$$\Delta T = f\left(\frac{I_{on} - I_{dark}}{I_{off} - I_{dark}}\right) \tag{3.5}$$

As detailed by Sullivan, et al., the calibration of the intensity of the TSP molecule and temperature change is given by Equation 3.6 [43]. The "off" condition temperature, T_{ref}, is taken from the surface thermocouple of the SB gauge before the run.

$$\Delta T = (363 - T_{ref})\left(1 - \frac{I_{on} - I_{dark}}{I_{off} - I_{dark}}\right) \tag{3.6}$$

Heat transfer can be inferred from the change in temperature if a few assumptions are made. It is assumed that heat transfer is one-dimensional, in the wall normal direction. In addition the heat transfer through the insulator layer is assumed to be linear. Finally, the model temperature, T_{model}, is assumed to be a constant. Fourier's law can then be simplified for the local heat flux as in Equation 3.7, where L is the thickness of the insulating layer.

$$\dot{q} = -\kappa \nabla T = \frac{\kappa}{L}(T - T_{model}) \tag{3.7}$$

The change in temperature is defined as in Equation 3.8. This can be substituted into Equation 3.7 to give heat transfer as a function of temperature change and other measured values.

$$\Delta T = T - T_{ref} \tag{3.8}$$

$$\dot{q} = \frac{\kappa}{L}(\Delta T + T_{ref} - T_{model}) \tag{3.9}$$

The TSP is calibrated using an SB heat transfer gauge located outside of the fin interaction region. A small patch near this sensor, as in Figure 3.8, is compared to the heat transfer measured by the SB. A linear regression for many successive images

determines the value of $\frac{\kappa}{L}$ and T_{model} that provides the best fit. Figure 3.9 shows the points chosen for calibration as the temperature drops after tunnel start-up. Figure 3.10 shows the linear calibration of temperature and heat transfer. The relationship is clearly not linear, but the linear calibration provides a fit with coefficient-of-determination values typically greater than 0.95.

Only the TSP on the cone is calibrated with any certainty due to limited space for SB sensors on the fin. There is no way to ensure that the paint on the cone and fin is uniform. The fins are thin and heat transfer was often measured to be higher if the length of time between runs was short. It is also unclear whether the heat transfer assumptions made during data reduction would hold for the fins. The fins are quite thin and the assumption that T_{model} is constant is not accurate. Therefore, heat transfer measurements on the fin should only be considered only qualitatively. Relative magnitudes could be reliable between runs of the same entry and fin. Other heat transfer measurement methods are being considered for future tests.

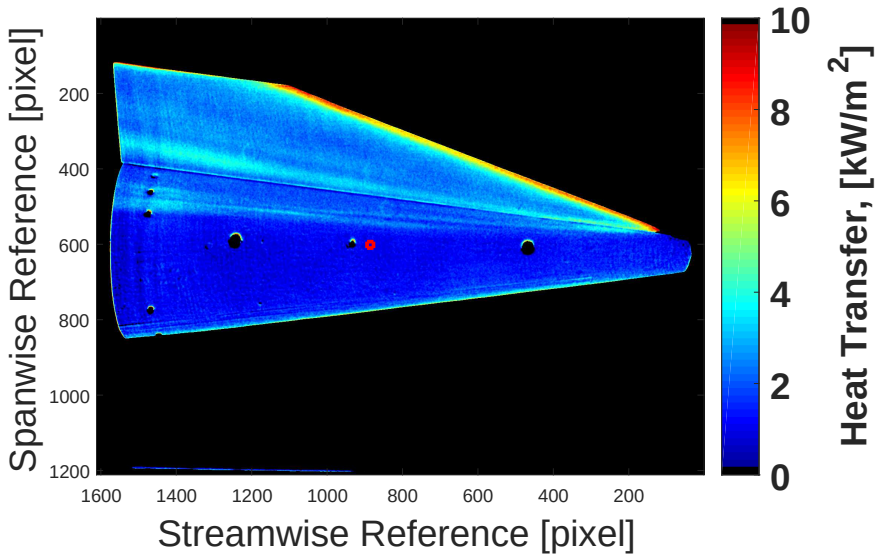

Figure 3.8. Example TSP image of the three-fin model. The patch chosen for calibration is indicated by a red square.

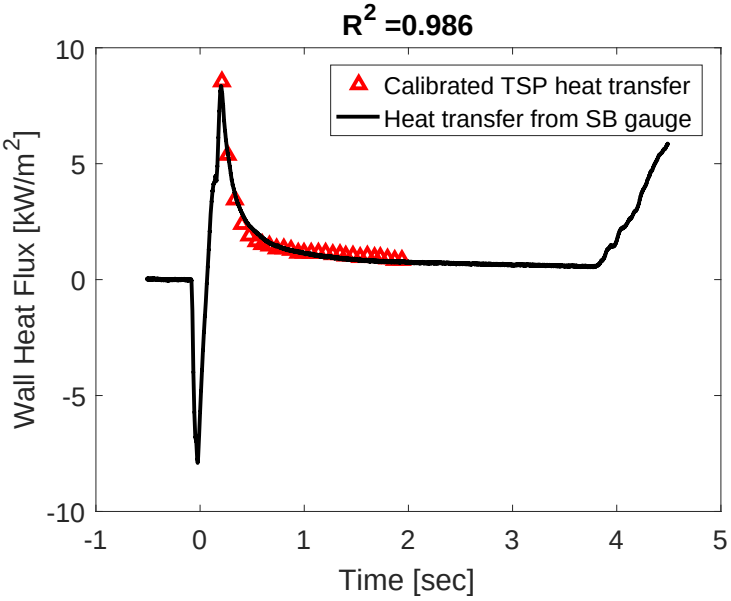

Figure 3.9. Example thermocouple heat transfer trace shown in black. Red triangles are the points chose for calibration.

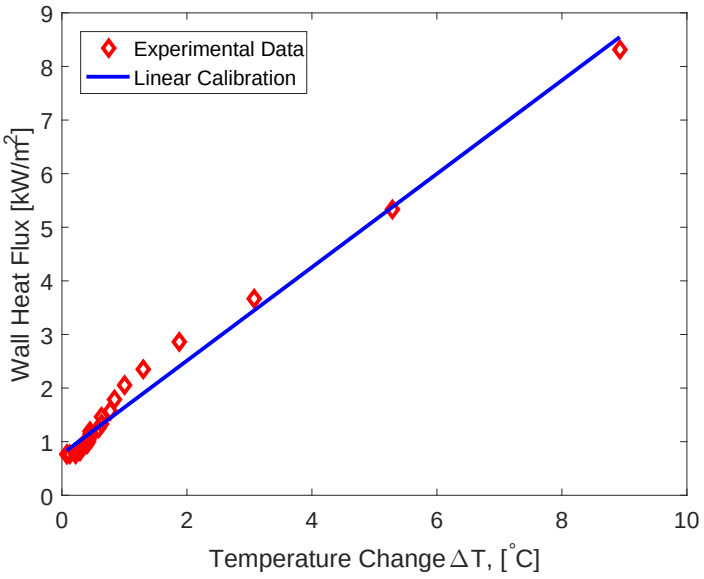

Figure 3.10. Example linear fit of heat transfer data.

3.3.6 Typical Experimental Setups

The single-fin model screws directly into the sting and is assumed to be at 0° angle of attack. The three-fin model makes use of a fine angle of attack adapter that is adjusted to align the model with the freestream. The model is centered to 0.0° by measuring the second-mode frequency at 4 sensors spaced equally around the azimuth as shown in Figure 3.11. During this process, no fins are attached and the fin slots are fitted with blanks. Adjustments are made by comparing second-mode frequencies on opposite sensors. If the frequency is higher for one sensor than the other, it means that the boundary layer is thinner on that side of the cone (i.e. windward). A screw on the sting adapter positioned downstream from each sensor can be tightened or loosened to either decrease or increase the angle of attack, respectively. The screws are adjusted until the second mode peaks appear to coincide. A full turn corresponds to an angle change of 0.36° [44].

Figure 3.12 shows the second-mode peaks in a PSD of the pressure fluctuations before and after alignment. Before adjustment, the percent difference in second-mode frequency is 16% for PCBs 2 and 9, which are opposite each other. The frequency for PCB2 is higher, and therefore PCB 9 on the windward side. A full turn was applied to the screw downstream of PCB9 pushing that side of the cone into the flow. After adjustment, the percent difference in the second-mode frequency is 1.7% for PCBs 2 and 9. Similarly, the percent difference in second-mode frequency before adjustment for PCBs 1 and 6 is 8.8%. The frequency for PCB6 is higher, and therefore PCB 6 on the windward side. A half turn is applied to the screw downstream of PCB1. After adjustment, the percent difference is reduced to 0.9% between PCBs 1 and 6. The sensitivity of the second-mode frequency to angle of attack for this model and sensor locations is about 100 kHz per degree change of angle of attack or yaw.

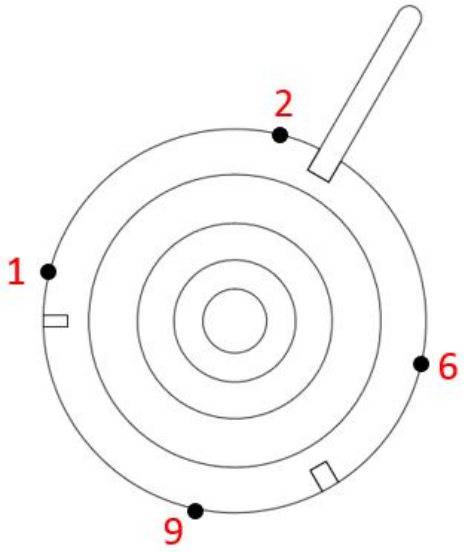

Figure 3.11. PCBs around the azimuth used for aligning during Entry 6.

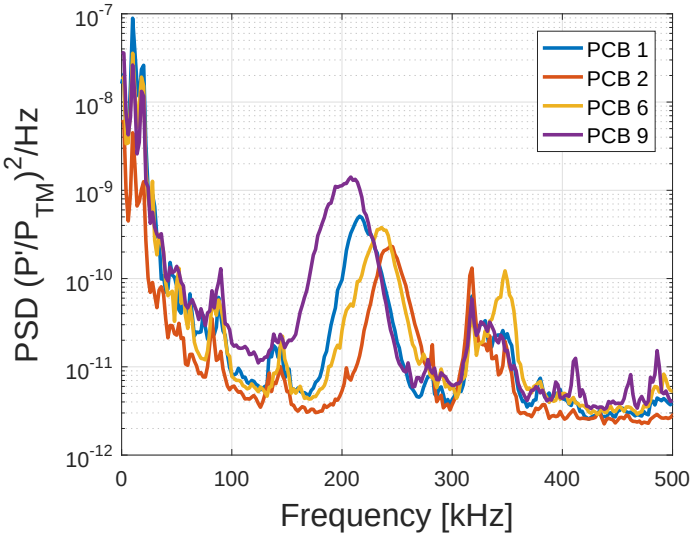

(a) Initial run data show model is misaligned (Run 601, unit Re = 9.13 x 10^6 m^{-1}, quiet flow). Second-mode frequencies are 16% different between PCBs 2 and 9, and 8.8% different between PCBs 1 and 6.

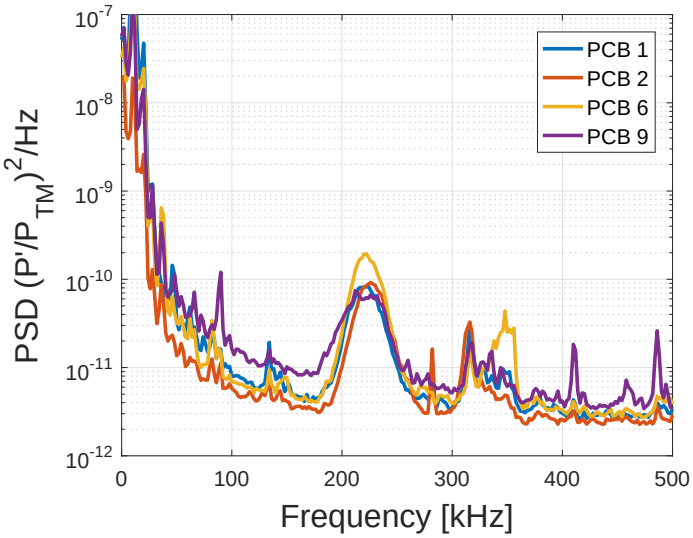

(b) After adjustment, the peaks coincide and the model is at 0.0° angle of attack (Run 603, unit Re = 9.27 x 10^6 m^{-1}, quiet flow). Second-mode frequecies are within 1.7% of each other after adjustment.

Figure 3.12. Model alignment using the second-mode frequency and the fine angle of attack adapter.

Camera Setup for 0° Angle of Attack Runs

For runs at 0° angle of attack, the model is rolled 30° towards the camera in order to have a better viewing angle. Figure 3.13 shows a typical camera setup for a 0° angle of attack run. In this case only one fin slot was used, so 6 PCBs were mounted. PCBs 1-3 are used for measurements in the corner region. PCBs 1, 4, 5, and 6 are spaced 90° apart and are used for aligning the model. The SB is located farther upstream and is within the camera field of view but outside of the fin interaction region.

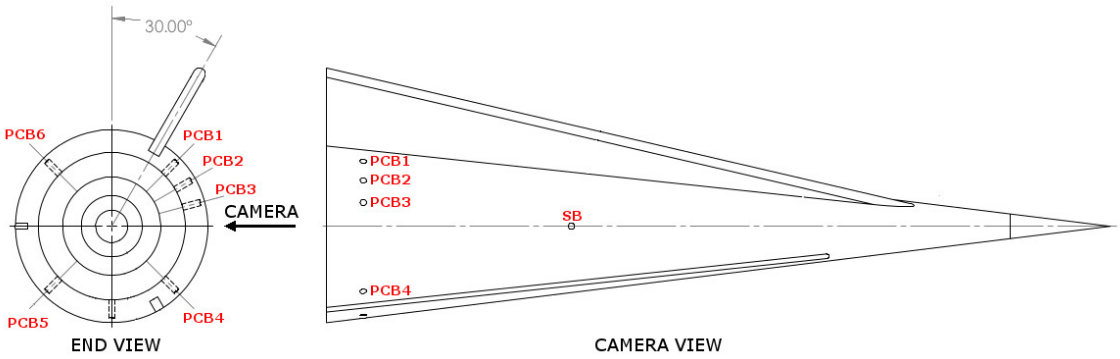

Figure 3.13. Typical camera and model set up for 0° angle of attack.

Camera Setup for 4° Angle of Attack Runs

During Entry 3, the cone was tested at 4° angle of attack. The model was tested in two orientations with respect to the freestream: (1) with the fin on the windward ray, and (2) with the fin on the yaw side of the cone. Figure 3.14 shows the orientation where the fin is on the windward ray. Unlike the tests at 0° angle of attack, the fin is not rolled towards the camera. The camera setup for the orientation with the fin on the yaw side is shown in Figure 3.15. The fin is on the side 90° azimuthally from the windward and leeward rays. The model was imaged from two separate angles. The first, Camera 1, viewed the fin leading edge. After these tests, the cone and sting

mount were rolled so that the cone was in the Camera 2 position. In this position, the camera viewed the leeward ray of the cone with the fin still on the yaw side.

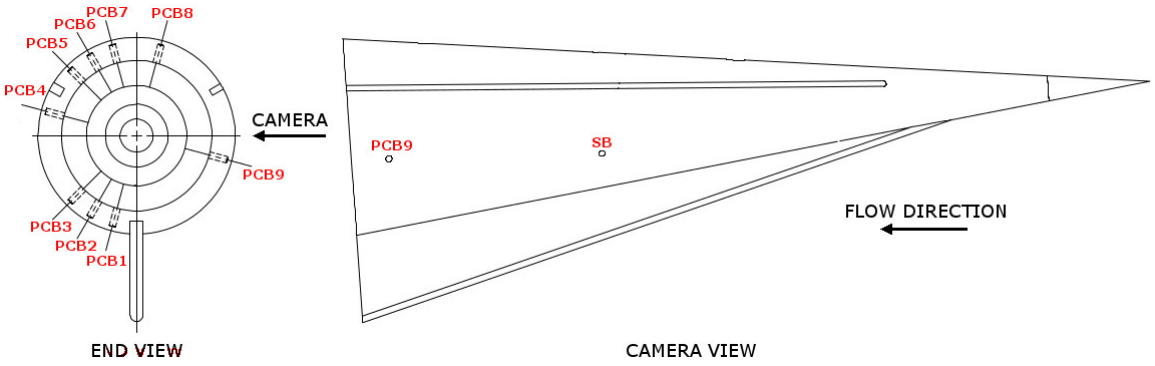

Figure 3.14. The camera and model set up for 4° angle of attack with the fin on the windward ray.

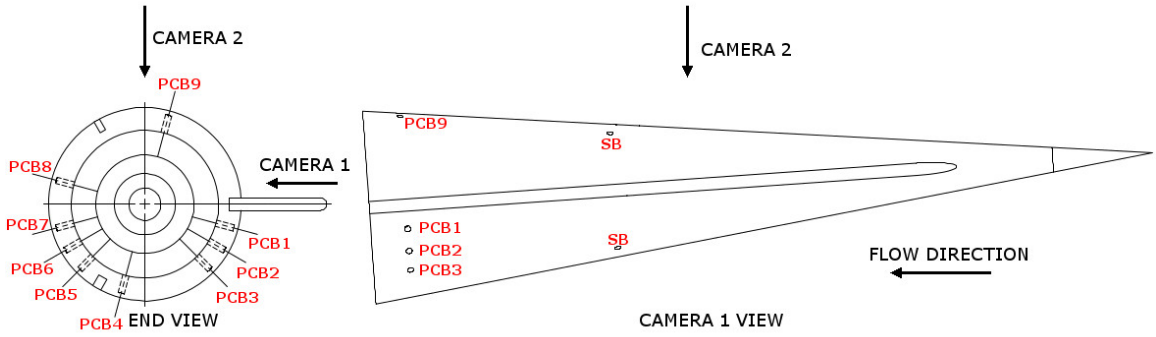

Figure 3.15. The camera and model set up for 4° angle of attack with the fin on the yawside.

4. RESULTS AND DISCUSSION

4.1 General Flow Characteristics

A TSP image is shown in Figure 4.1 at the original maximum quiet unit Reynolds number of 12.4 x 10^6 m^{-1}. This image shows the common flow features seen in the experiments on the fin-cone geometry. There are three major features labeled: streaks on the cone (A), streaks on the fin (B), and heating at the fin leading edge (C). All runs were performed under quiet flow at 0.0° angle of attack unless otherwise specified.

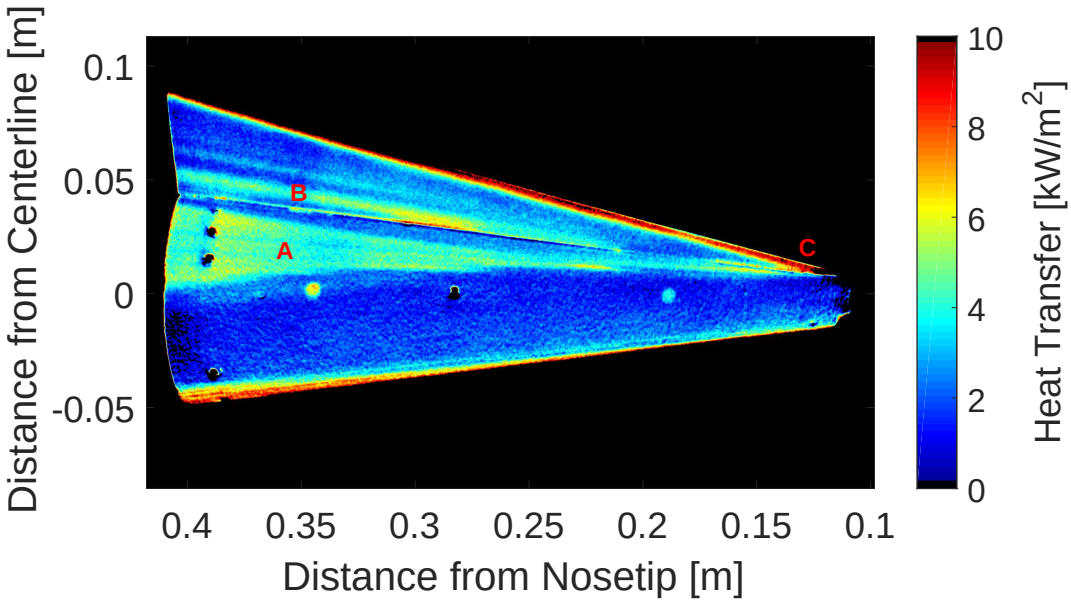

Figure 4.1. Typical TSP image of the fin-cone flowfield (Run 109, unit Re = 12.4 x 10^6 m^{-1}). Three-fin model shown with R_{LE}=1/8", 75° fin sweep, and a sharp nosetip. Flow is from right to left.

On the cone surface, multiple streaks of increased heat transfer are measured. These begin near the intersection of the fin leading edge and the cone surface. The streaks indicate a vortex system on the cone surface. This image represents the highest Reynolds number case, in which the streaks have spread extensively toward the aft end. As many as three definitive streaks have been seen in these experiments as well as the possible beginning of a fourth streak. The primary streak lies closest to the corner and extends from the fin root to the aft end of the cone. Secondary and tertiary streaks form farther outboard and downstream of the primary streak. These additional streaks could indicate secondary separations adjacent to the primary separation.

On the fin surface, one large streak appears close to the corner and smaller streaks appear farther outboard. The streak closest to the corner is much broader and has the highest heat transfer. It is assumed to be due to a vortex, similar to the streaks on the cone. The smaller streaks could also be secondary separations or due to another instability.

The most intense heating occurs at the leading edge of the fin. In all cases the heating there was several times larger than any other heating features. Increased heat transfer at the fin leading edge is expected due to the bow shock from the blunt fin.

4.2 Quiet vs. Noisy Flow

The single-fin model was primarily used to distinguish differences between noisy and quiet flow measurements. Figures 4.2 and 4.3 show the temperature change for quiet and noisy flow conditions at the same Reynolds number of 8.69 x 10^6 m^{-1}. The streaks in the noisy flow case are coincident with the SB sensor, preventing an accurate calibration of the TSP. Instead of heat transfer, a comparison of temperature change between quiet and noisy flow is provided. Note the difference in the color bar scale on the right side of the figures. In the quiet flow TSP image, Figure 4.2, the flow structure is easily distinguishable. In noisy flow, Figure 4.3, all flow structures visible under quiet flow are no longer observed. The heating on the cone surface is much higher than under quiet flow and extends well past the corner interaction region. Similarly, the heating on the fin is much higher and the streaks are indistinguishable, if they exist at all. There is a high heating region on the bottom side of the cone near the aft end in Figure 4.3. This is believed to be due to a wave from the Senflex hot film array on the nozzle wall, which has been on some larger models [39]. All subsequent runs were performed with quiet flow.

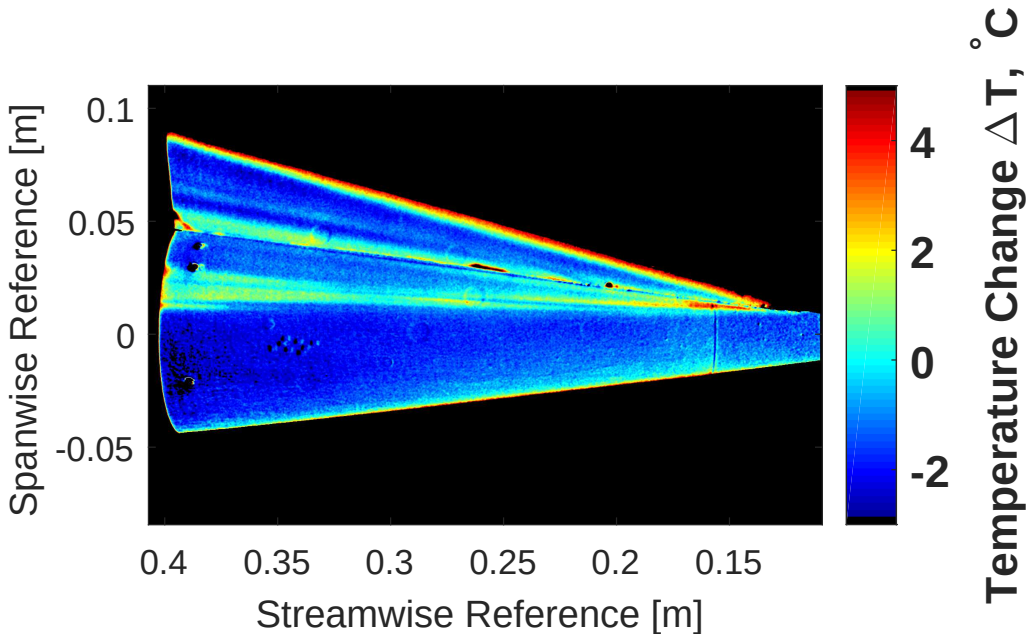

Figure 4.2. Quiet flow at Re = 8.69 x 10^6 m^{-1} (Run 028). Single-fin model shown with R_{LE}=0.175", 75° fin sweep, and a sharp nosetip.

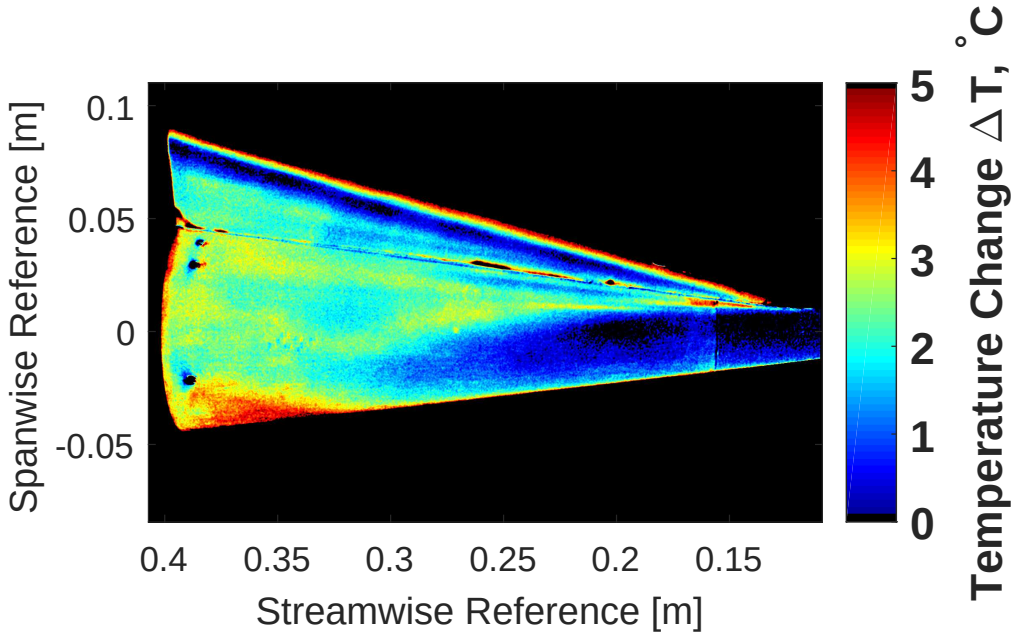

Figure 4.3. Noisy flow at Re = 8.69 x 10^6 m^{-1} (Run 032). Single-fin model shown with R_{LE}=0.175", 75° fin sweep, and a sharp nosetip.

4.3 Effect of Reynolds Number

4.3.1 TSP Data Over a Small Range of Reynolds Numbers

The Reynolds number in the BAM6QT is increased by raising the initial stagnation pressure of the driver section. Throughout the run, the Reynolds number drops periodically with the stagnation pressure as the expansion wave reflects back and forth within the driver tube. Therefore, unit Reynolds numbers between roughly 5.0 x 10^6 m^{-1} and 12.0 x 10^6 m^{-1} can be tested for each configuration in just a few runs. Figure 4.4 shows TSP images of the three-fin model as the unit Reynolds number is increased and the streaks spread over the pressure sensors at the aft end. At the lowest Reynolds number, as shown in Figure 4.4a, two thin streaks can be seen on the cone surface. These streaks fall between the PCBs at 30° and 45° from the fin centerline. As the unit Reynolds number increases in the subsequent images, Figures 4.4b - 4.4d, the streaks spread at the aft end and the location where spreading starts also moves upstream.

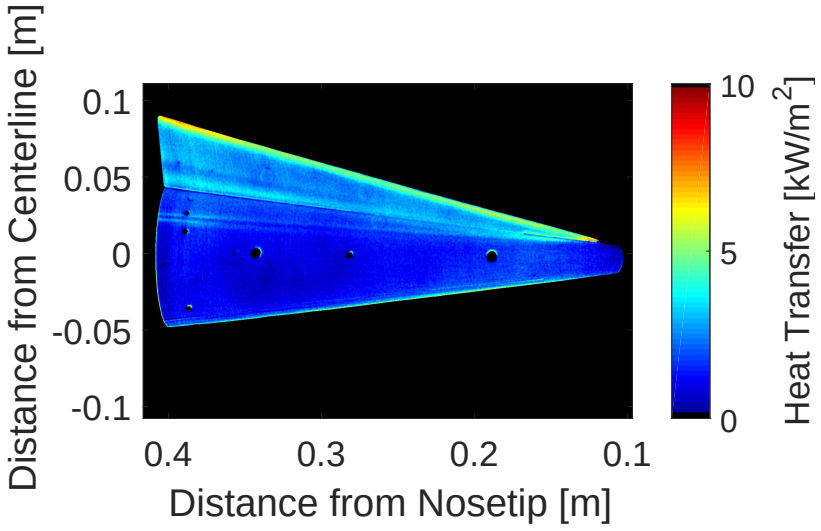

(a) Run 706, unit Re = 6.02 x 10^6 m^{-1}

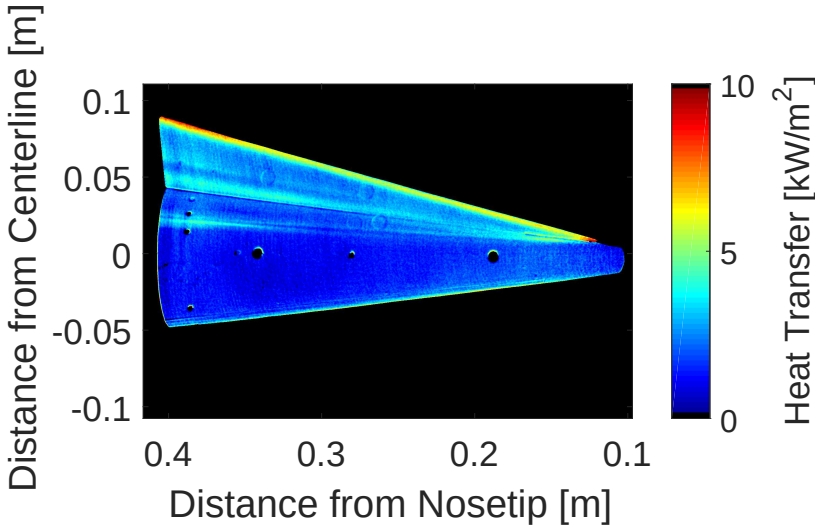

(b) Run 705, unit Re = 6.80 x 10^6 m^{-1}

Figure 4.4. Cone streaks spread as the Reynolds number increases from 6.02 x 10^6 m^{-1} to 8.12 x 10^6 m^{-1} in quiet flow. Three-fin model shown with R_{LE}=1/8", 75° fin sweep, and a sharp nosetip.

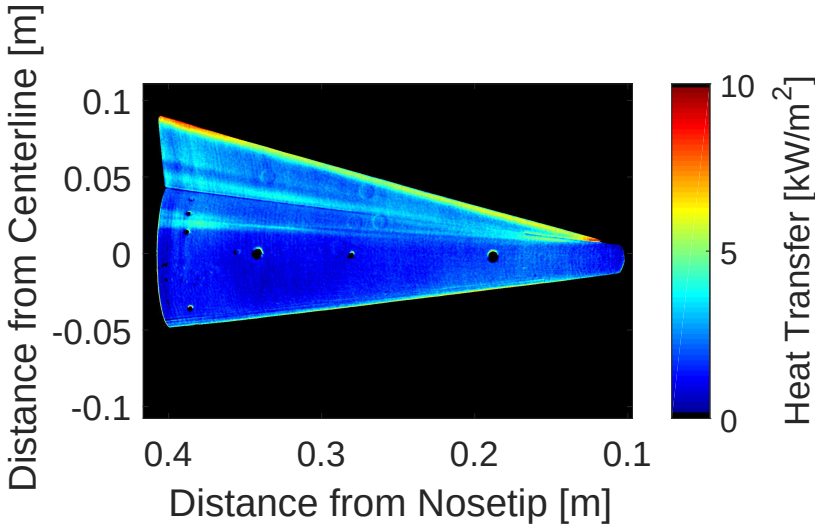

(c) Run 707, unit Re = 7.49 x 10^6 m^{-1}

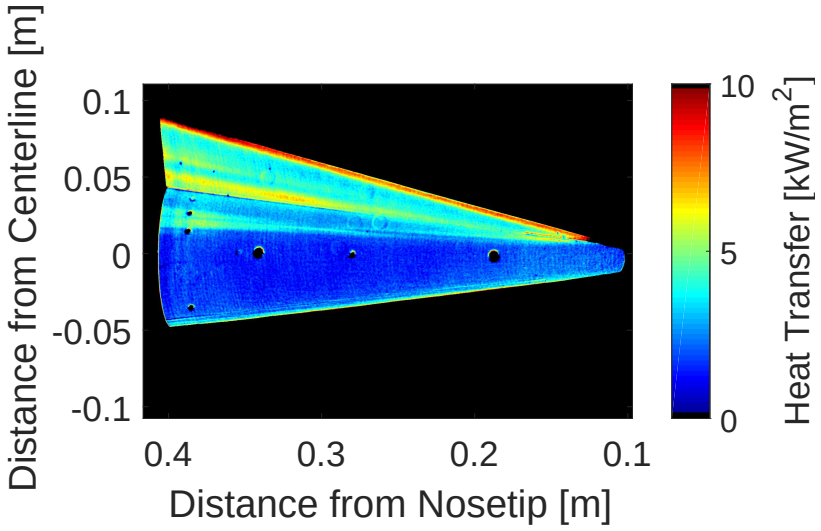

(d) Run 703, unit Re = 8.12 x 10^6 m^{-1}

Figure 4.4. (cont'd) Cone streaks spread as the Reynolds number increases from 6.02 x 10^6 m^{-1} to 8.12 x 10^6 m^{-1} in quiet flow. Three-fin model shown with R_{LE}=1/8", 75° fin sweep, and a sharp nosetip.

Figure 4.5 shows an azimuthal slice of the TSP in these images at an axial station just upstream of the sensors, x = 0.375 meters. The slices run azimuthally on the cone surface and vertically up the face of the fin. The azimuth and fin height are oriented from the corner. A moving average over a 0.5 millimeter azimuthal length was used to smooth the data. At the lowest unit Reynolds number, 6.02 x 10^6 m^{-1}, the primary and secondary streaks are clearly shown on the cone surface. As the Reynolds number increases, the two streaks on the cone spread azimuthally and the heat transfer increases. For the higher unit Reynolds number cases, the streaks are not as clearly defined. The streaks on the fin, also shown in Figure 4.5, do not broaden significantly with Reynolds number nor do they change their location on the fin.

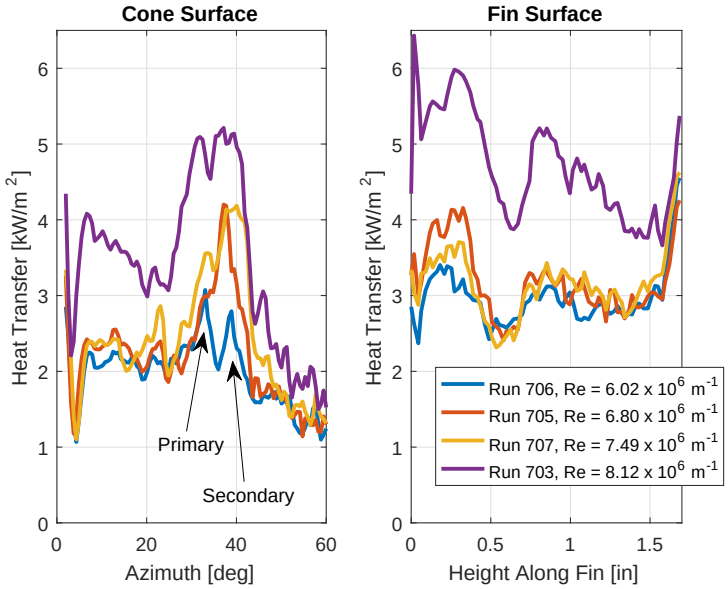

Figure 4.5. Slices of TSP images at x = 0.375 meters for Runs 703, 705, 706, and 707. The streaks spread on the cone surface and the heat transfer increases as Reynolds number increases.

4.3.2 Trouble Inferring Heat Transfer on the Fin and TSP Limitations

Two primary problems were encountered when measuring heat transfer with TSP on this model. First, the temperature of the fin was not constant throughout the run due to its thickness. This prevents an accurate TSP calibration and can also affect the heat transfer measurement on the cone, as will be discussed. Second, the resolution of the TSP is not fine enough in the present images to clearly define the streaks on the cone surface.

The fin is thin compared to the cone and the constant model temperature assumption does not hold when reducing heat transfer from temperature change. This led to inconsistency in the heat transfer measured between repeated runs. Figure 4.6 shows two TSP images of the same fin-cone geometry at similar unit Reynolds numbers under quiet flow. Figure 4.6a shows much higher heat transfer on the fin and on the cone surface near the corner than is seen in Figure 4.6b. Figure 4.7 shows the power spectral density calculated of the pressure fluctuations at the sensor closest to the corner, within the area of increased heating on the cone surface. There is no change in the power spectra, which indicates that the increase in heating is not due to transition. It was found that increasing the amount of time between runs resulted in this phenomenon being less common. The image in Figure 4.6a was taken soon after another run, which was performed at a high unit Reynolds number. The image in Figure 4.6b was taken after significant time had passed since the previous run. It is believed that when runs were made in quick succession, the fin was not able to radiate the heat gained from the previous runs. This caused the fin to sink heat into the cone during the run causing the increase in heating both on the fin and in the corner on the cone surface. This heating phenomenon occurred during several runs, such as Run 703 in Figures 4.4 and 4.5, and happened often when several runs were made in quick succession or a run was made quickly after a high Reynolds number run. It is not believed to have any effect on the flow field as evidenced by the pressure fluctuation power spectra.

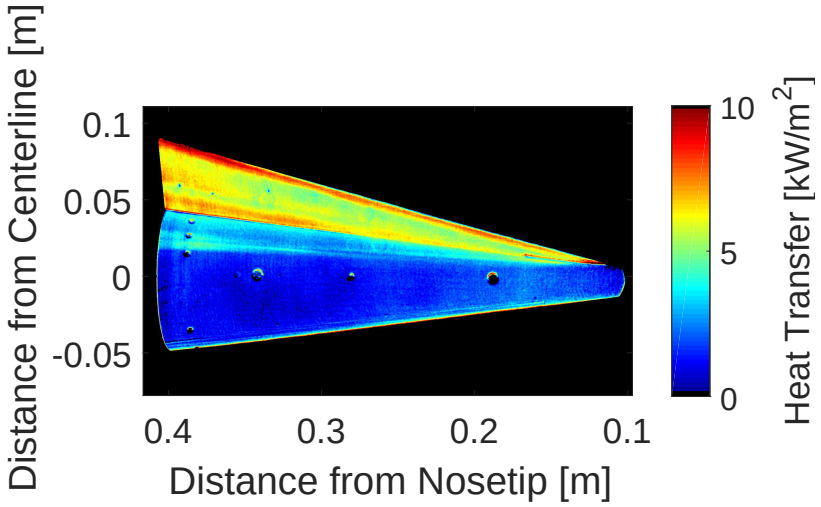

(a) Run 704, unit Re = 7.42 x 10^6 m^{-1}

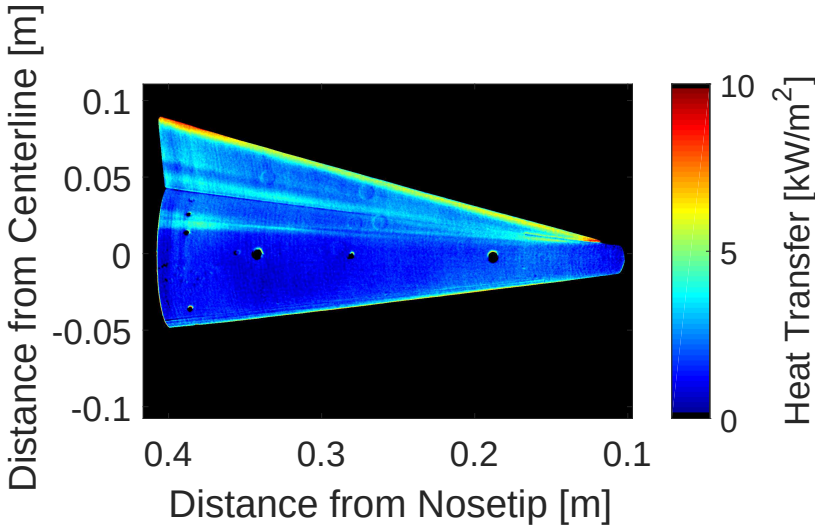

(b) Run 707, unit Re = 7.49 x 10^6 m^{-1}

Figure 4.6. Identical runs show different heat transfer on the fin and close to the corner. Three-fin model shown under quiet flow with R_{LE}=1/8", 75° fin sweep, and a sharp nosetip.

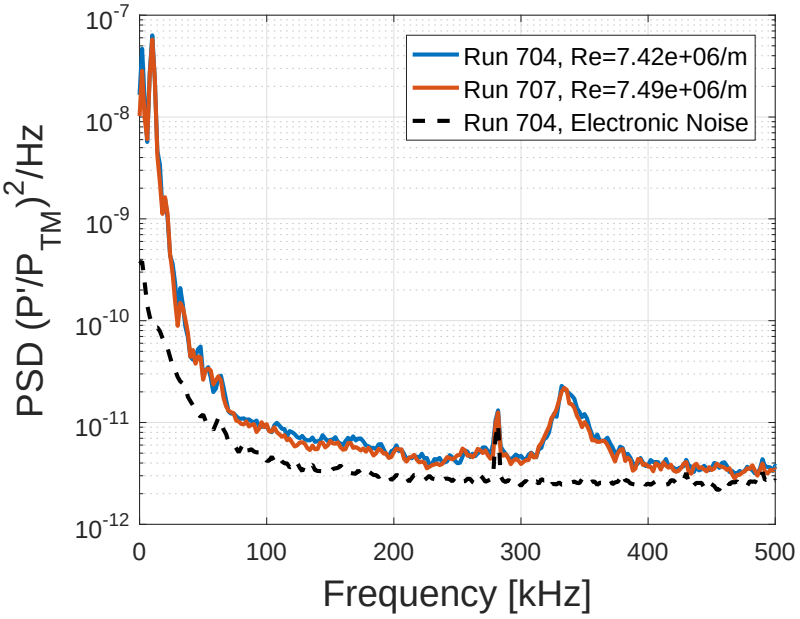

Figure 4.7. Power spectral density of the pressure fluctuations show that the heating in the corner is not due to transition.

The resolution of the TSP is critical when examining the number of streaks on the cone surface and how much these streaks have spread. The ability of the TSP method to resolve the streaks is limited by the resolution of the image as well as the signal-to-noise ratio of the TSP. Figure 4.8 shows two detail images of the streaks on the cone surface at unit Reynolds numbers of 6.02 x 10^6 m^{-1} and 7.49 x 10^6 m^{-1}. Before the streaks have spread, as in Figure 4.8a, the space between the primary streak and the secondary streak is roughly 10 pixels wide, corresponding to 2 millimeters in arc length. As the streaks spread, the space between streaks becomes even smaller, less than 1 millimeter. In future tests, better resolution must be obtained either by reducing the imaging area or by considering other heat transfer techniques such as IR that have a better signal-to-noise ratio and increased sensitivity. Improved image processing techniques need to be developed to better characterize the streaks in the current data set.

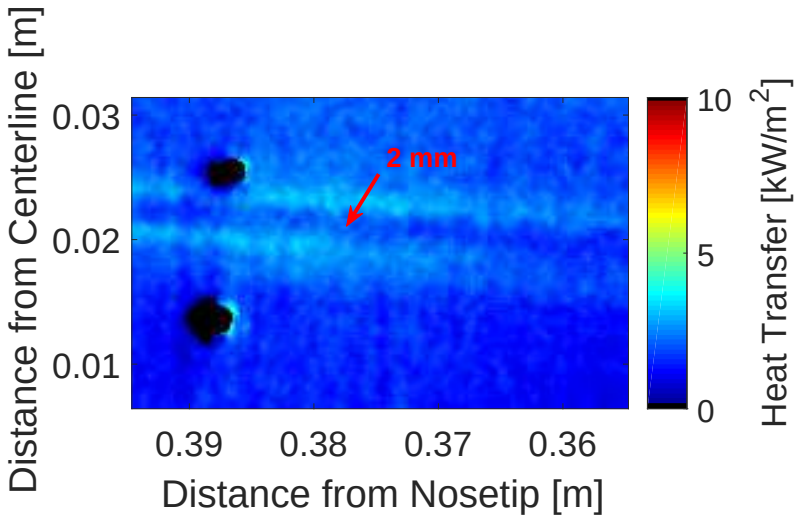

(a) Run 706, unit Re = 6.02 x 10^6 m^{-1}

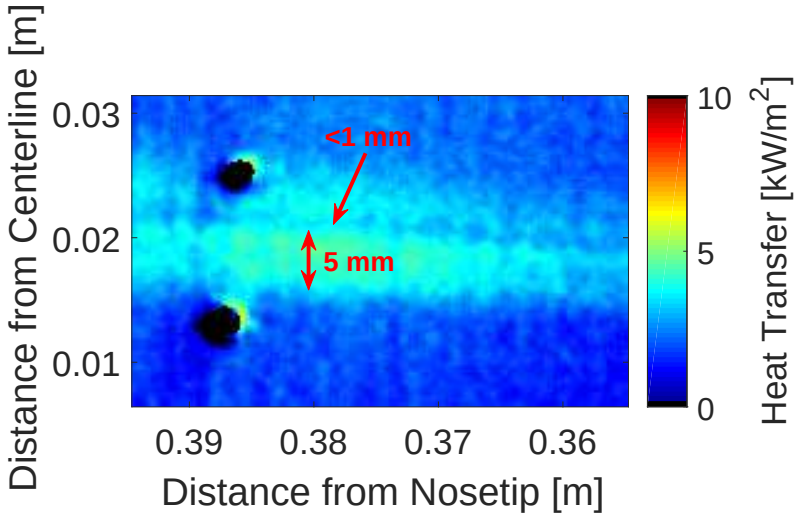

(b) Run 707, unit Re = 7.49 x 10^6 m^{-1}

Figure 4.8. Streak spreading reduces space between the streaks. TSP resolution limits the ability to define the edges of the streaks. Three-fin model shown with R_{LE}=1/8", 75° fin sweep, and a sharp nosetip.

4.3.3 Pressure Fluctuation Data as the Streaks Spread Over the Sensors

Boundary-layer instabilities were measured with the flush-mounted PCBs near the aft end of the cone. Power spectra were calculated for each of the pressure sensors in the corner region as the streaks spread. PCB1 is located closest to the corner at 15° from the fin. PCB2 is located between the corner and the streaks at 30° from the fin. PCB3 is located on the far side of the cone streaks from the corner at 45° from the fin. The spectra were computed for a range of Reynolds number at each location.

Figure 4.9 shows the power spectral density plot calculated from the pressure fluctuations for PCB1 near the corner. A peak in the power spectra is seen near 350 kHz which does not change over the Reynolds number range shown. It is unclear whether this is related to the flow, or due to some other effect such as sensor resonance. A small swell in amplitude is seen between 100 and 200 kHz. The RMS pressure fluctuations were calculated by integrating the power spectra between 30 and 800 kHz. Table 4.1 lists the RMS pressure fluctuations as a percentage of the Taylor-Maccoll pressure for each unit Reynolds number shown in Figure 4.9. The RMS pressure fluctuations decrease as the unit Reynolds number goes down, however, all three values are at a laminar level.

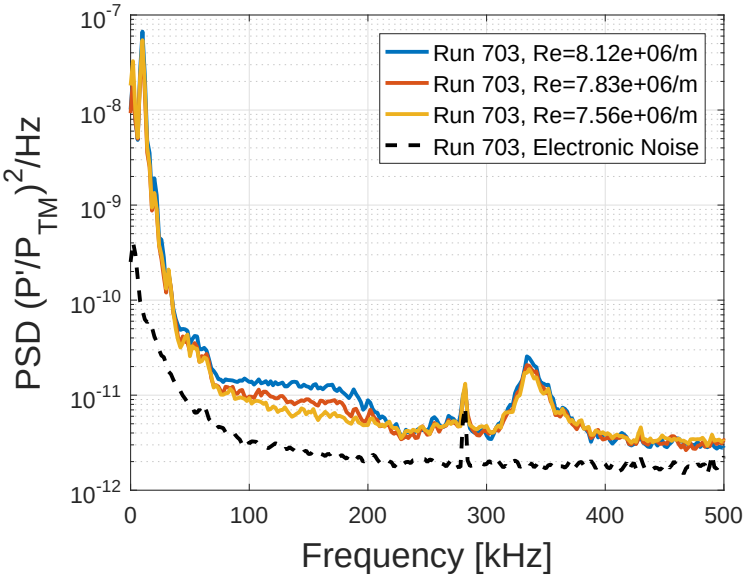

Figure 4.9. PSD of sensor 15° from fin (PCB1) at increasing unit Reynolds number. This sensor location is closest to the fin.

Table 4.1. Percent RMS pressure fluctuations for PCB1.

Unit Re [m^{-1}]	$\frac{P'_{RMS}}{P_TM}$
8.12 x 10^6	0.26%
7.83 x 10^6	0.24%
7.56 x 10^6	0.24%

Figure 4.10 shows the PSD calculated from pressure fluctuations for the sensor at 30° from the fin. As the streaks spread over the sensor with increasing unit Reynolds number, a broadband increase in the amplitude of the pressure fluctuations indicates boundary-layer transition. A high frequency peak centered near 250 kHz is measured. An additional region of increased amplitude is measured between 50 and 100 kHz. The RMS pressure fluctuations are shown in Table 4.2. The pressure fluctuations increase by an order of magnitude from a unit Reynolds number of 5.81 x 10^6 m^{-1} to 7.49 x 10^6 m^{-1}, indicating transition to turbulence.

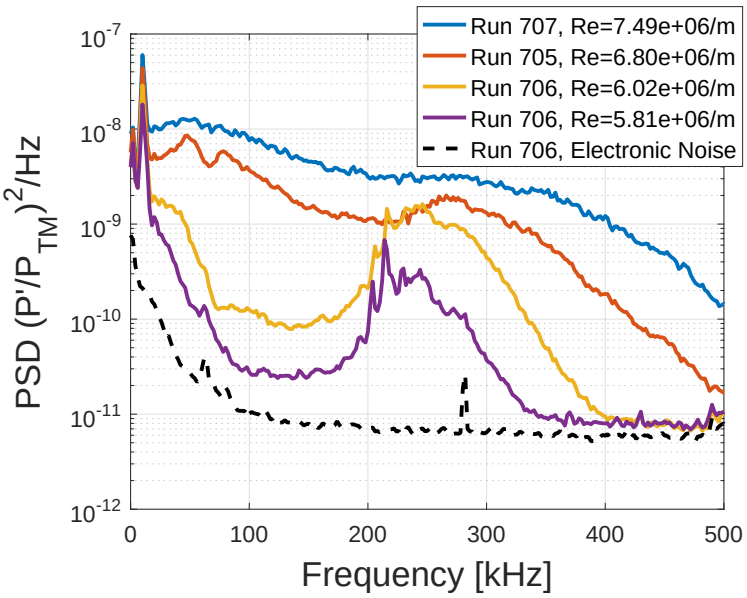

Figure 4.10. PSD of sensor 30° from fin (PCB2) at increasing unit Reynolds number. This sensor location is between the streaks and the fin.

Table 4.2. Percent RMS pressure fluctuations for PCB2.

Unit Re [m^{-1}]	$\frac{P'_{RMS}}{P_TM}$
7.49 x 10^6	4.25%
6.80 x 10^6	2.81%
6.02 x 10^6	1.26%
5.81 x 10^6	0.61%

Figure 4.11 shows the PSD calculated from the pressure fluctuations for the sensor 45° from the fin. A broadband increase in the amplitude of the pressure fluctuations is also seen for this sensor as the Reynolds number increases, however, this occurs at a slightly higher Reynolds number than for PCB2. This is due to the streaks being closer to the sensor at 30°, which requires the streaks to spread more to reach the sensor at 45°. A peak centered around 180 kHz is measured as well as another near

50 kHz. When the flow over the 45° sensor is completely laminar, such as for Re = 6.02 x 10^6 m^{-1} in Figure 4.11, the high frequency peak is still present indicating that it is not completely related to the streaks on the cone. The low frequency peak begins to appear as the streaks spread over the sensor then disappears as the flow becomes fully turbulent. This could indicate a low frequency instability related to the vortex system. The RMS pressure fluctuations are shown in Table 4.3. The pressure fluctuations increase by an order of magnitude from a unit Reynolds number of 6.02 x 10^6 m^{-1} to 8.12 x 10^6 m^{-1}, indicating transition to turbulence.

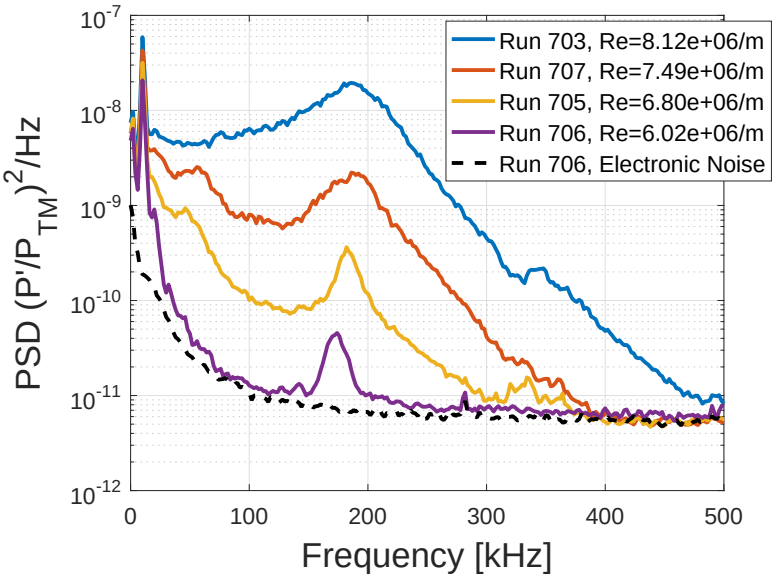

Figure 4.11. PSD of sensor 45° from fin (PCB3) at increasing unit Reynolds number. This sensor location is on the far side of the streaks from the corner.

Table 4.3. Percent RMS pressure fluctuations for PCB3.

Unit Re [m^{-1}]	$\frac{P'_{RMS}}{P_T M}$
8.12 x 10^6	4.43%
7.49 x 10^6	1.67%
6.80 x 10^6	0.72%
6.02 x 10^6	0.29%

The peak in the PSD near 250 kHz for the sensor located 30° from the fin and the peak near 180 kHz for the sensor located 45° from the fin are in the frequency range of the second-mode instability for a 7° straight cone. Figure 4.12 shows a second-mode frequency measured on the fin-cone geometry with the fins removed. The second-mode frequency measured is near 220 kHz at a unit Reynolds number of 9.48 x 10^6 m^{-1}. In order to predict the second-mode frequency for any unit Reynolds number, a Navier-Stokes solver, Stability and Transition Analysis for hypersonic Boundary Layers (STABL), was used to obtain a mean flow for a 7° straight cone. STABL can estimate the second-mode frequency by integrating the time that it takes for a wave to travel from the surface to the relative Mach line in the boundary layer. This has been shown to estimate the experimental second-mode frequency within 2% [40]. Figure 4.13 shows the second-mode frequencies estimated by STABL for a range of unit Reynolds numbers. The second-mode frequency scales linearly with the square root of the unit Reynolds number. The estimated second-mode frequency agrees well with the high frequency peak measured by the sensor at 45° from the fin. This seems to confirm that this peak is due to the second-mode instability. The frequency measured at the sensor 30° away from the fin is much higher than the second-mode frequency estimated by STABL. This might imply that the boundary layer is thinner between the streaks and the fin.

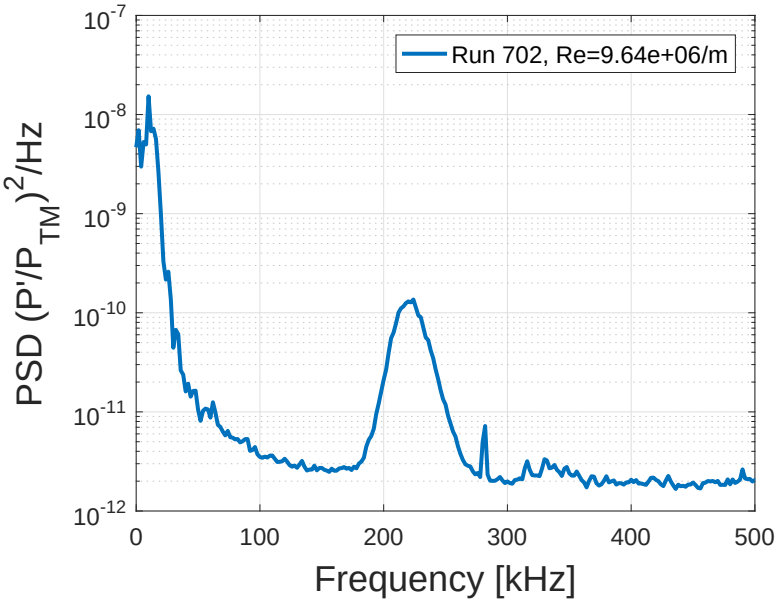

Figure 4.12. PSD of a PCB sensor on the three-fin model with no fins installed and a sharp nosetip. Second-mode instability measured at Re = 9.48 x 10^6 m^{-1}.

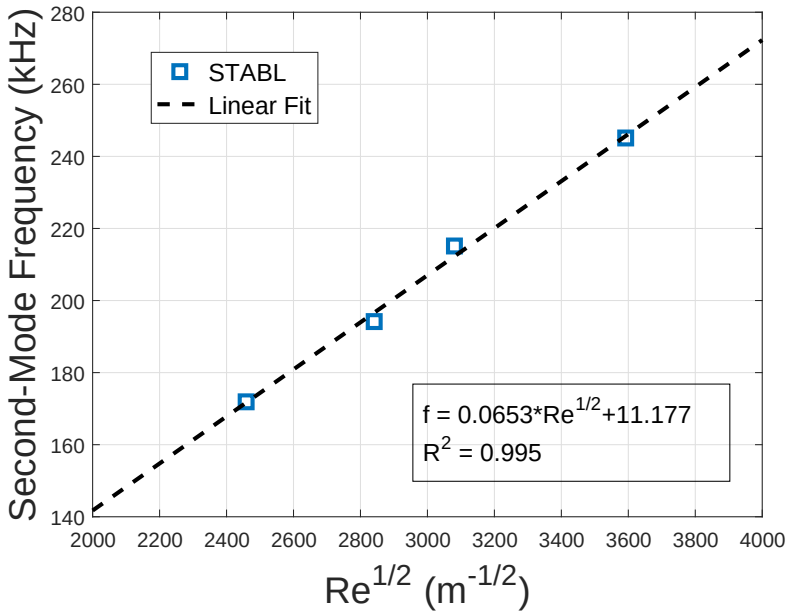

Figure 4.13. The second-mode frequency estimated using STABL increases linearly with the square root of unit Reynolds number.

4.3.4 TSP Data at Higher Reynolds Number

When the Reynolds number is increased to near the maximum quiet unit Reynolds number (12.4 x 10^6 m^{-1}), more streaks begin to appear. Figure 4.14 shows a TSP image at the original maximum quiet Reynolds number for the three-fin model with a 75° fin sweep, a 1/8-inch leading edge radius, and a sharp nosetip. An azimuthal slice of the TSP in Figure 4.15 shows three individual peaks of high heat transfer on the cone surface between 20° and 55°, indicated by black arrows. A fourth large peak very close to the corner near 3° is due to an anomaly in the paint. A slice of heat transfer for a lower Reynolds number case (6.02 x 10^6 m^{-1}) is also included in Figure 4.15. A double-sided arrow shows a shift in the streak location between the two cases. It is unclear whether this is a real movement or due to uncertainty in determining the azimuth in the TSP slicing method. The fin streaks appear to be in the same location, but the heat transfer magnitude is uncertain. The RMS pressure fluctuations given in Table 4.4 show that the flow is turbulent at all sensor locations.

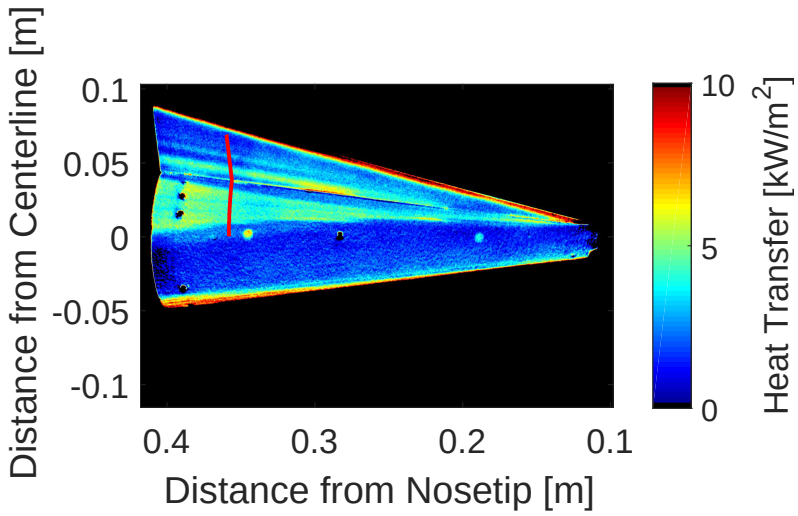

Figure 4.14. Three heating streaks and extensive streak spreading are seen at higher Reynolds number. (Run 109, unit Re = 12.4 x 10^6 m^{-1}). Three-fin model shown with R_{LE}=1/8", 75° sweep, and a sharp nosetip.

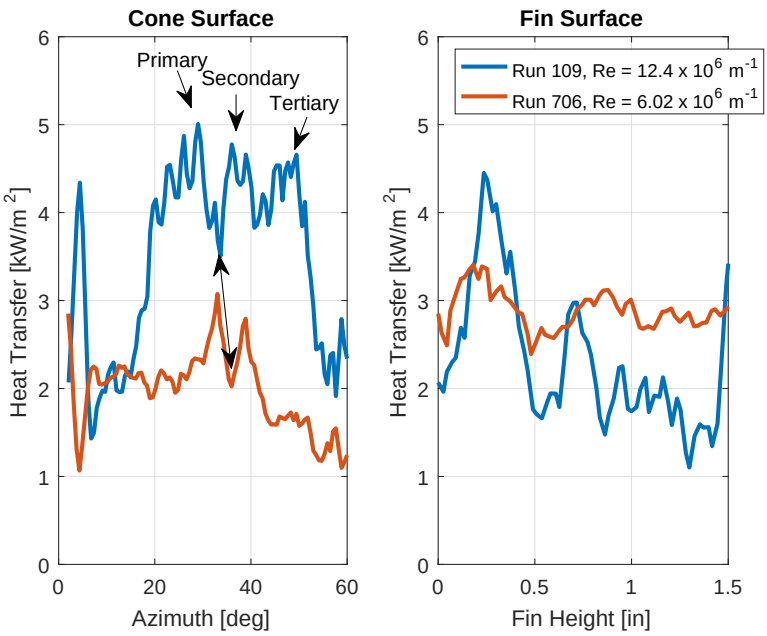

Figure 4.15. At maximum quiet Reynolds number there are three streaks on the cone surface. Slice of TSP image for Run 109 at x = 0.356 meters. Data from Run 706 overlaid to show that the two streaks on the cone surface indicated by the arrows have the same location.

Table 4.4. Percent RMS pressure fluctuations for all sensors in the corner region at a unit Reynolds number of 12.4 x 10^6 m^{-1}.

Sensor	Location from Fin	$\frac{P'_{RMS}}{P_{TM}}$
PCB1	15°	4.42%
PCB2	30°	5.03%
PCB3	45°	5.54%

4.4 Effect of Nose Bluntness

4.4.1 TSP Data for Three Nosetip Radii

The effect of increasing the nose radius has been investigated on the three-fin model using interchangeable nosetips. TSP images at the aft end for three different nosetips are shown in Figure 4.16 for a fin with 75° sweep and a 1/8-inch leading edge radius at similar Reynolds numbers. The nosetip radii tested were sharp, 1 mm, and 2 mm. The larger nosetip cases show reduced spreading of the cone streaks. Figure 4.17 shows a slice of the TSP at an axial station just upstream of the sensors for the TSP images in Figure 4.16. The heat transfer in the cone streaks is significantly decreased from a sharp nosetip down to a 2 mm radius nosetip, however, the magnitudes in the corner for Runs 703 and 709 indicate that the TSP might be artificially high due the previously discussed issues with the fin. Regardless of magnitude, the streaks narrow considerably from the sharp nosetip to the 2 mm radius nosetip. The location of the cone streaks appears to move away from the corner with increasing nose radius, though this effect is too small to conclude this with any certainty.

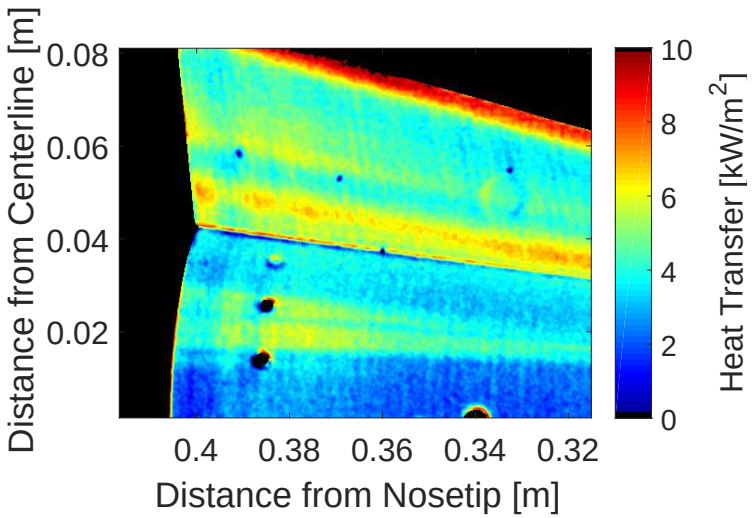

(a) Run 703, sharp nosetip, Re = 8.26 x 10^6 m^{-1}

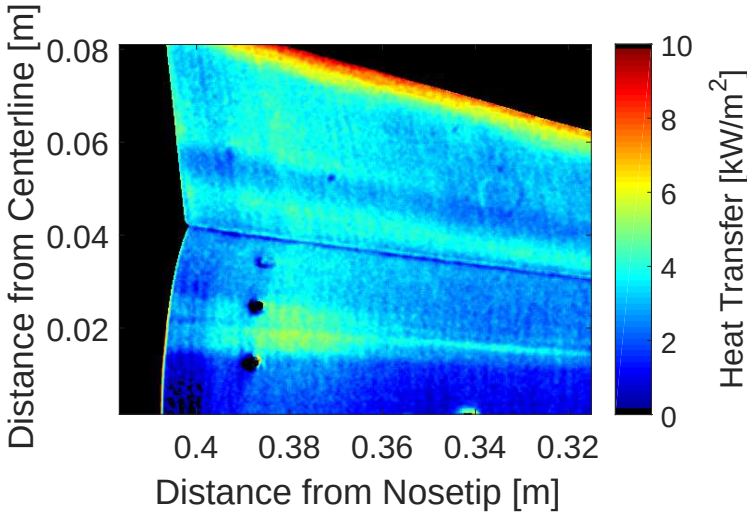

(b) Run 709, R_{NT} = 1 mm, Re = 8.29 x 10^6 m^{-1}

Figure 4.16. Increasing nosetip radius reduces streak spreading at a similar Reynolds number. Three-fin model shown with R_{LE}=1/8" and 75° sweep.

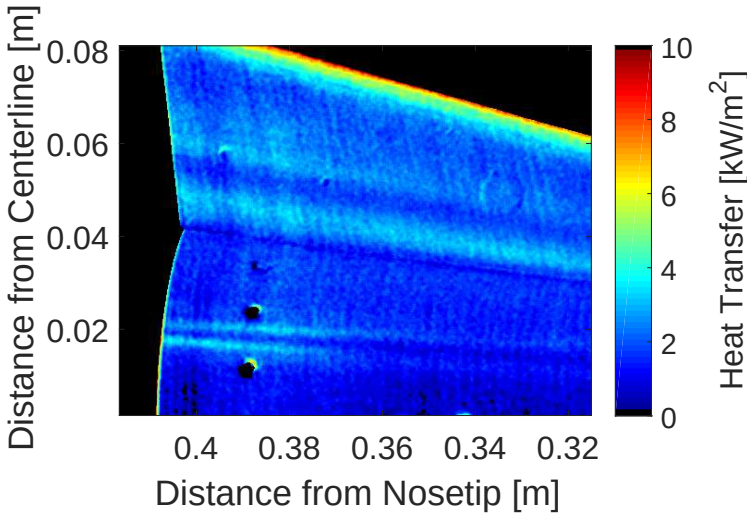

(c) Run 715, R_{NT} = 2 mm, Re = 8.30 x 10^6 m^{-1}

Figure 4.16. (cont'd) Increasing nosetip radius reduces streak spreading at a similar Reynolds number. Three-fin model shown with R_{LE}=1/8" and 75° sweep.

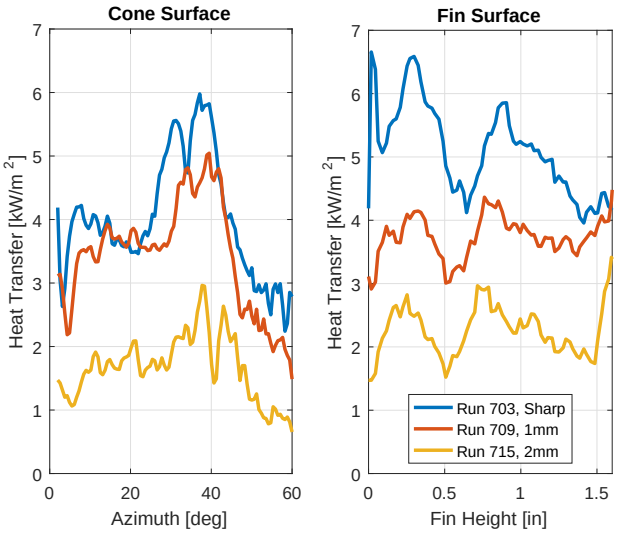

Figure 4.17. Increasing nose radius narrows the streak on the cone surface and reduces heat transfer. Slices of TSP images at x = 0.375 meters for Runs 703, 709, and 715 at similar Reynolds number. Three-fin model with R_{LE}=1/8" and 75° sweep.

Improved TSP measurements were obtained for a fin with 70° sweep and a 1/8-inch leading edge radius. The TSP images for this geometry are shown in Figure 4.18. A spanwise slice of these measurements are given in Figure 4.19. The heat transfer magnitudes are much more consistent for each nosetip. Similar to the 75° sweep case in Figure 4.17, the streaks narrow as nose radius increases. The effect is more pronounced from a nose radius of 1 mm to 2 mm than from a sharp nosetip to a 1 mm nose radius. In both Figure 4.17 and Figure 4.19 the locations of the streaks on the fin are invariant with nose radius.

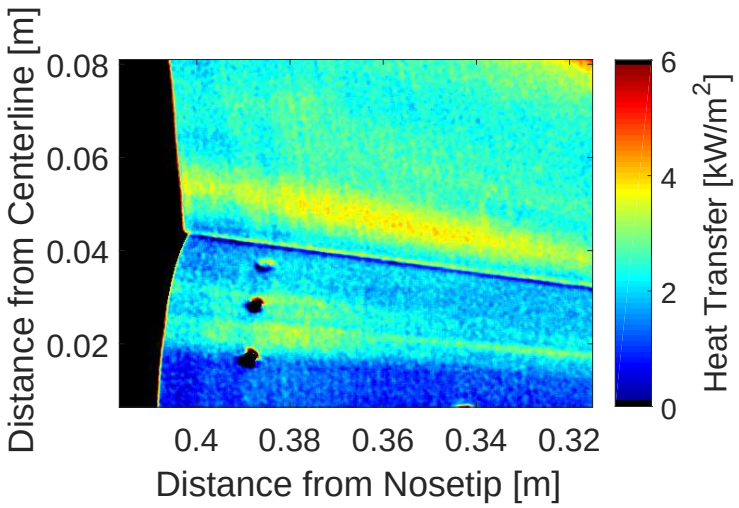

(a) Run 719, sharp nosetip, Re = 6.73 x 10^6 m^{-1}

Figure 4.18. Increasing nosetip radius reduces streak spreading at a similar Reynolds number. Three-fin model shown with R_{LE}=1/8" and 70° sweep.

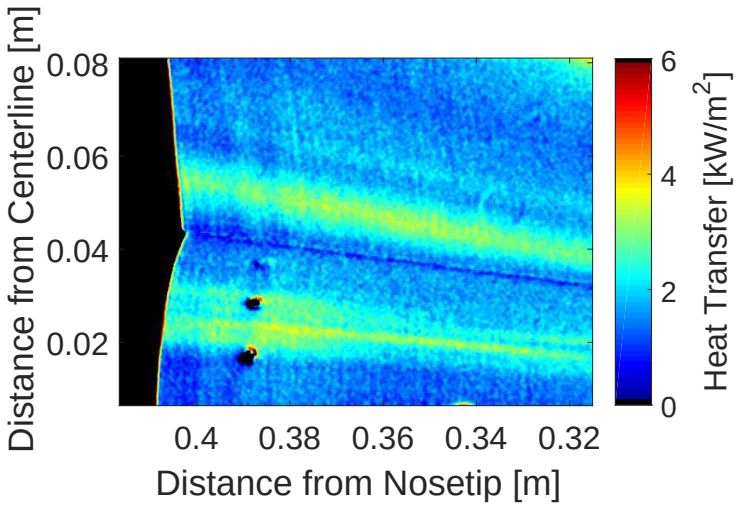

(b) Run 724, R_{NT} = 1 mm, Re = 6.75 x 10^6 m^{-1}

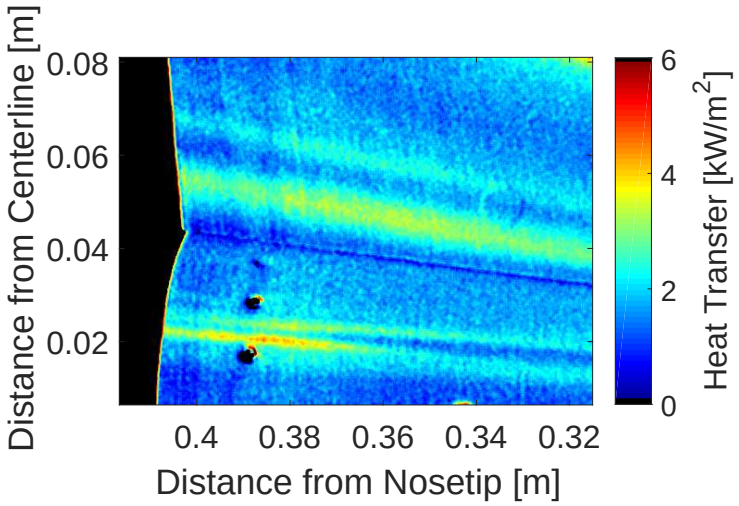

(c) Run 729, R_{NT} = 2 mm, Re = 6.74 x 10^6 m^{-1}

Figure 4.18. (cont'd) Increasing nosetip radius reduces streak spreading at a similar Reynolds number. Three-fin model shown with R_{LE}=1/8" and 70° sweep.

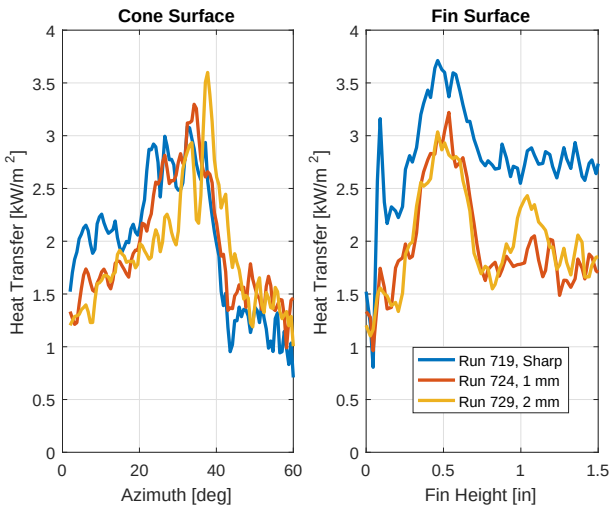

Figure 4.19. Increasing nose radius narrows the streak on the cone surface, however, there is little effect on heat transfer. Slices of TSP images at x = 0.375 meters for Runs 719, 724, and 729 at a similar unit Reynolds number. Three-fin model with R_{LE}=1/8" and 70° sweep.

4.4.2 Pressure Fluctuation Data for Three Nosetip Radii

The pressure fluctuation power spectra for the fin-cone with a 1/8-inch fin leading-edge radius and 75° sweep are given in Figure 4.20. Figure 4.20a shows the pressure fluctuations for the sensor closest to the fin. The sharp nosetip case has a swell between 100 and 200 kHz, which is not present for larger nose radii. The peak near 350 kHz is nearly the same for the sharp and 1 mm nose radius cases, however, the amplitude of the peak is reduced for the 2 mm radius nosetip. Figure 4.20b shows the pressure fluctuations for the sensor at 30° from the fin, which is very close to the fin side of the streak. The fluctuation level of the sharp and 1 mm cases are nearly identical because the streak has narrowed but is still coincident with the sensor. For the 2 mm nosetip case, the streak is no longer over the sensor face, and the fluctuation level has reduced to near fully-laminar levels. Pressure fluctuation power spectra for the sensor farthest from the corner, at 45° from the fin, are shown in Figure 4.20c. The fluctuation level here consistently drops with increasing nose radius as transition is delayed and the streak narrows. Table 4.5 lists the RMS pressure fluctuations for the three nosetips. Increasing nosetip radius reduces pressure fluctuations from turbulent to laminar levels for all sensor locations.

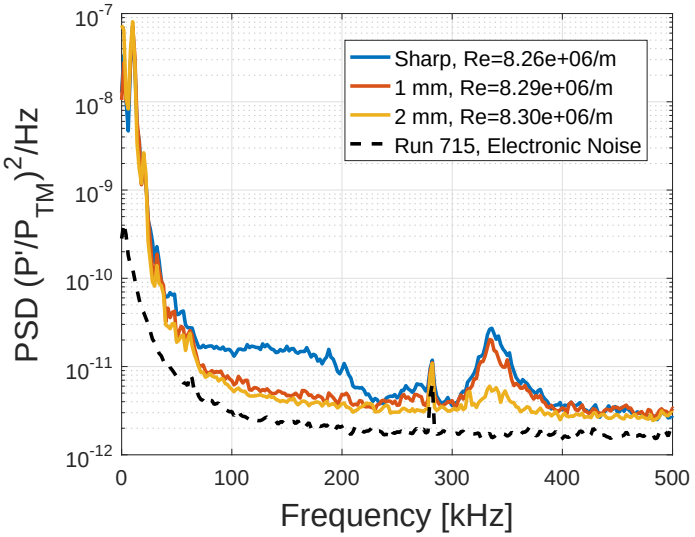

(a) Sensor 15° from fin

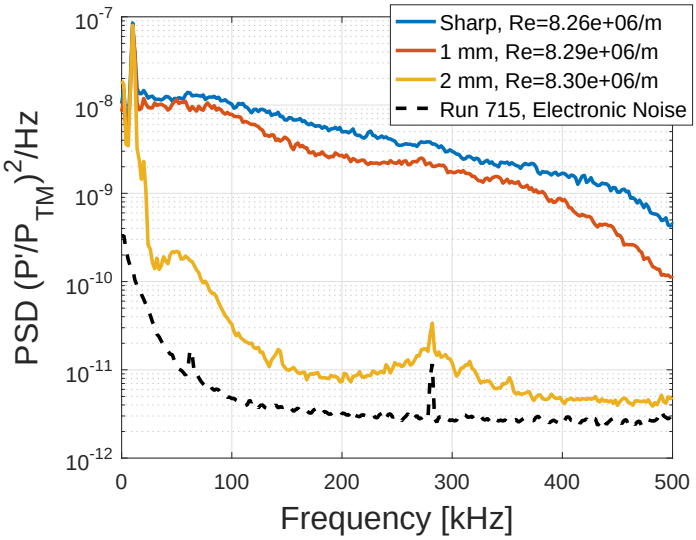

(b) Sensor 30° from fin

Figure 4.20. Increasing nosetip radius significantly decreases the broadband amplitude of the pressure fluctuations, indicating delayed transition. Measurements on three-fin model with R_{LE}=1/8" and 75° sweep.

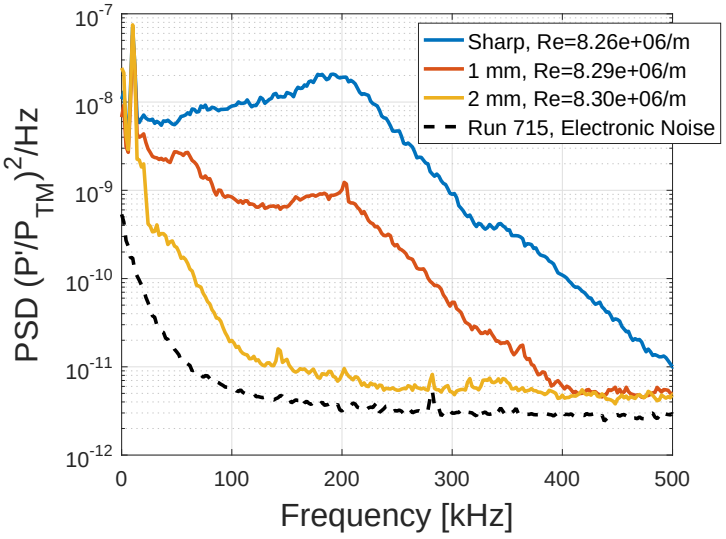

(c) Sensor 45° from fin

Figure 4.20. (cont'd) Increasing nosetip radius significantly decreases the broadband amplitude of the pressure fluctuations, indicating delayed transition. Measurements on three-fin model with R_{LE}=1/8" and 75° sweep.

Table 4.5. RMS pressure fluctuations ($\frac{P'_{RMS}}{P_{TM}}$) for three nosetip radii and 75° fin sweep.

Sensor	Sharp Nosetip	1 mm Nosetip	2 mm Nosetip
PCB1	0.28%	0.23%	0.20%
PCB2	4.84%	3.87%	0.38%
PCB3	5.11%	1.55%	0.38%

The pressure fluctuations power spectra for the fin-cone with 1/8-inch fin leading edge radius and 70° sweep are given in Figure 4.21. These spectra display the same trend as shown for the 75° fin sweep case. Table 4.6 shows decreases in RMS pressure fluctuations with increasing nosetip radius at all sensor locations.

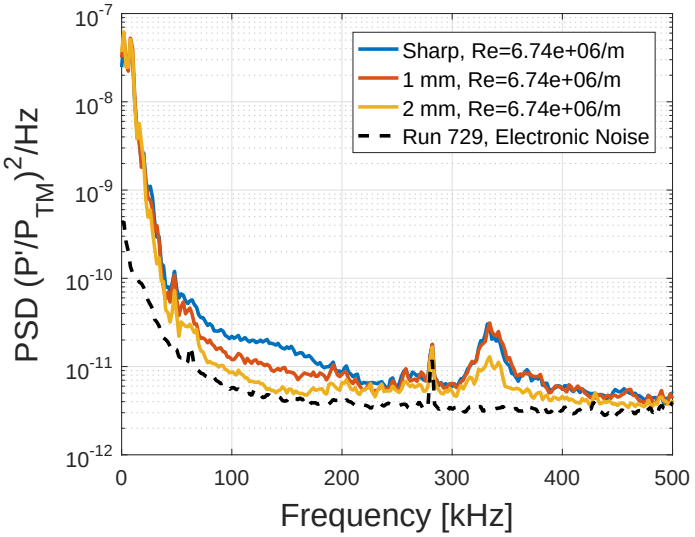

(a) Sensor 15° from fin

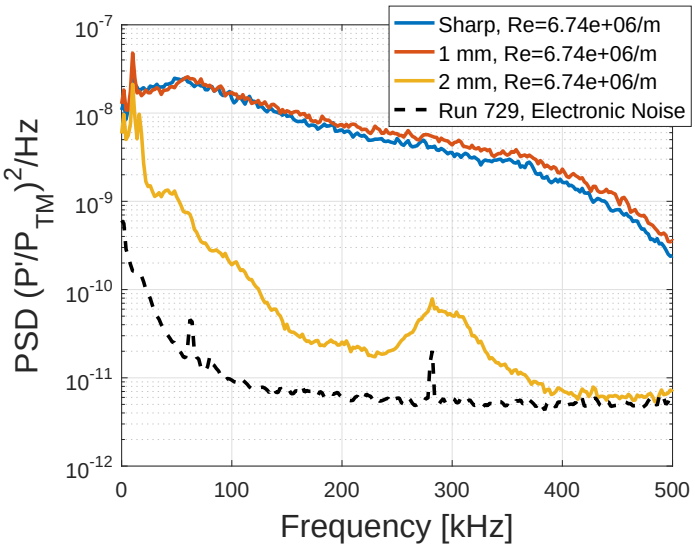

(b) Sensor 30° from fin

Figure 4.21. Increasing nosetip radius significantly decreases the broadband amplitude of the pressure fluctuations, indicating delayed transition. Measurements on three-fin model with R_{LE}=1/8" and 70° sweep.

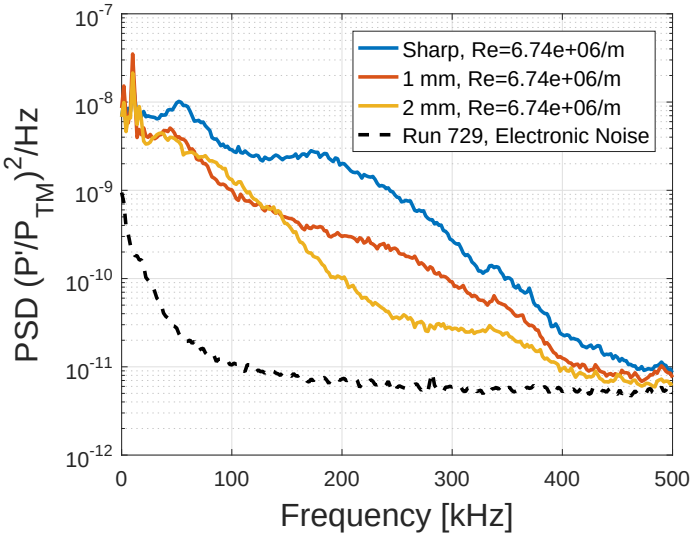

(c) Sensor 45° from fin

Figure 4.21. (cont'd) Increasing nosetip radius significantly decreases the broadband amplitude of the pressure fluctuations, indicating delayed transition. Measurements on three-fin model with R_{LE}=1/8" and 70° sweep.

Table 4.6. RMS pressure fluctuations ($\frac{P'_{RMS}}{P_{TM}}$) for three nosetip radii and 70° fin sweep.

Sensor	Sharp Nosetip	1 mm Nosetip	2 mm Nosetip
PCB1	0.33%	0.30%	0.25%
PCB2	5.71%	6.01%	0.79%
PCB3	2.83%	1.67%	1.60%

The effect of nose radius on the transition process for the 75° sweep case is shown in Figure 4.22. Power spectra are shown for the sensors on either side of the streaks, 30° and 45° from the fin, for each nosetip. A range of Reynolds numbers for each sensor is given to compare similar stages in the transition process which occur at higher Reynolds number for larger nose radii. Figures 4.22a, 4.22c, and 4.22e show the power spectra for the sensor 30° from the fin which is between the streak and the corner. The high frequency peak for the sharp case, as in Figure 4.22a, is centered around 250 kHz and has a distinct peak. For the 1 mm radius nosetip shown in Figure 4.22c, the peak is flattened and is spread over a larger range of frequencies. Figure 4.22e shows that the amplitude of this peak is greatly reduced for the 2 mm radius nosetip.

Figures 4.22b, 4.22d, and 4.22f show the power spectra for the sensor 45° from the fin, which is outside of the streak. A peak around 200 kHz is present in Figure 4.22b for the sharp nosetip case. Figures 4.22d and 4.22f show that the amplitude of this peak decreases with increasing nosetip radius. Increasing nose radius has been shown to delay transition on straight cones due to the swallowing of the entropy layer created by the nose [45, 46]. This affects amplification of the second-mode instability. Figure 4.13 suggests that the second-mode instability has a frequency of between 170 kHz and 220 kHz for the unit Reynolds number range shown in Figure 4.22. The high frequency peaks seen in Figure 4.22 are most likely second-mode waves that are suppressed by the increase in nose radius. The frequency of the second mode peak is higher inside the streak, suggesting that the vortex system has the effect of thinning the boundary layer in the corner. There is seemingly little effect of nose radius on the amplitude of the low frequency instability at about 50 kHz for either sensor location.

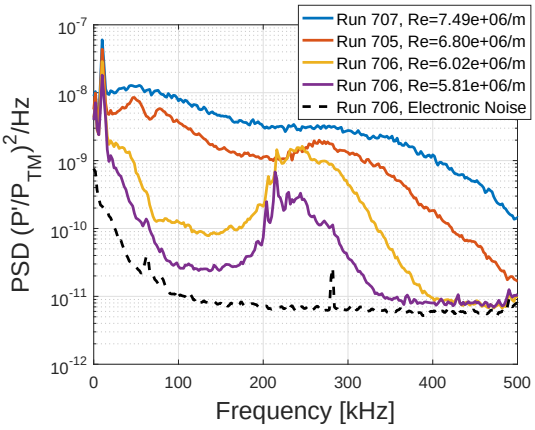

(a) sharp nosetip, 30° from fin

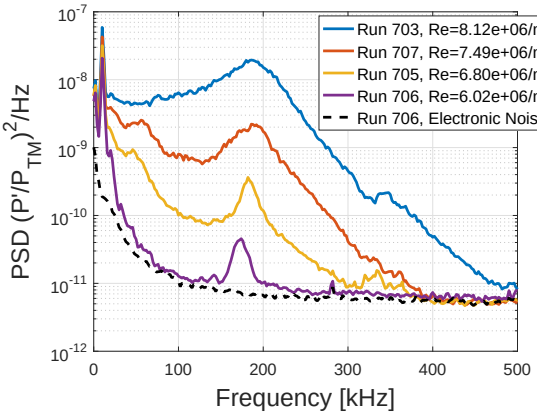

(b) sharp nosetip, 45° from fin

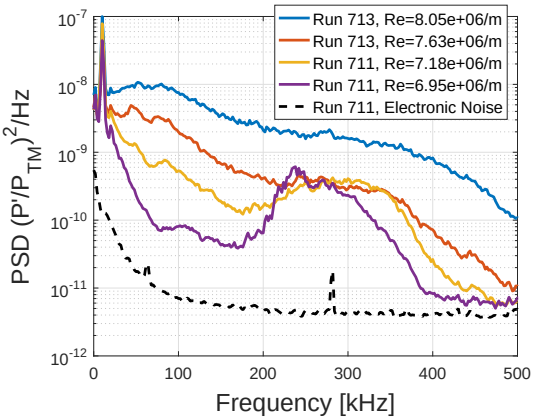

(c) R_{NT} = 1 mm, 30° from fin

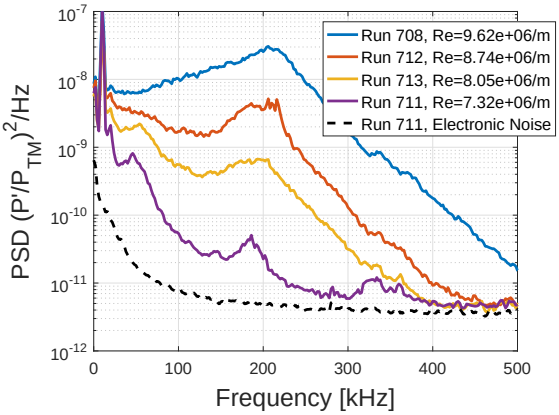

(d) R_{NT} = 1 mm, 45° from fin

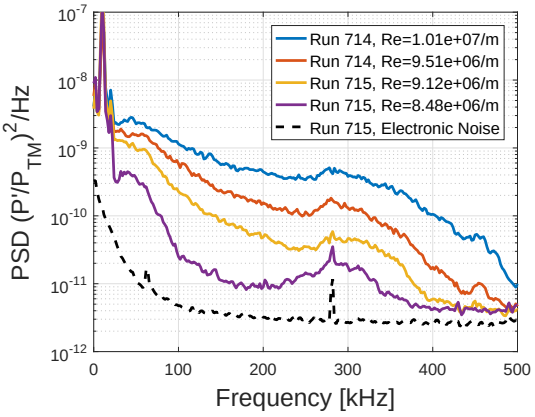

(e) R_{NT} = 2 mm, 30° from fin

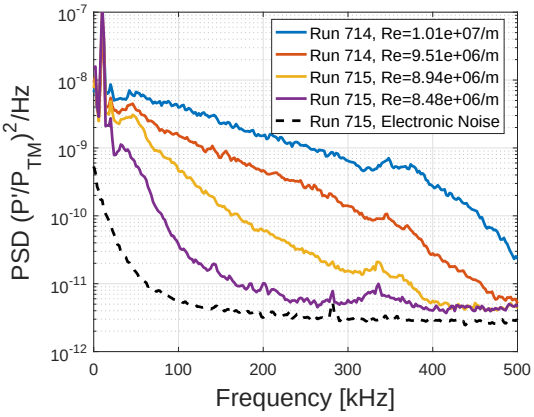

(f) R_{NT} = 2 mm, 45° from fin

Figure 4.22. Second-mode instability suppressed both inside and outside of the streak with increased nose radius. Low-frequency instability seemingly unchanged by nose radius. Three-fin model with R_{LE}=1/8" and 75° fin sweep.

4.5 Fin Sweep

4.5.1 Shock Attachment at the Fin Leading Edge

Blunt fins introduce a boundary-layer disturbance upstream of the fin due to the bow shock at the fin leading edge. The fin shock causes a pressure increase which can lead to boundary-layer separation and the classic lambda shock structure. Horseshoe vortices can form in this separation region and propagate downstream. As fins are swept back, a condition can occur where the fin shock becomes attached at the fin root preventing the formation of the lambda shock.

Stollery estimated the conditions where fin shock attachment can occur for blunt, swept fins, which are reproduced in Figure 4.23 [23]. First, the sweep must be high enough for an oblique shock wave to be attached at the fin root. This boundary is the curve in red in Figure 4.23. Envisioning the leading edge of the fin as a wedge, this can be found by solving for the maximum turn angle via isentropic oblique shock theory for a given freestream Mach number as shown in Equation 4.1, where θ is the shock angle and δ is the turn angle. The turn angle is related to the sweep angle, Λ, as given in Equation 4.2.

$$\tan\theta = \frac{(1/\tan\beta)(M^2\sin^2\beta - 1)}{\frac{\gamma+1}{2}M^2 - (M^2\sin^2\beta - 1)} \tag{4.1}$$

$$\theta = 90^\circ - \Lambda \tag{4.2}$$

The second condition, shown in blue in Figure 4.23, requires that the sweep must not be so much as to make the normal Mach number less than one, as shown in Equation 4.3.

$$M_N = M\cos\Lambda \geq 1 \tag{4.3}$$

He notes that this condition creates a supersonic leading edge that limits spanwise communication, though it is unclear what he means by this. It is likely that he intends

for this limit to be defined as in Equation 4.4, where the leading edge is coincident with the Mach angle, μ.

$$\mu = \sin^{-1}\frac{1}{M} = 90^\circ - \Lambda \tag{4.4}$$

It is uncertain how much this condition affects the attachment of the shock at the fin root. Stollery considers these constraints to be conservative estimates, so this condition may be too restrictive.

The yellow curve is the empirical two-dimensional wedge angle required for incipient separation of a turbulent boundary layer, as given in Equation 4.5.

$$\alpha_i = \Lambda - 90^\circ = 10\sqrt{(M)} \tag{4.5}$$

A second empirical curve for a laminar boundary layer, shown in purple, has been added to the plot. This correlation is provided in Equation 4.6 and was also taken from Stollery [23].

$$\alpha_i = \Lambda - 90^\circ = 3\sqrt{(M)} \tag{4.6}$$

Stollery has found that attachment is likely for fins in region A1, bounded by the blue and yellow curves, and attachment is possible in region A2, bounded by the yellow and red curves. He established these zones for a turbulent boundary layer. Using the same logic for a laminar boundary layer, attachment is likely above the purple curve, and possible between the purple and red curves. Laminar boundary layers are much more likely to separate than turbulent boundary layers, meaning that the yellow curve may be a feasible lower bound for a laminar boundary layer. Data points are plotted for the fin sweeps used in these experiments, adjusted to account for the cone angle. The shock is possibly attached for both fin sweeps, but this is uncertain. Recent simulations of the fin-cone geometry with a 1/8-inch fin leading edge radius, 70° sweep, and a 1 mm nosetip radius at unit Reynolds number of 9.68 x 10^6 m^{-1} indicate a separation bubble upstream of the fin [47]. It is possible that the streaks seen in the TSP are due to horseshoe vortices that form in this separation region and propagate downstream.

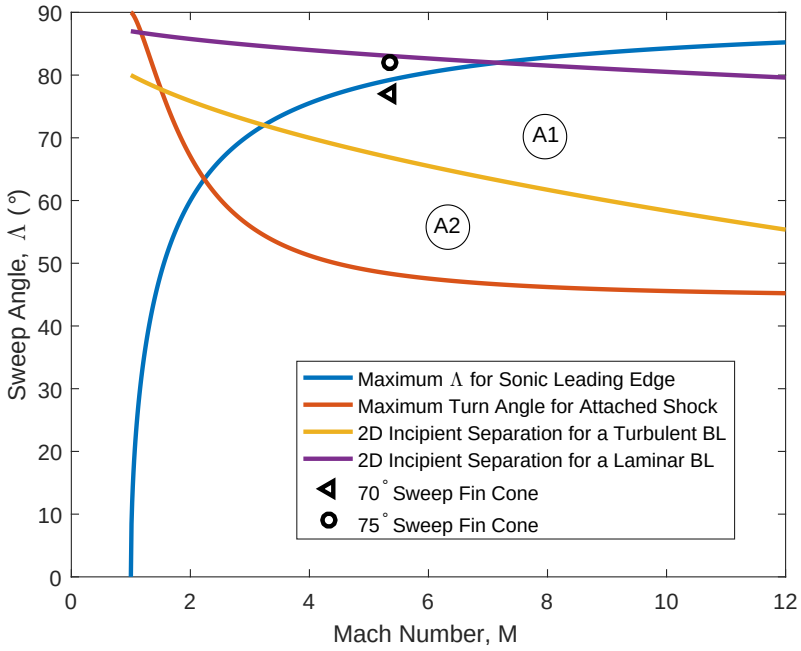

Figure 4.23. Conditions for an attached shock at the root of a blunt, swept fin reproduced from Stollery [23].

4.5.2 TSP Data for Fin Sweeps of 70° and 75°

Fin sweeps of 70° and 75° were tested. The 70° fin had to be truncated to avoid interaction with the tunnel-wall boundary layer. Figure 4.24 shows TSP images of the fin interaction region for a fin leading edge radius of 1/8 inches and a sharp nosetip. These images show that at the same Reynolds number the cone streak has spread more for the fin with less sweep. Figure 4.25 shows spanwise slices of the TSP for the two fin sweeps. The slices show the spreading of the cone streak, and also that the streaks for the 75° sweep fin are farther from the corner. The streak on the fin has moved farther from the corner for the 70° sweep case. There appears to be a slightly higher heat transfer magnitude for the case with more sweep, but this could be within TSP tolerances.

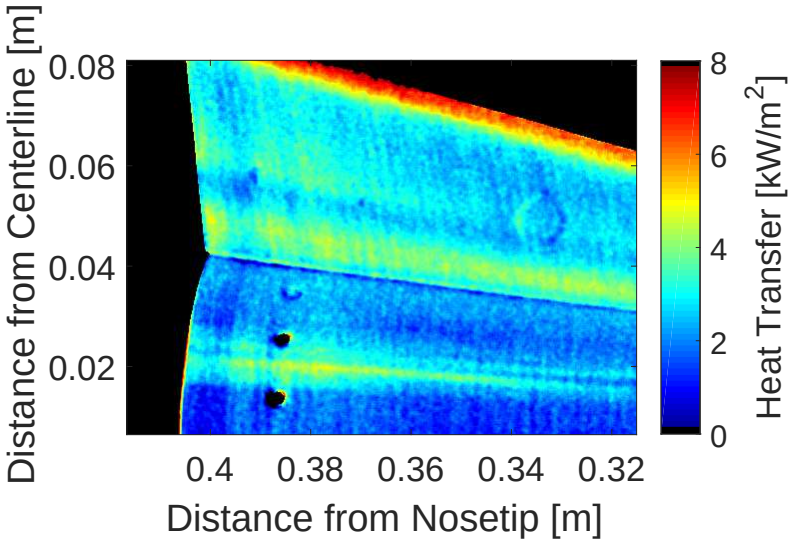

(a) Run 705, 75° sweep, unit Re = 6.85 x 10^6 m^{-1}

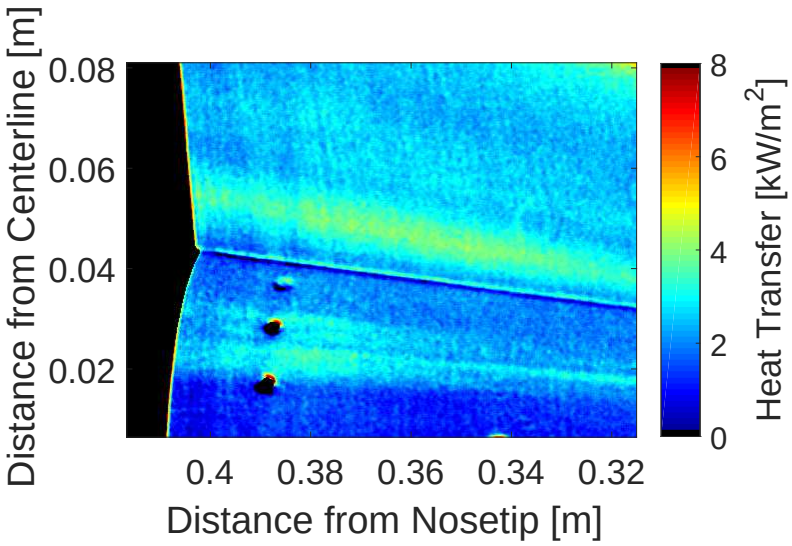

(b) Run 719, 70° sweep, unit Re = 6.85 x 10^6 m^{-1}

Figure 4.24. Increasing fin sweep decreases streak spreading at a similar Reynolds number. Three-fin model shown with R_{LE}=1/8" and a sharp nosetip.

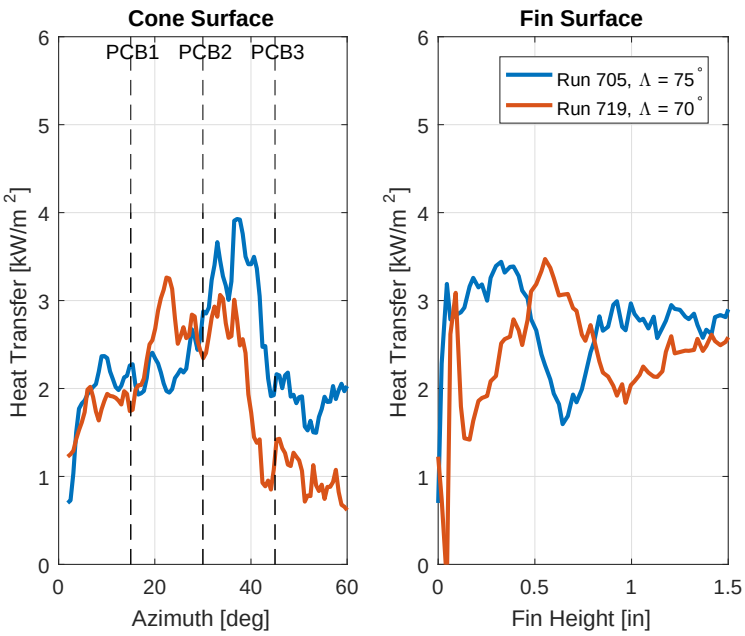

Figure 4.25. Increasing fin sweep narrows the streaks and moves the fin streak closer to the corner. Slices of TSP images at x = 0.368 meters. Three-fin model with R_{LE}=1/8" and a sharp nosetip.

The effect of fin sweep was tested again for a model with a 1/8-inch leading edge radius and a 1 mm radius nosetip. The TSP images for this case are shown in Figure 4.26 for both fin sweeps at a similar Reynolds number. These images show a decrease in streak spreading for increased sweep, similar to what was seen for the sharp nosetip measurements. Figure 4.27 shows an azimuthal slice of the TSP for these images. The cone streaks are farther from the corner for the higher sweep fin. The fin streaks are farther from the corner for the fin with less sweep.

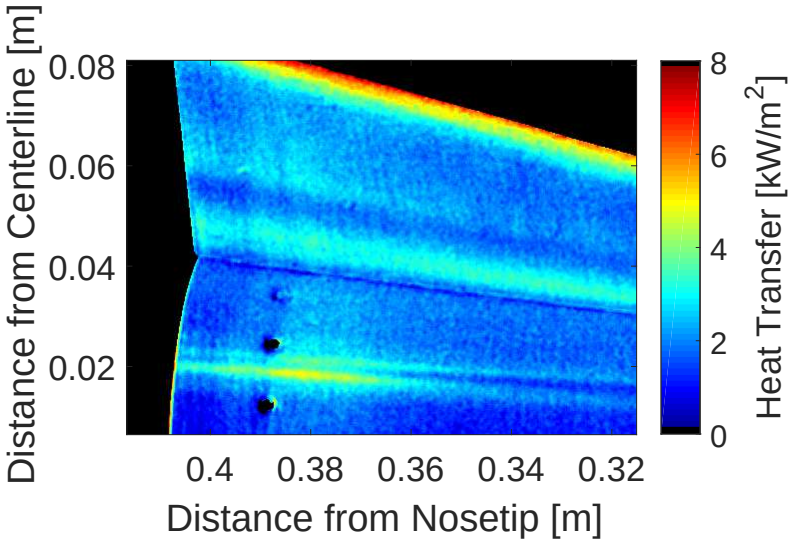

(a) Run 711, 75° sweep, unit Re = 7.20 x 10^6 m^{-1}

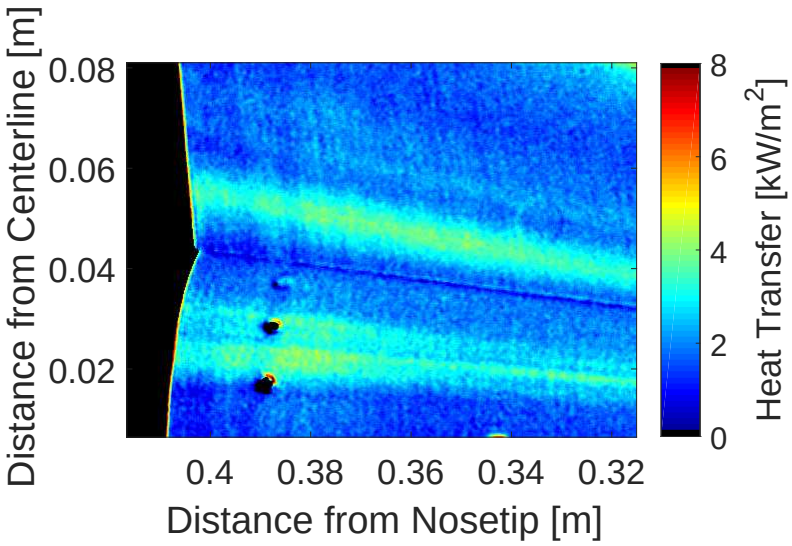

(b) Run 723, 70° sweep, unit Re = 7.20 x 10^6 m^{-1}

Figure 4.26. Increasing fin sweep decreases streak spreading at a similar Reynolds number. Three-fin model shown with R_{LE}=1/8" and R_{NT}=1 mm.

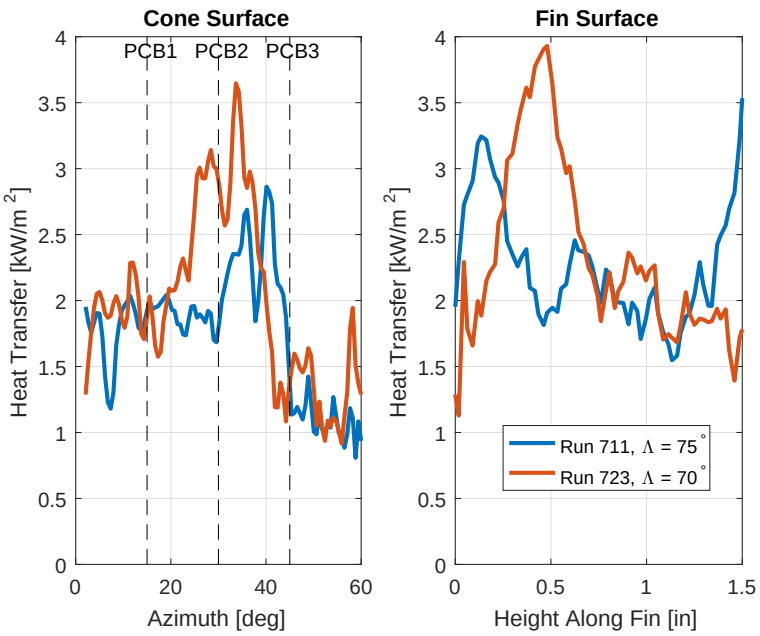

Figure 4.27. Increasing fin sweep narrows the streaks and moves the fin streak closer to the corner. Slices of TSP images at x = 0.356 meters. Three-fin model with R_{LE}=1/8" and R_{NT}=1 mm.

4.5.3 Pressure Fluctuation Data for Fin Sweep of 70° and 75°

Figure 4.28 shows PSD plots calculated from the pressure fluctuations for the sharp nosetip case. All pressure sensor locations show clearly higher levels of pressure fluctuations at a similar Reynolds number for the 70° fin sweep as compared to the 75° fin sweep. Table 4.7 lists the RMS pressure fluctuations for all three PCB locations. Increasing fin sweep decreases fluctuation levels indicating a delay in transition. This is an effect of higher sweep delaying streak spreading but also the streak moving relative to the sensors.

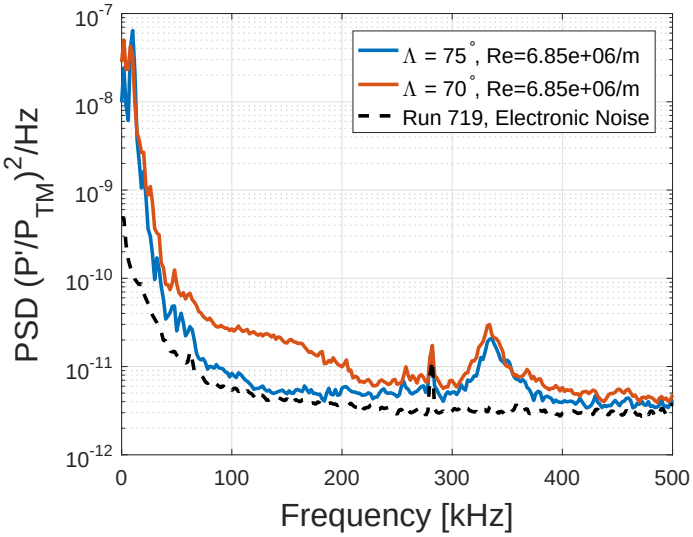

(a) Sensor 15° from fin

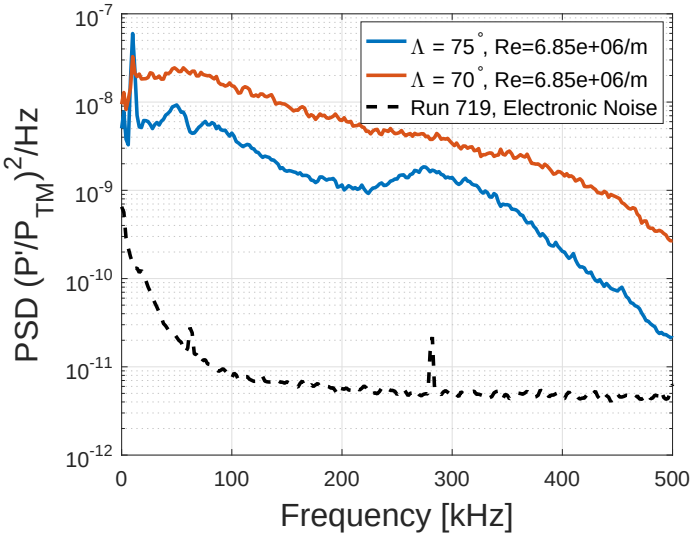

(b) Sensor 30° from fin

Figure 4.28. Increasing fin sweep decreases the amplitude of the pressure fluctuation power spectra, indicating delayed transition. Three-fin model shown with R_{LE}=1/8" and a sharp nosetip.

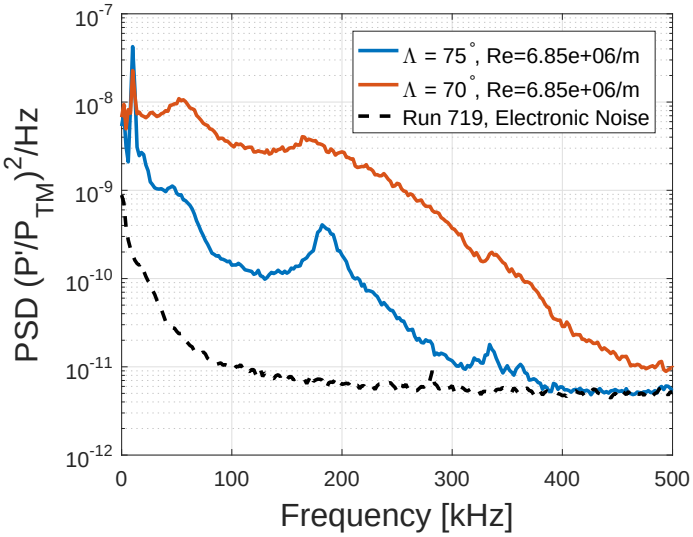

(c) Sensor 45° from fin

Figure 4.28. (cont'd) Increasing fin sweep decreases the amplitude of the pressure fluctuation power spectra, indicating delayed transition. Three-fin model shown with R_{LE}=1/8" and a sharp nosetip.

Table 4.7. RMS pressure fluctuations ($\frac{P'_{RMS}}{P_{TM}}$) for two sweep angles and a sharp nosetip.

Sensor	$\Lambda = 75°$	$\Lambda = 70°$
PCB1	0.24%	0.33%
PCB2	2.91%	5.65%
PCB3	0.82%	3.05%

Figure 4.29 shows the PSD plots calculated from the pressure fluctuations for the 1 mm nosetip radius measurements. As seen for the sharp nosetip measurements, increasing fin sweep decreases the amplitude of the pressure fluctuations for all three sensors. The RMS pressure fluctuations given in Table 4.8 show a corresponding decrease in the pressure fluctuation level, indicating that increasing nosetip radius delays transition. Again, this is a factor of the streak spreading less for higher sweep and of the streak moving relative to the sensor locations.

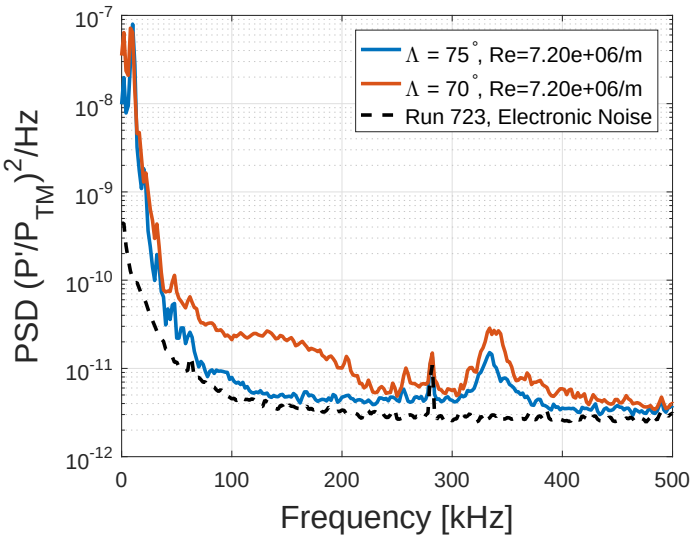

(a) Sensor 15° from fin

Figure 4.29. Increasing fin sweep decreases the amplitude of the pressure fluctuation power spectra, indicating delayed transition. Three-fin model shown with R_{LE}=1/8" and R_{NT}=1 mm.

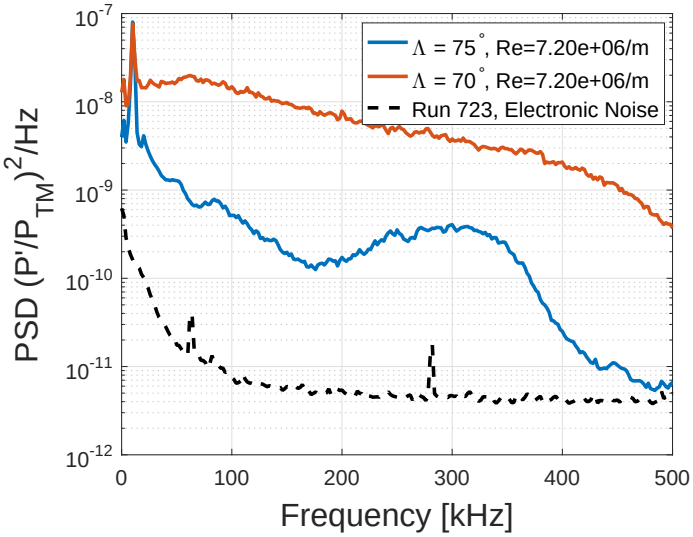

(b) Sensor 30° from fin

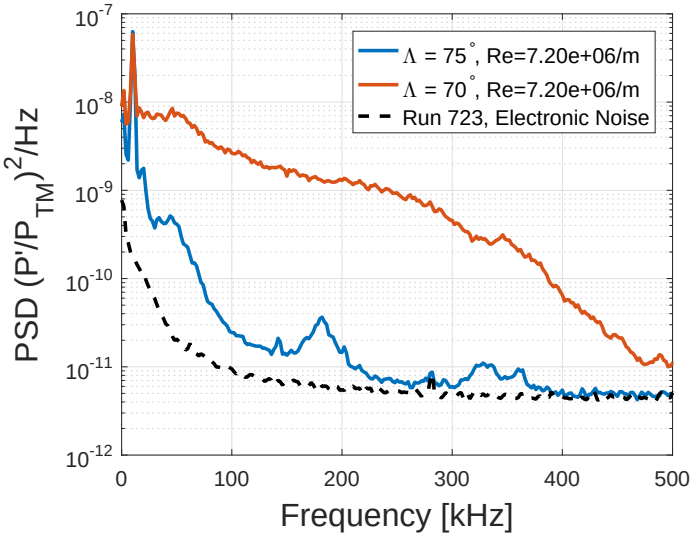

(c) Sensor 45° from fin

Figure 4.29. (cont'd) Increasing fin sweep decreases the amplitude of the pressure fluctuation power spectra, indicating delayed transition. Three-fin model shown with R_{LE}=1/8" and R_{NT}=1 mm.

Table 4.8. RMS pressure fluctuations ($\frac{P'_{RMS}}{P_{TM}}$) for two sweep angles and a 1 mm radius nosetip.

Sensor	$\Lambda = 75°$	$\Lambda = 70°$
PCB1	0.23%	0.33%
PCB2	1.20%	5.56%
PCB3	0.45%	2.57%

4.6 Fin Bluntness

4.6.1 TSP Data for Three Fin Leading Edge Radii

Three fin leading-edge radii have been tested to assess how fin bluntness affects the fin-cone interaction. Fin bluntness has been shown to be a main factor in the lateral extent of the interaction region in unswept configurations [48]. Figure 4.30 shows the heating pattern for a 70° fin sweep and a sharp nosetip for three fin radii of 1/8 inches, 3/32 inches, and 1/16 inches at a similar Reynolds number. The heating levels are uncertain due to changes in paint from entry to entry, but the streaks have shifted and spread. From the TSP images it can be seen that the cone streak moves toward the corner with decreasing leading-edge radius. Figure 4.31 shows a TSP slice upstream of the sensors for the three cases shown in Figure 4.30. Each decrease in fin radius moves the streak towards the corner by roughly 15° azimuthally. The relationship is likely not truly linear. The spreading of the cone streaks is more extensive for the larger bluntness fins indicating that increases in the fin leading edge radius will cause earlier boundary-layer transition as well. The streaks on the fin surface are seemingly unchanged in size and location. The higher background heating in Figure 4.30b is due to the quick succession of runs, however the streaks are still visible.

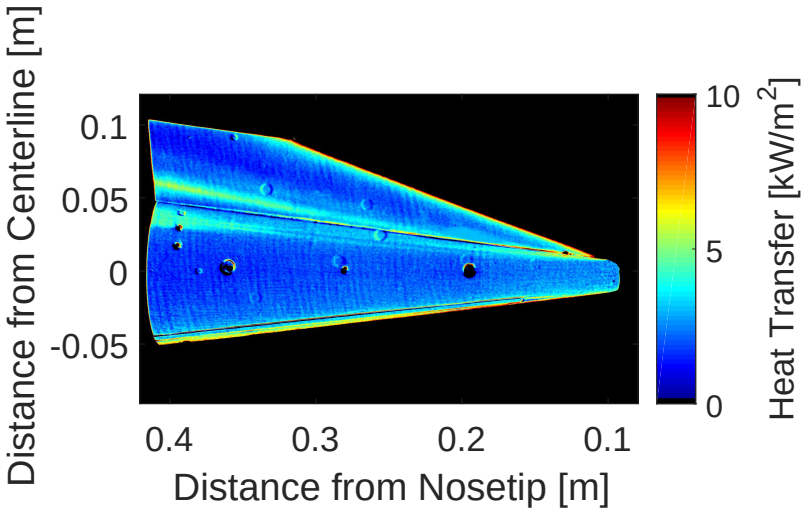

(a) Run 518, R_{LE} = 1/16", unit Re = 8.36 x 10^6 m^{-1}

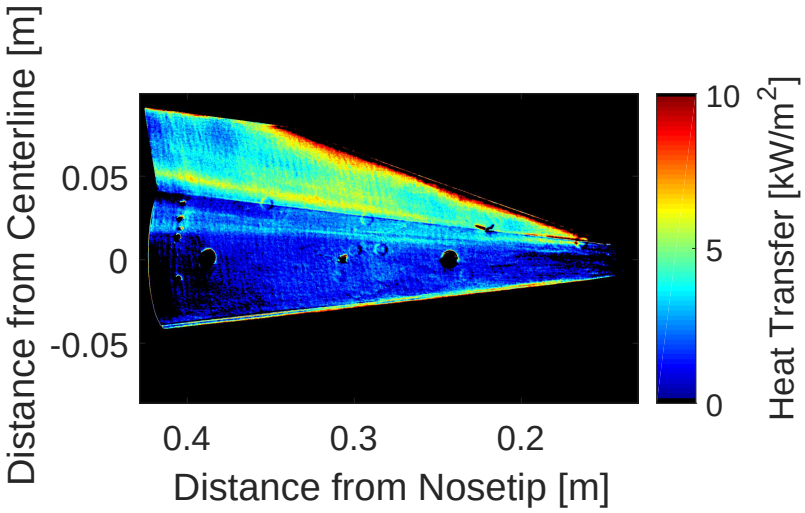

(b) Run 608, R_{LE} = 3/32", unit Re = 8.36 x 10^6 m^{-1}

Figure 4.30. Increasing fin bluntness moves the streak on the cone surface away from the corner. Three-fin model shown with a sharp nosetip and 70° sweep.

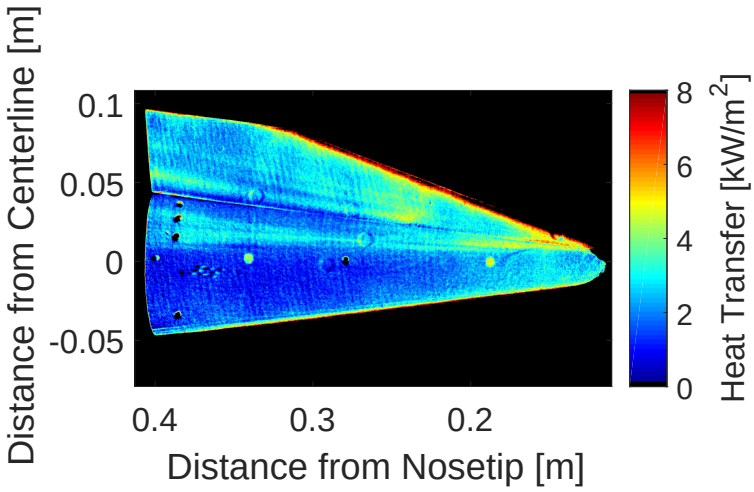

(c) Run 231, R_{LE} = 1/8", unit Re = 8.36 x 10^6 m^{-1}

Figure 4.30. (cont'd) Increasing fin bluntness moves the streak on the cone surface away from the corner. Three-fin model shown with a sharp nosetip and 70° sweep.

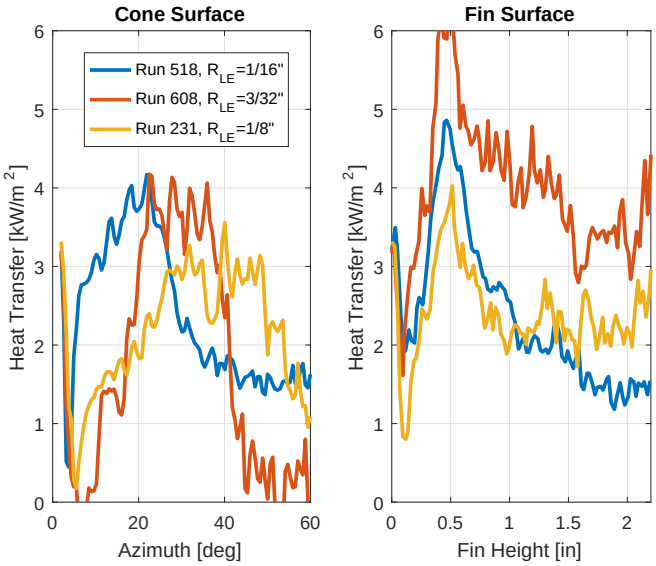

Figure 4.31. Increasing fin bluntness moves the streak on the cone surface away from the corner. Slice of TSP images at x = 0.373 meters for Runs 518, 608, and 231 at Re = 8.36 x 10^6 m^{-1}.

4.6.2 Pressure Fluctuation Data for Three Fin Leading Edge Radii

Power spectral density plots for the three sensors in the corner interaction region for the case with a 1/16-inch fin leading edge radius are shown in Figure 4.32. The streak in this case has moved very close to the corner, between the sensors at 15° and 30° from the corner. A peak at a frequency around 200 kHz is seen for the sensor closest to the corner in Figure 4.32a. Another small peak is measured at 50 kHz at the lowest unit Reynolds number. Similar peaks are seen in Figure 4.32b, however, there are unexpected peaks around 170 kHz and 320 kHz. The pressure measurements from Entry 5 all show this phenomenon, and it is expected that these are due to interference from the nozzle wall hot film array. Similar disturbances are seen in Figure 4.32c which is well away from the streak. The nozzle wall hot film array has since been replaced with a smaller sensor. Future experiments will determine if the new, smaller sensor eliminates this problem.

Similar plots are shown in Figure 4.33 for the case with the 3/32-inch leading edge radius. In this case, the streaks are coincident with the sensor at 30° from the fin, therefore the power spectra are completely turbulent. The sensor closest to the fin measures a peak at 350 kHz and broadband increases in amplitude as the Reynolds number increases. The sensor farthest from the fin measures two high frequency peaks, one at 200 kHz and another around 350 kHz. The 200 kHz instability is likely second-mode. The source of the 350 kHz peak is unknown.

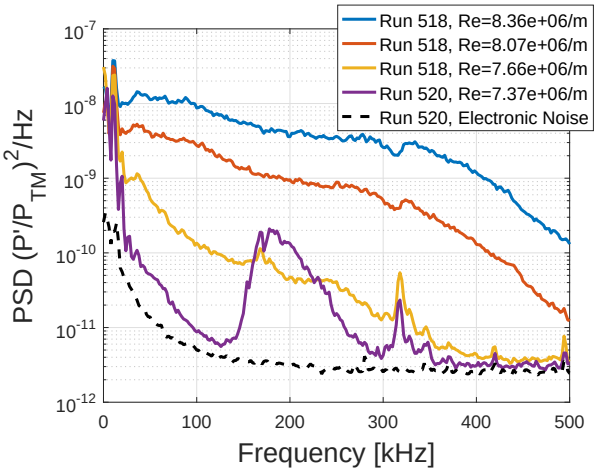

(a) Sensor 15° from fin

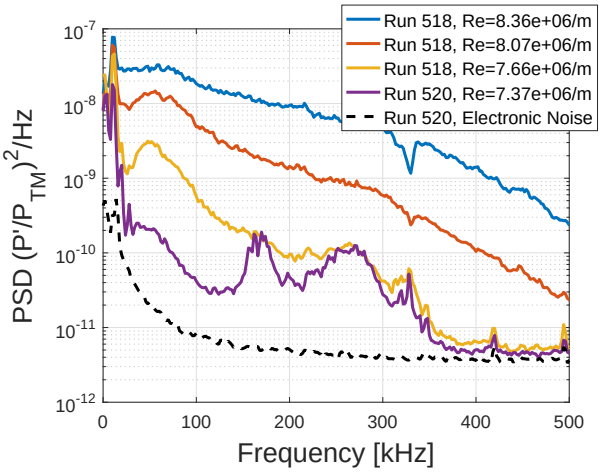

(b) Sensor 30° from fin

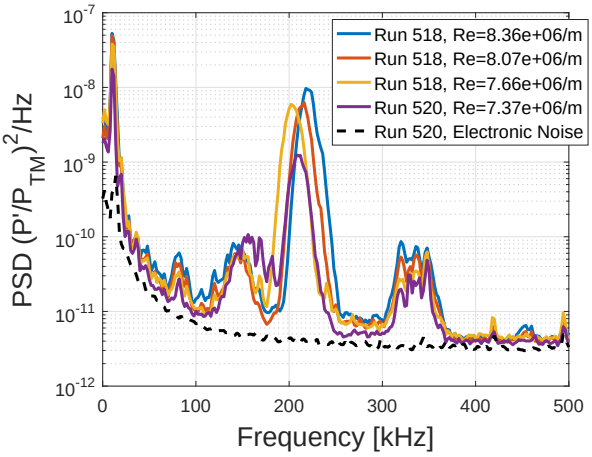

(c) Sensor 45° from fin

Figure 4.32. Power spectra corresponding with vortex system very near the corner. Measurements on three-fin model with R_{LE}=1/16", 70° sweep, and a sharp nosetip.

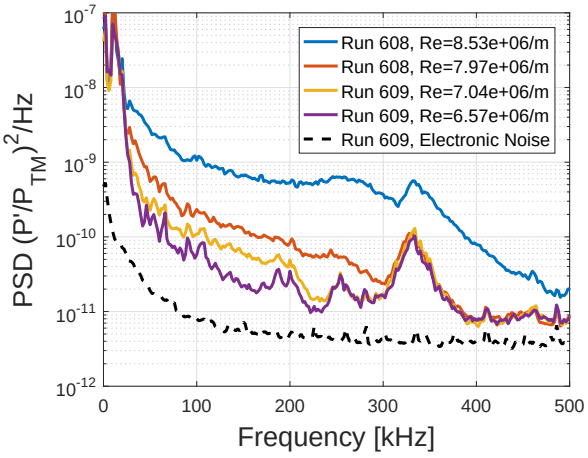

(a) Sensor 15° from fin

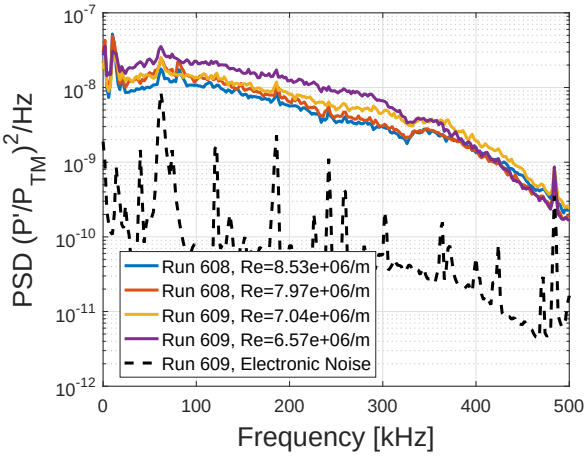

(b) Sensor 30° from fin

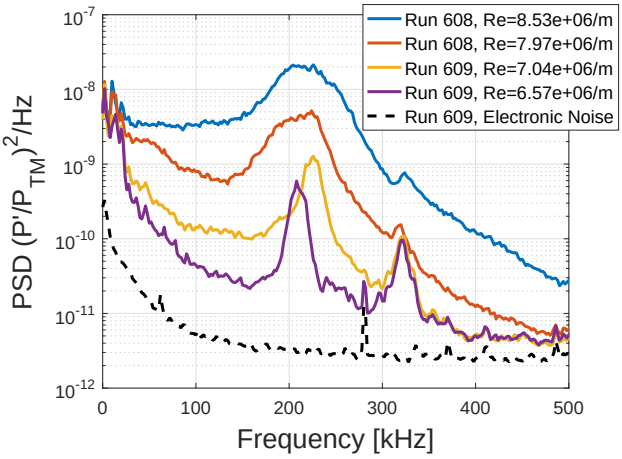

(c) Sensor 45° from fin

Figure 4.33. Power spectra corresponding with vortex system coincident with the sensor at 30° from the fin. Measurements on three-fin model with R_{LE}=3/32", 70° sweep, and a sharp nosetip.

4.7 Pressure Fluctuations Far from the Fin Interaction Region

Pressure fluctuation measurements have been made far from the fin-cone interaction region. Pressure-fluctuation power spectra are shown in Figure 4.34 for all of the PCB sensors outside of the corner region for Run 605. One peak is seen at 200 kHz which is in the range expected for the second-mode instability on a 7° straight cone at this axial station based on estimates from STABL in Figure 4.13. Another peak occurs at 330 kHz whose origin is uncertain. This peak at 330 kHz also appears in measurements made on a straight cone while aligning of the model during the same entry, as shown in Figure 4.35. The Senflex hot film array that was mounted on the tunnel wall has been shown to increase heating at the aft end of some models, so contamination from a wave from the hot film could be a possibility. This hot film has since been replaced with a less intrusive sensor, so further experiments will be needed to confirm this possibility. Other possible factors are PCB resonance or model vibration.

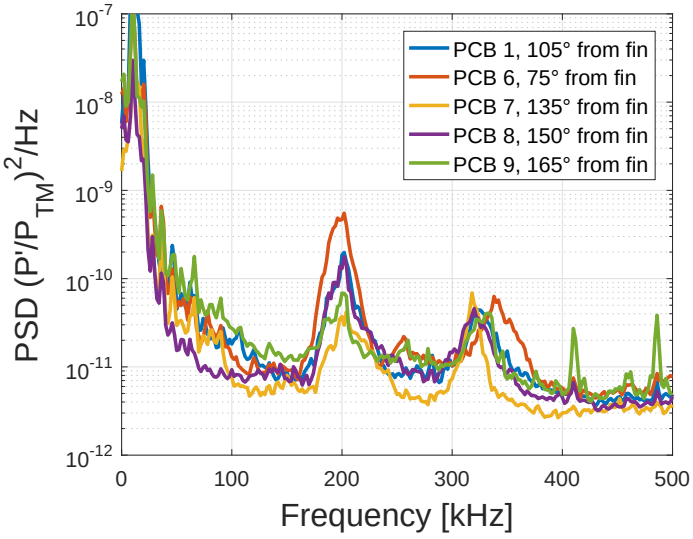

Figure 4.34. Power spectra for sensors far from the corner region for Run 605 (unit Re = 8.5 x 10^6 m^{-1}). Three-fin model shown with sharp nosetip, 75° sweep, and R_{LE}=3/32".

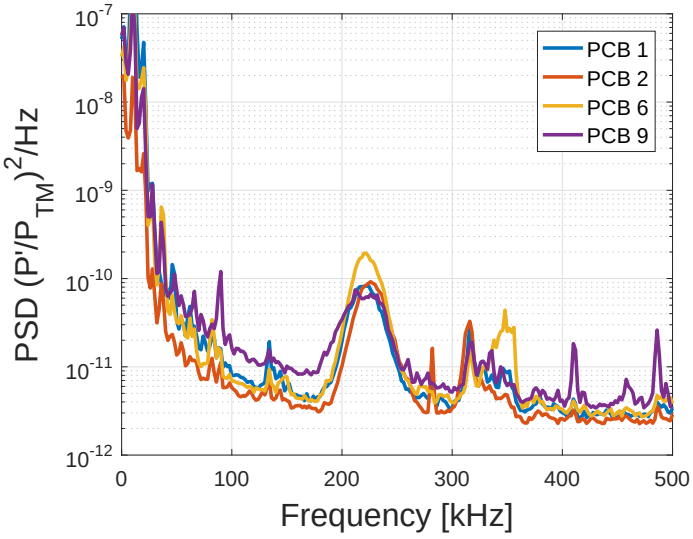

Figure 4.35. Power spectra for sensors around the azimuth of a 7° straight cone for a unit Reynolds number of 9.27 x 10^6 m^{-1}. Shows same peaks as sensors away from fin interaction region. Measurements were made while aligning the model during Entry 6.

4.8 Angle of Attack

Due to the extensive testing required at 0° angle of attack only a few runs were performed at 4° angle of attack and they were purely exploratory. The cone was tested in two orientations. The cone was first installed and tested with the fin on the windward ray, as in Figure 3.14. The cone was then rolled 90° so that the fin was on the yaw side and tested again, as in Figure 3.15. These runs were all done at high pressure and therefore have high heating and extensive spreading of the streaks. Much of the pressure fluctuation data was either turbulent or has high levels of electronic noise and is not presented. More work will need to be done to characterize this flow field and determine the effects of angle of attack on transition and boundary-layer instabilities. Heating streaks over the SB sensor made TSP calibration impossible, so temperature change is shown instead of heat transfer.

Figure 4.36 shows a TSP image of a maximum quiet Reynolds number case where the fin is on the windward ray. An image with the cone at 0° angle of attack is given in Figure 4.37 for comparison. At a 4° angle of attack transition appears to have started farther upstream than it does at a 0° angle of attack. The temperature change at 4° angle of attack is much higher than for the same configuration at 0° angle of attack as might be expected. The streak on the cone surface has also moved significantly away from the corner indicating that the pressure difference from the windward to the leeward side is moving the vortex system. Outside of the fin interaction region there appears to be crossflow vortices. These occur both on the cone surface and farther outboard on the fin surface. The vortex in the corner on the fin surface appears to have an additional streak.

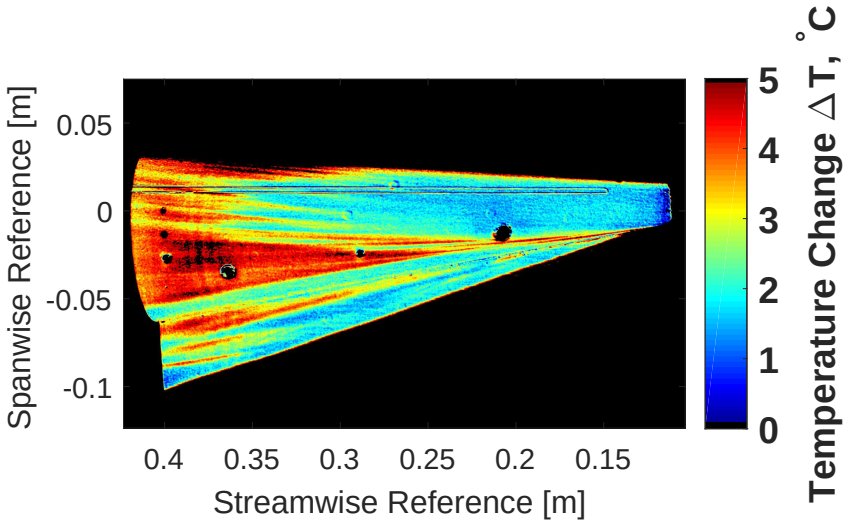

Figure 4.36. Temperature change for the fin-cone at 4° angle of attack with the fin on the windward ray (Run 314, Re = 12.1 x 10^6 m^{-1}). Three-fin model shown under quiet flow with a sharp nosetip, 75° fin sweep, and R_{LE} = 1/8".

Figure 4.38 shows a TSP image of the cone with the fin on the yaw side. The camera angle, Camera 1 from Figure 3.15, views the leading edge of the fin. In this case the fin is inclined to the freestream flow resulting in an expansion on the upper

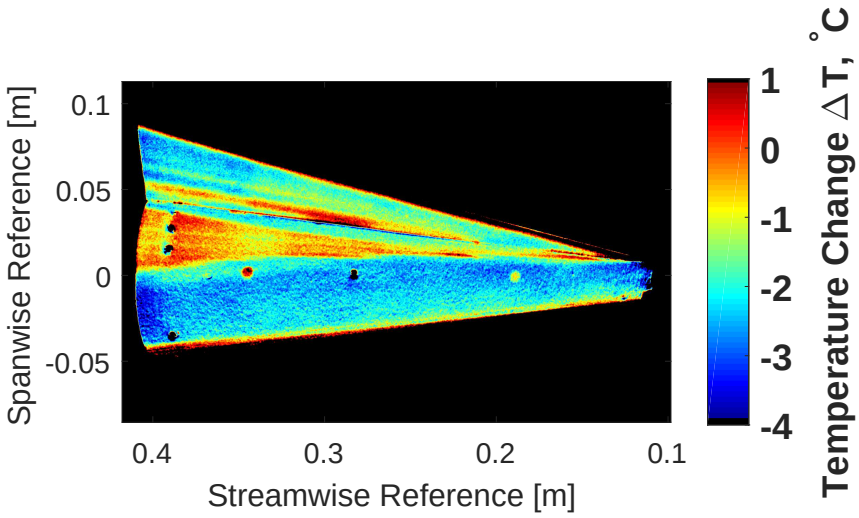

Figure 4.37. Temperature change for the fin-cone at 0° angle of attack (Run 109, Re = 12.4 x 10^6 m^{-1}). Three-fin model shown under quiet flow with a sharp nosetip, 75° fin sweep, and R_{LE} = 1/8".

surface of the fin and an oblique shock on the lower surface. The hot-flow region on the cone below the fin is much closer to the fin than what was measured for any other configuration with the same leading edge bluntness. This is also likely due to the pressure difference from the windward to the leeward side. On the leeward side of the fin where the flow expands there is no indication of a large vortex system. Only two small streaks are measured, one close to the corner and one farther out. The streak closer to the corner dissipates quickly and the heat transfer is greatly reduced farther downstream.

With the fin-cone in the same orientation with respect to the flow, the camera angle was adjusted to the Camera 2 view from Figure 3.15. Figure 4.39 shows the leeward ray of the cone with the fin on the yaw side. There is low heating close to the corner on the cone surface and one streak emanating from the fin root farther from the corner. These features correspond with the streaks seen in the upper portion of Figure 4.38. Crossflow vortices from the non-fin side of the cone are also apparent.

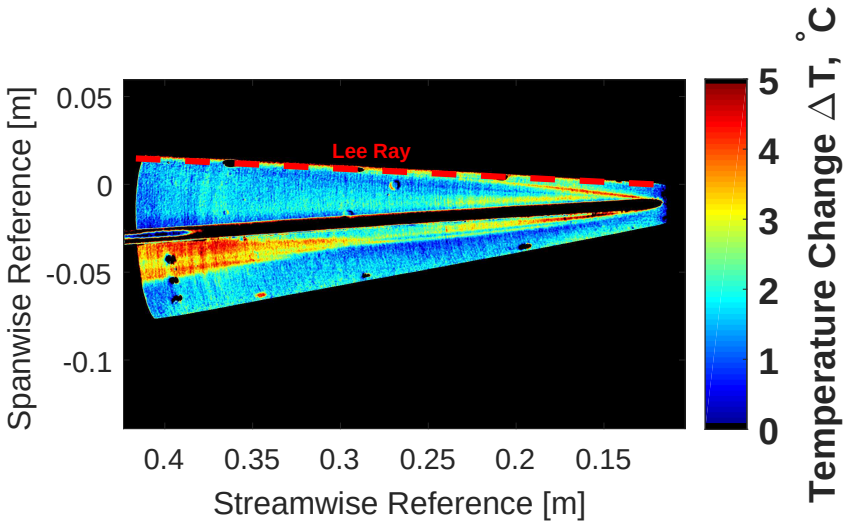

Figure 4.38. Temperature change for the fin-cone at 4° angle of attack with the fin on the yaw side (Run 316, Re = 10.1 x 10^6 m^{-1}). Camera is viewing the side of the cone where the fin is attached. Three-fin model shown under quiet flow with a sharp nosetip, 75° fin sweep, and R_{LE} = 1/8".

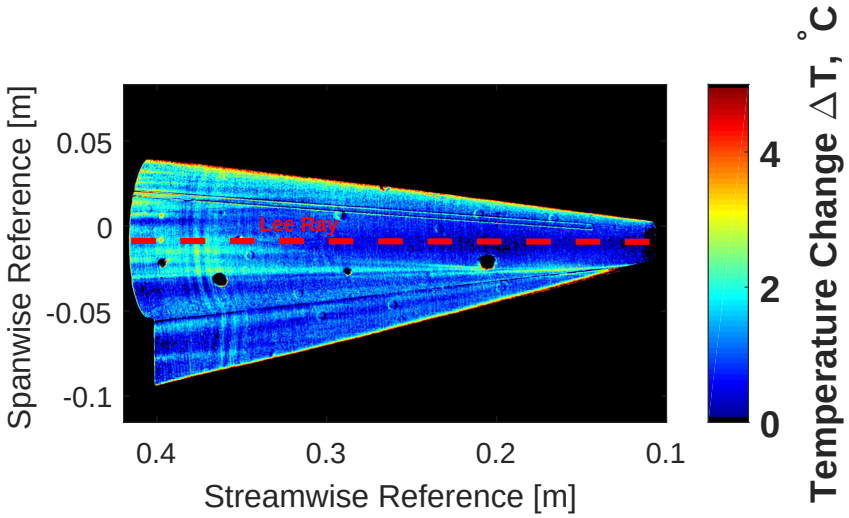

Figure 4.39. Temperature change for the fin-cone at 4° angle of attack with the fin on the yaw side (Run 321, Re = 9.97 x 10^6 m^{-1}). Camera is viewing the lee ray of the cone. Three-fin model shown under quiet flow with a sharp nosetip, 75° fin sweep, and R_{LE} = 1/8".

4.9 Comparison with Stability Analysis

Dr. Helen Reed's group at Texas A&M University provided preliminary mean flow and stability computations of the fin-cone geometry [49]. The mean flow was obtained using the Data Parallel Line Relaxation Code (DPLR) which includes a Navier-Stokes solver. Stability analysis was performed using linear stability theory (LST), linear parabolized stability equations (LPSE), and Spatial BiGlobal methods (SBG). The grid utilizes 745 cells in the streamwise direction, 600 cells in the wall normal direction, and 451 cells around the azimuth. Simulations were done for the cone at 0° angle of attack, with a 2 mm nosetip radius, a 3/32-inch leading edge radius, and a 75° fin sweep. The flow conditions used are given in Table 4.9.

Table 4.9. CFD simulation conditions

M	p_0	T_0	T_w	Re
6.0	101.3 psia	435.15 K	300 K	7.4 x 10^6 m^{-1}

A Mach contour plot for the fin-cone is displayed in Figure 4.40. Slices of this Mach contour are shown for three axial stations in Figure 4.41. Distortions of the boundary layer are seen on both the fin surface and cone surface. Far upstream at 0.108 meters, near the fin root, the beginnings of a corner vortex can be seen, as indicated by a bulge in the boundary layer. Farther downstream, two vortices are apparent that resemble the flowfield found by Fomison [29]. The vortex in the corner is much more tightly wound than the vortex on the cone surface. At the farthest downstream station, the corner vortex has lifted off of the cone surface and has moved up the fin. Two vortices are now seen on the fin surface. On the cone surface, the vortex has become significantly flattened. The boundary layer on the cone surface near the fin is thinner than seen elsewhere on the cone.

Figure 4.42 shows the heating pattern obtained from CFD. A experimental comparison for this computation is not possible with the current data set. However, the

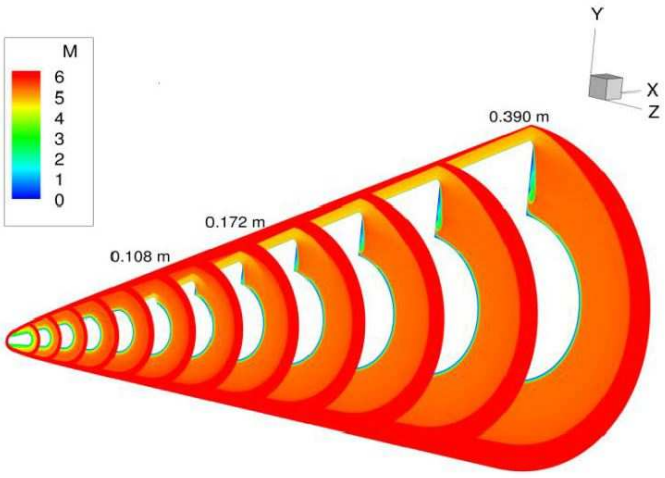

Figure 4.40. Mach contour computed for fin-cone geometry with 75° fin sweep, R_{NT}= 2 mm, and R_{LE}=1/8" at Re = 7.4 x 10^6 m^{-1}.

experimental heating pattern for a configuration with a 1/8-inch fin leading-edge radius at a similar Reynolds number is shown in Figure 4.43. The computations and experiments with regard to heating show good agreement. The two fin streaks correspond to the two vortices seen in the Mach contours. The path angle of the streaks is hard to compare because the imaging angle of the cone in the experiment is different than for the CFD image. More comparisons are to be obtained in the future.

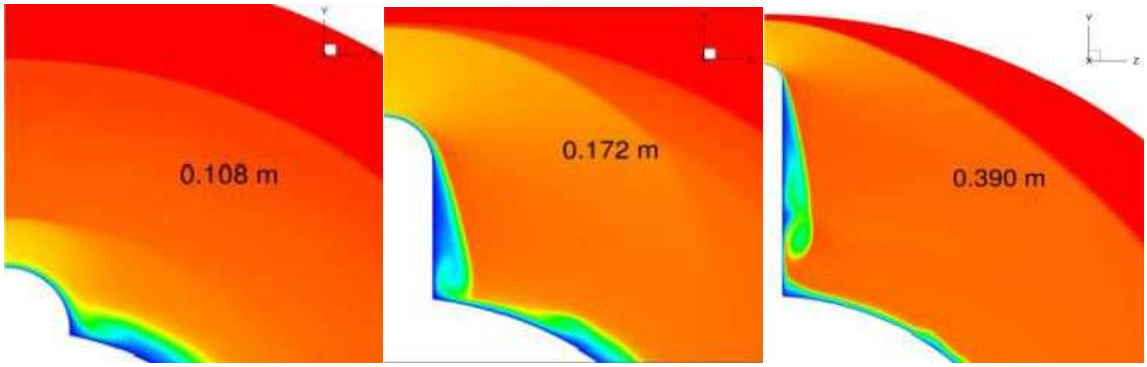

(a) x = 0.108 m (b) x = 0.172 m (c) x = 0.390 m

Figure 4.41. Vortices present in the corner on the cone and fin surfaces.

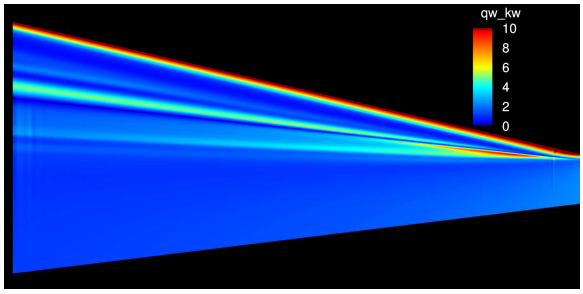

Figure 4.42. Heating pattern computed for fin-cone geometry with 75° fin sweep, R_{NT}= 2 mm, and R_{LE}=3/32" at Re = 7.4 x 10^6 m^{-1}.

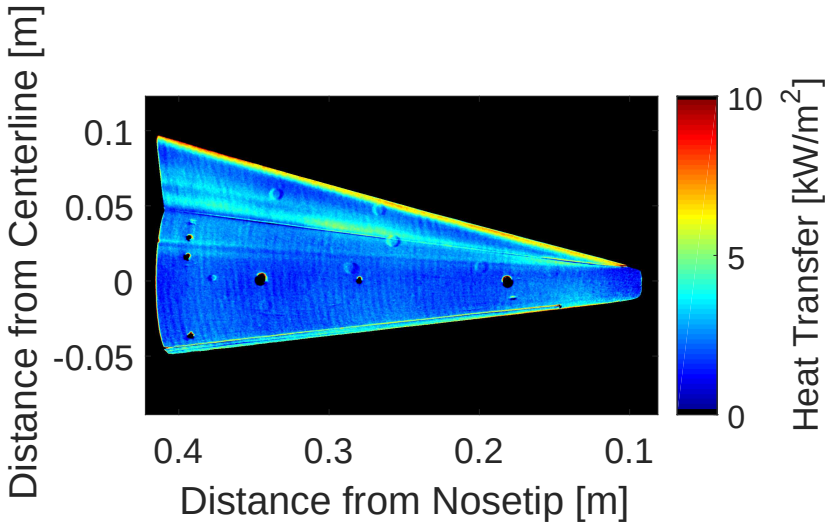

Figure 4.43. Heating pattern matches qualitatively with CFD (Run 508, Re = 7.38 x 10^6 m^{-1}). Three-fin model shown with with 75° fin sweep, R_{NT}= 2 mm, and R_{LE}=1/8"

A linear stability analysis along a streamline that passes near the PCB 30° from the fin computed two possible instabilities, one at 260 kHz and another at 30 kHz. The high-frequency peak computed is two-dimensional in nature. High-frequency instabilities have been identified experimentally at between 150 kHz and 250 kHz, and are likely related to the second-mode instability. In addition, far inside the streak near the corner, a peak in the experimental power spectra has been seen at 300 kHz. The computed low-frequency peak is three-dimensional in nature and is most amplified at an azimuthal wave number of 40. A low-frequency instability has been identified around 50 kHz in the experiments near the corner region.

5. SUMMARY

This research explored instability and transition on a 7° half-angle cone with highly-swept fins. A cone was fabricated that could be used to explore a wide parameter space including fin sweep, fin bluntness, nose bluntness, and angle of attack. The flowfield shares many of the characteristics associated with glancing shock-wave flows and axial corner flows. The heating pattern on the surface indicated the existence of a vortex system in the corner region. Under noisy flow this heating pattern was markedly different than under quiet flow.

Under quiet flow, multiple streaks of heat transfer were seen on both the cone and fin surface. There were two streaks of heat transfer on the cone surface at most Reynolds numbers, but three were seen near the maximum quiet Reynolds number. A Reynolds number sweep demonstrated that the streaks spread azimuthally and increase in heat transfer as the unit Reynolds number increased. On the fin, one broad streak was seen at all Reynolds numbers close to the corner. Several other smaller streaks are seen farther outboard of this corner streak.

As the heating streaks on the cone surface spread over the pressure sensors at the aft end, a broadband increase in the amplitude of the pressure fluctuations was seen, indicating the onset of transition. Several boundary layer instabilities appeared in the power spectral density plots calculated from the pressure fluctuation measurements. One of these instabilities is centered around 50 kHz and is present in all configurations. The other is centered between 150 and 250 kHz and appears to be related to the second-mode instability. A third peak in the power spectra was identified for the pressure sensors closest to the corner. This peak was less sensitive to Reynolds number and is possibly due to effects unrelated to the flow field such as sensor resonance.

Nose bluntness was evaluated with a nominally sharp nosetip, a 1 mm radius nosetip, and a 2 mm radius nosetip. TSP measurements indicated less spreading of

the streaks for the larger nose radii than was seen for the sharp nosetip at similar Reynolds numbers. Increasing nose radius reduced the level of the RMS pressure fluctuations. The power spectral density plots showed a corresponding decrease in the broadband amplitude of the pressure fluctuations. The power spectra also indicate that increasing nose radius decreased the amplitude of the high-frequency instability, which is believed to be the second-mode instability.

The effect of fin sweep was evaluated with sweep angles of 70° and 75°. TSP measurements indicated that increasing fin sweep reduces streak spreading and therefore delays transition. This effect is also supported by the RMS pressure fluctuations. Increasing fin sweep was also shown to move the cone streaks farther from the corner and move the fin streaks closer to the corner.

Three fin radii were tested, with radii of 1/8, 3/32, and 1/16 inches, to assess the effect of fin bluntness. Increasing fin bluntness was shown to increase the lateral extent of the interaction. Streak spreading was reduced for smaller fin radii indicating delayed transition. The lack of quality TSP images and clean pressure fluctuation data at similar Reynolds number drives the need for more investigation on the effects of fin bluntness.

Preliminary computational results show encouraging agreement with experiments. Stability analyses have been able to identify instabilities in the same frequency range as were seen in experiment. More work will need to be done to correlate amplification rates and N-factors to the measured transition locations.

5.1 Future Work

In the near term, much work should be done to finish up the parametric survey. This should start with making additional measurements on fin bluntness effects. The current TSP measurements are insufficient to make good comparisons at similar Reynolds number, and more pressure measurements should be made to establish repeatability. The next step should then be to improve the image processing techniques.

Issues with resolution of the TSP images makes it difficult to find the edges of the streaks, and therefore how much the streaks have spread. New methods to smooth and average the TSP measurements will enhance the value of the current data. This effort will also make determination of a transition location possible in the absence of upstream pressure sensors.

A wide parameter space has been investigated in a preliminary way, however, little is known about the streamwise growth of the vortex system. The author plans to continue this work toward his PhD by narrowing the parameter space and focusing closely on collecting data to more thoroughly understand the fin-cone interaction region. Toward that end, the following items are suggested for further work:

1. The parameter space was large for the initial tests. To reduce this parameter space, it is suggested that the 1/8-inch fin leading edge radius should be the primary test case. Using one fin slot reduces the number of model changes made during a tunnel entry, which increases the total amount of runs. This fin also had fewer TSP issues because of its thickness. Future tunnel modifications and the resulting quiet-flow performance will determine which fin sweeps and nose radii will be tested. The highest fin sweep (70°, 75°, or 80°) possible should be tested given the new maximum quiet Reynolds number. The nosetips should be limited to two: the sharp nosetip and either the 1 mm or 2 mm nose radius.

2. The lack of sensor space on the fin makes it difficult to get a reliable TSP calibration for heat transfer. IR imaging methods have been shown to have better signal-to-noise ratio and sensitivity. A method of reducing heat transfer from IR images is currently being developed for PEEK material. Obtaining global heat transfer measurements using a model constructed of PEEK should be a high priority. Other methods must be considered for direct measurement of heat transfer as well. Hot films are currently being considered as another plausible option.

3. Fast pressure transducers indicated several possible boundary-layer instabilities. Unfortunately few sensors were used in the initial testing to ease the parametric study. More sensors should be used, especially in the streamwise direction, to better evaluate the growth of these instabilities. A combination of Kulite XCQ-062-15A and PCB132B38 sensors are suggested to characterize these instabilities. The Kulite sensors have better frequency resolution below 100 kHz which will better characterize the low frequency instability. The PCB sensors are updates to the PCB132A31 sensors and have the sensing element centered on the sensor face. This will give better azimuthal resolution to the pressure fluctuation measurements. The fin should also be instrumented with low-profile Kulite LS-062 or Kulite XCE-SL-062 sensors.

4. Off-surface measurements should be a priority. A micro-pitot probe is currently being developed for use in the BAM6QT to make pressure measurements. FLDI is also being developed to measure density gradients in the BAM6QT.

5. Oil flow has been used in past corner flow experiments to determine if and where separation occurs as well as the number of separations. Run times are short in the BAM6QT making oil flow difficult, but this should be considered as possible future work.

6. Measurements at angle of attack have significance in possible applications of this work. Only preliminary measurements have been made thus far and no significant pressure data was taken. Further data at angle of attack with better heat transfer measurement are desirable.

REFERENCES

REFERENCES

[1] Joe D. Watts. Flight Experience with Shock Impingement and Interference Heating on the X-15-2 Research Airplane. TM-X-1669, NASA, October 1968.

[2] David S Dolling. Fifty Years of Shock-Wave/Boundary-Layer Interaction Research: What Next? *AIAA Journal*, 39(8):1517–1531, 2001.

[3] Steven P Schneider. The Development of Hypersonic Quiet Tunnels. *Journal of Spacecraft and Rockets*, 45(4):641–664, 2008.

[4] David F Fisher and N. Sam Dougherty Jr. In-Flight Transition Measurement on a 10° Cone at Mach Number From 0.5 to 2.0. NASA-TP-1971, June 1982.

[5] John Laufer. Aerodynamic Noise in Supersonic Wind Tunnels. *Journal of the Aerospace Sciences*, 28:685–692, 1961.

[6] Daniel C Reda. Boundary-Layer Transition Experiments on Sharp, Slender Cones in Supersonic Free Flight. *AIAA Journal*, 17(8):803–810, 1979.

[7] Brandon C. Chynoweth, Christopher A C Ward, Ryan O Henderson, George Moraru, Roger T Greenwood, Andrew D Abney, and Steven P Schneider. Transition and Instability Measurements in a Mach 6 Hypersonic Quiet Tunnel. AIAA Paper 2014-0074, January 2014.

[8] Dennis C Berridge, Christopher A C Ward, Ryan P K Luersen, Amanda Chou, Andrew D Abney, and Steven P Schneider. Boundary-Layer Instability Measurements in a Mach-6 Quiet Tunnel. AIAA Paper 2012-3147, June 2012.

[9] Robert H Korkegi. Survey of Viscous Interactions Associated with High Mach Number Flight. *AIAA Journal*, 9(5):771–784, 1971.

[10] Dietrich Hummel. Axial Flow in Corners at Supersonic and Hypersonic Speeds. In *Special Course on Three-Dimensional Supersonic/Hypersonic Flows Including Separation*, AGARD Report 764, pages 5.1–5.37. June 1990.

[11] Argyris G. Panaras. Review of the Physics of Swept-Shock/Boundary Layer Interactions. *Progress in Aerospace Sciences*, 32:173–244, 1996.

[12] Andrew F Charwat and Larry G Redekopp. Supersonic Interference Flow along the Corner of Intersecting Wedges. *AIAA Journal*, 5(3):480–488, 1967.

[13] Ralph D Watson and Leonard M Weinstein. A Study of Hypersonic Corner Flow Interactions. *AIAA Journal*, 9(7):1280–1286, 1971.

[14] James R Cooper and Wilbur L. Hankey Jr. Flowfield Measurements in an Asymmetric Axial Corner at M=12.5. *AIAA Journal*, 12(10):1353–1357, 1974.

[15] Robert H Korkegi. On the Structure of Three-Dimensional Shock-Induced Separated Flow Regions. *AIAA Journal*, 14(5):597–600, 1976.

[16] Hakan Papuccuoglu. Experimental Investigation of Hypersonic Three-Dimensional Corner Flow. *AIAA Journal*, 31(4):652–656, 1993.

[17] Calvin P Stainback and Leonard M Weinstein. Aerodynamic Heating in the Vicinity of Corners at Hypersonic Speeds. NASA-TN-D-4130, November 1967.

[18] John E West and Robert H Korkegi. Supersonic Interaction in the Corner of Intersecting Wedges at High Reynolds Numbers. *AIAA Journal*, 10(5):652–656, 1972.

[19] Robert H Korkegi. Effect of Transition on Three-Dimensional Shock-Wave/Boundary-Layer Interaction. *AIAA Journal*, 10(3):361–363, 1972.

[20] J.E. Green. Interactions Between Shock Waves and Turbulent Boundary Layers. *Progress in Aerospace Sciences*, 11:235–340, 1970.

[21] Gary S Settles and David S Dolling. Swept Shock Wave/Boundary-Layer Interactions. In Michael J Hemsch and Jack N Nielsen, editors, *Tactical Missile Aerodynamics*, volume 104 of *Progress in Astronautics and Aeronautics*, pages 297–379. AIAA, New York, 1986.

[22] John L Stollery. Some Aspects of Shock-Wave Boundary-Layer Interaction Relevant to Intake Flows. In *Hypersonic Combined Cycle Propulsion*, AGARD Conference Proceedings 479, pages 17.1–17.13. 1990.

[23] John L Stollery. Glancing Shock-Boundary Layer Interactions. In *Special Course on Three-Dimensional Supersonic/Hypersonic Flows Including Separation*, AGARD Report 764, pages 6.1–6.30. June 1990.

[24] Hayao Kubota and John L Stollery. An Experimental Investigation of the Interaction Between a Glancing Shock Wave and a Turbulent Boundary Layer. In Josef Singer and Rolf Staufenbiel, editors, *12th Congress of the International Council of the Aeronautical Sciences*, ICAS-80-14.1, Munich, Germany, 1980.

[25] Hayao Kubota and John L Stollery. An Experimental Study of the Interaction Between a Glancing Shock Wave and a Turbulent Boundary Layer. *Journal of Fluid Mechanics*, 116:431–458, 1982.

[26] Farrukh S Alvi and Gary S Settles. Physical Model of the Swept Shock Wave/Boundary-Layer Interaction Flowfield. *AIAA Journal*, 30(9):2252–2258, 1992.

[27] Gerard Degrez and Jean J Ginoux. Surface Phenomena in a Three-Dimensional Skewed Shock Wave/Laminar Boundary-Layer Interaction. *AIAA Journal*, 22(12):1764–1769, 1984.

[28] Louis G Kaufman, Robert H Korkegi, and Leo C Morton. Shock Impingement Caused by Boundary-Layer Separation Ahead of Blunt Fins. *AIAA Journal*, 11(10):1363–1364, 1973.

[29] N.R. Fomison. *The Effects of Bluntness and Sweep on Glancing Shock Wave Turbulent Boundary Layer Interaction*. PhD Dissertation, Cranfield Institute of Technology, September 1986.

[30] Wolfgang Möllenstädt. Experimentelle Untersuchungen an Längsangeströmten Eckenkonfigurationen im Hyperschallbereich. *Zeitschrift für Flugwissenschaften und Weltraumforschung*, 8:405–414, 1984.

[31] Wolfgang Möllenstädt. *Experimentelle Untersuchungen an Längsangeströmten, Gepfeilten Eckenkonfigurationen im Hyperschallbereich*. PhD Dissertation, Technischen Universität Carolo-Wilhelming zu Braunschweig, 1984.

[32] Dennis M Bushnell. Interference Heating on a Swept Cylinder in Region of Intersection with a Wedge at Mach Number 8. NASA-TN-D-3094, December 1965.

[33] N.R. Fomison and John L Stollery. The Effects of Sweep and Bluntness on a Glancing Shock Wave Turbulent Boundary Layer Interaction. In *Aerodynamics of Hypersonic Lifting Vehicles*, AGARD-CP-428, pages 8.1–8.18. November 1987.

[34] Shigeru Aso, Seishi Kuranaga, and Shigehide Nakao. Aerodynamic Heating Phenomena in Three-Dimensional Shock Wave/Turbulent Boundary Layer Interactions Induced by Sweptback Blunt Fins. AIAA Paper 90-0381, January 1990.

[35] T Taz Bramlette, Richard R Smith, and Neil J Sliski. Fin Induced Laminar Interactions on Sharp and Spherically Blunted Cones. *Journal of Spacecraft and Rockets*, 10(11):696–703, 1973.

[36] Joseph D Gillerlain Jr. Fin-Cone Interference Flow Field. AIAA Paper 79-0200, January 1979.

[37] Andrew Abney and Henry Rochlitz. Straight Cone with Fin in Mach 6 Quiet Tunnel. AAE 520 Final Report, Purdue University, March 2012.

[38] Brandon Chynoweth, Ryan Henderson, and George C Moraru. Investigation of Fin Geometries on a 7-Degree Half-Angle Cone at Mach 6. AAE 520 Final Report, Purdue University, June 2013.

[39] Matthew P Borg and Roger L Kimmel. Ground Test Measurements of Boundary-Layer Instabilities and Transition for the HIFiRE-5 at Flight Relevant Attitudes. AIAA Paper 2017-3135, June 2017.

[40] Brandon Chynoweth. *Measurements of Transition Dominated by the Second-Mode Instability at Mach 6*. PhD Dissertation, Purdue University, May 2018.

[41] Dennis C Berridge. *Generating Low-Pressure Shock Waves for Calibrating High-Frequency Pressure Sensors*. PhD Dissertation, Purdue University, December 2015.

[42] Kathryn A Gray, Brandon C Chynoweth, Joshua B Edelman, Gregory R McKiernan, Mark P Wason, and Steven P Schneider. Boundary-Layer Transition Measurements in the Boeing/AFOSR Mach-6 Quiet Tunnel. AIAA Paper 2017-0068, January 2017.

[43] John P Sullivan, Steven P Schneider, Tianshu Liu, Justin Rubal, Chris Ward, Joseph Dussling, Cody Rice, Ryan Foley, Zeimin Cai, Bo Wang, and Sudesh Woodiga. Quantitative Global Heat Transfer in a Mach-6 Quiet Tunnel. CR-2012-217331, NASA, February 2012.

[44] Cameron J Sweeney, Brandon C Chynoweth, Josh B Edelman, and Steven P Schneider. Instability and Transition Experiments in the Boeing/AFOSR Mach 6 Quiet Tunnel. AIAA Paper 2016-0355, January 2016.

[45] Kenneth F Stetson and Roger L Kimmel. On Hypersonic Boundary-Layer Stability. AIAA Paper 92-0737, January 1992.

[46] Mujeeb R Malik, Robert E Spall, and Chau-Lyan Chang. Effect of Nose Bluntness on Boundary Layer Stability and Transition. AIAA Paper 90-0112, January 1990.

[47] Anthony L Knutson. Direct Numerical Simulation of Mach 6 Flow over a Cone with a Highly Swept Fin. AIAA Paper 2018-0379, January 2018.

[48] David S Dolling. Comparison of Sharp and Blunt Fin-Induced Shock Wave/Turbulent Boundary-Layer Interaction. *AIAA Journal*, 20(10):1385–1391, 1982.

[49] Dr. Helen Reed. Personal Communication. October 2017.

APPENDICES

A. Model Drawings

A.1 Single-Fin Model

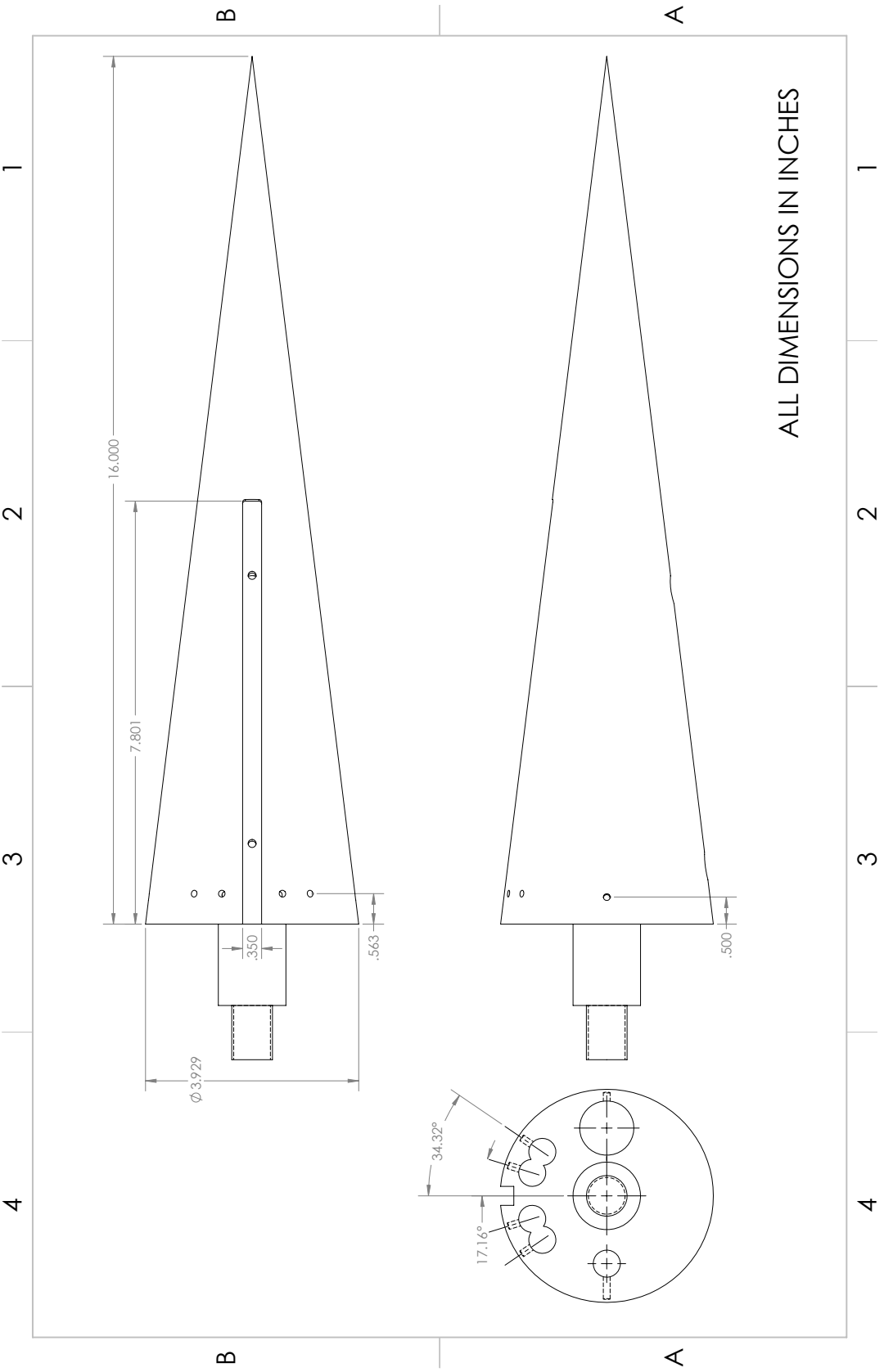
ALL DIMENSIONS IN INCHES
16.000
7.801
.350
.563
Ø3.929
.500
34.32°
17.16°
A
B
1
2
3
4

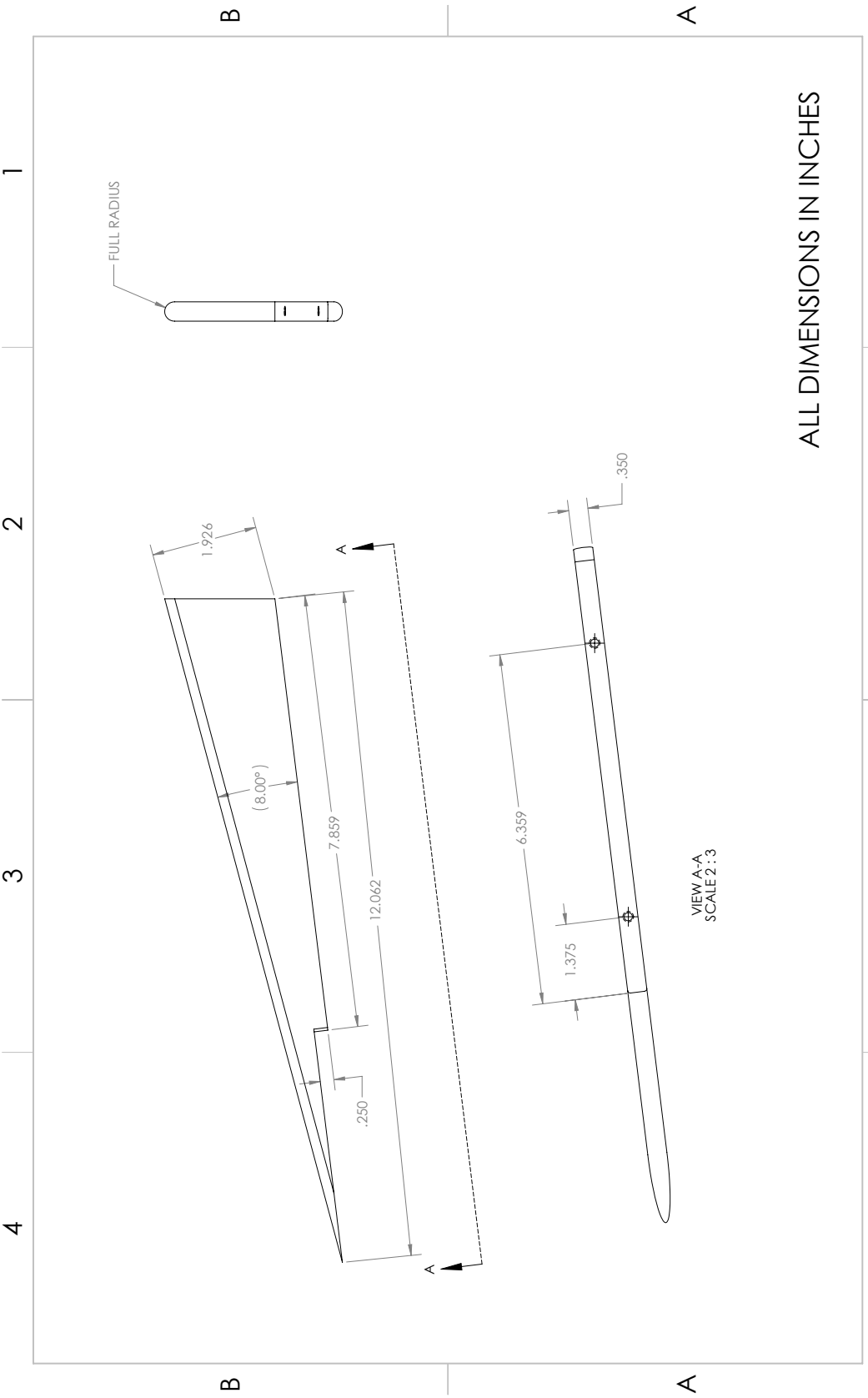
ALL DIMENSIONS IN INCHES
FULL RADIUS
1.926
(8.00°)
7.859
12.062
.250
A
A
.350
6.359
1.375
VIEW A-A
SCALE 2 : 3
1
2
3
4
B
A

A.2 Three-Fin Model

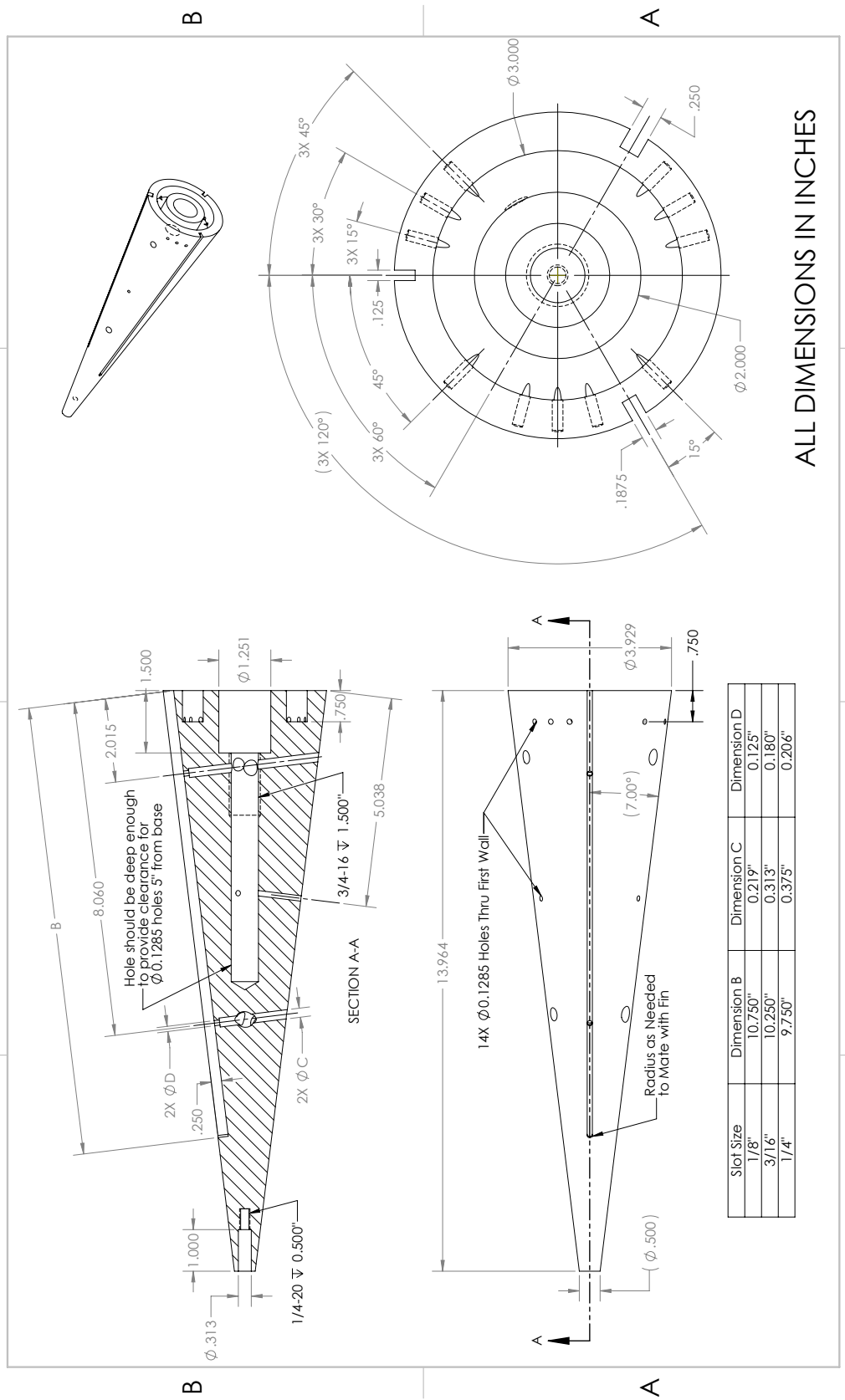

Slot Size	Dimension B	Dimension C	Dimension D
1/8"	10.750"	0.219"	0.125"
3/16"	10.250"	0.313"	0.180"
1/4"	9.750"	0.375"	0.206"

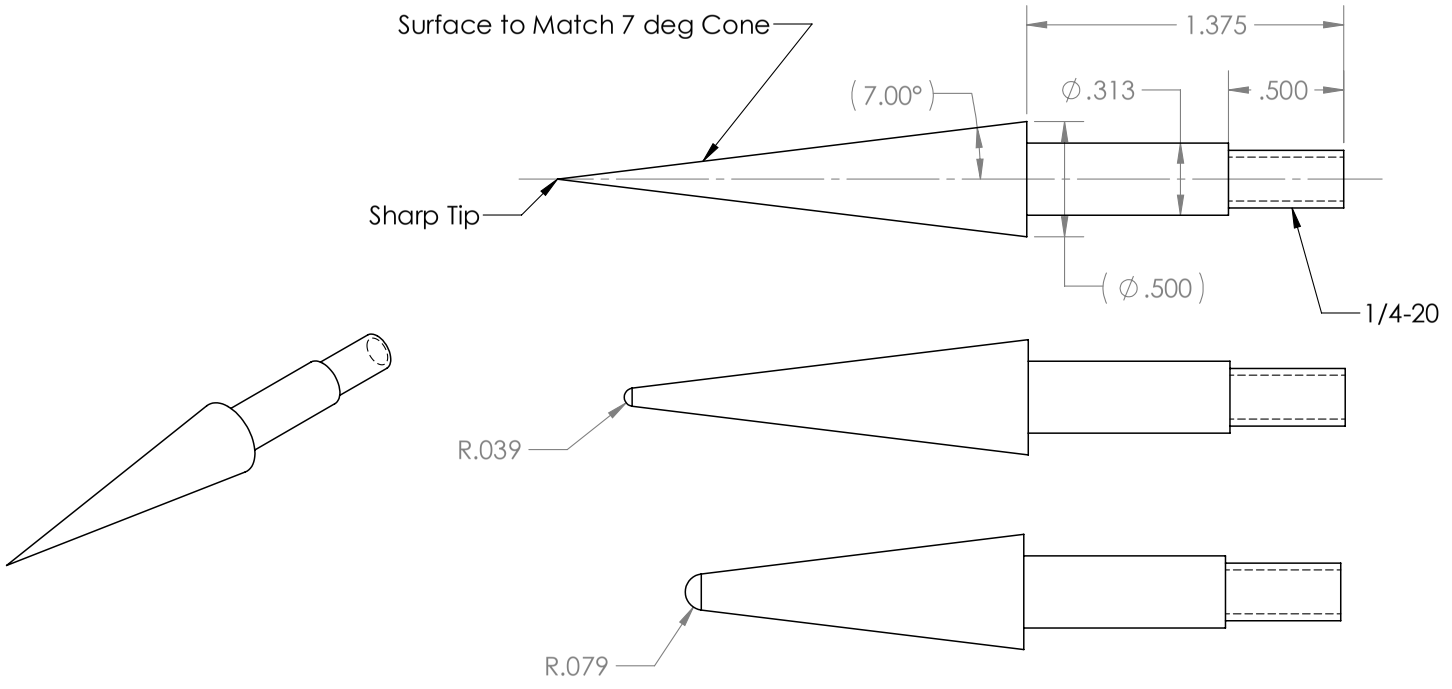

ALL DIMENSIONS IN INCHES

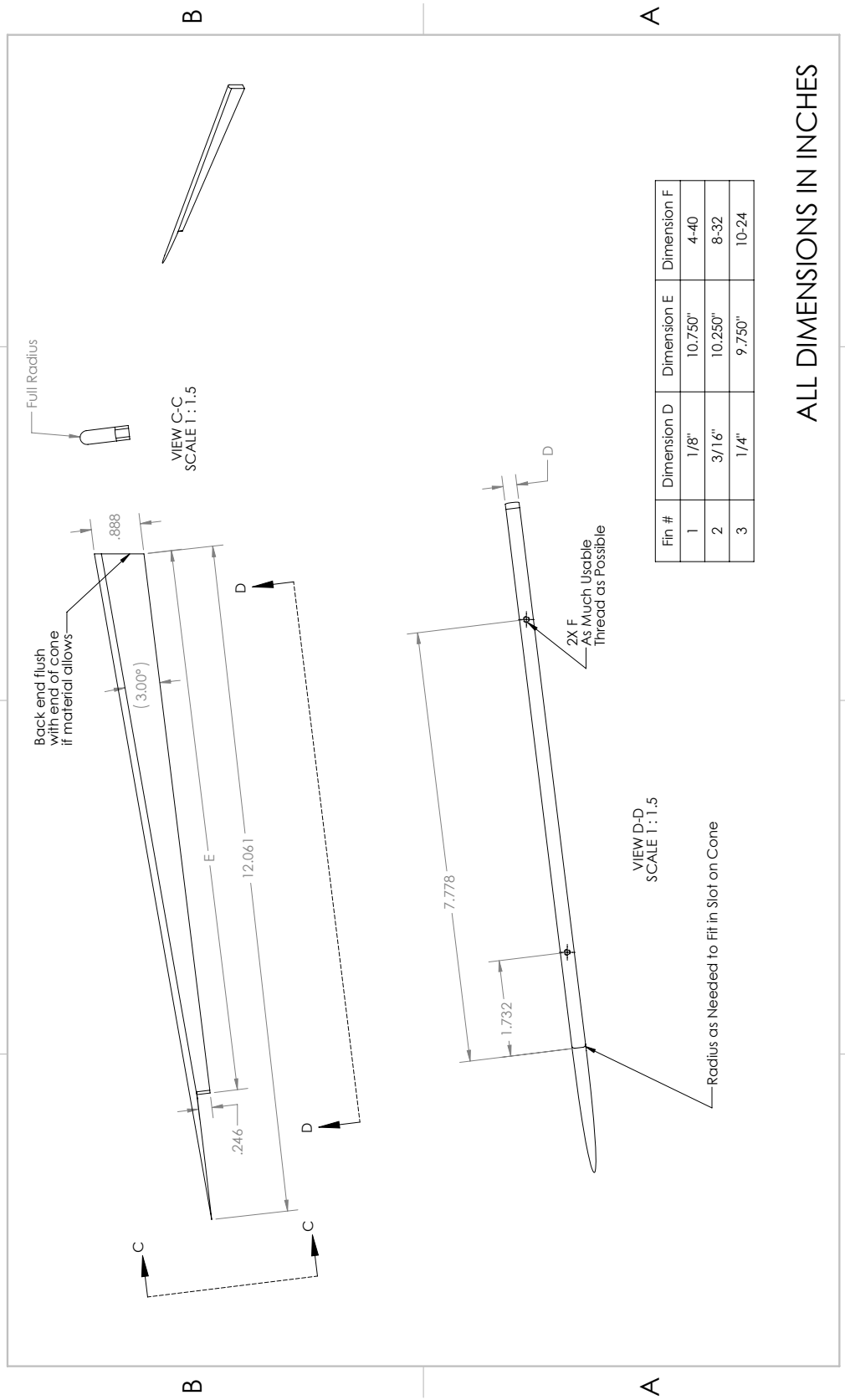
ALL DIMENSIONS IN INCHES
Full Radius
VIEW C-C
SCALE 1 : 1.5
.888
(3.00°)
E
12.061
.246
Back end flush
with end of cone
if material allows
D
C
VIEW D-D
SCALE 1 : 1.5
7.778
1.732
2X F
As Much Usable
Thread as Possible
Radius as Needed to Fit in Slot on Cone
Fin # | Dimension D | Dimension E | Dimension F
1 | 1/8" | 10.750" | 4-40
2 | 3/16" | 10.250" | 8-32
3 | 1/4" | 9.750" | 10-24

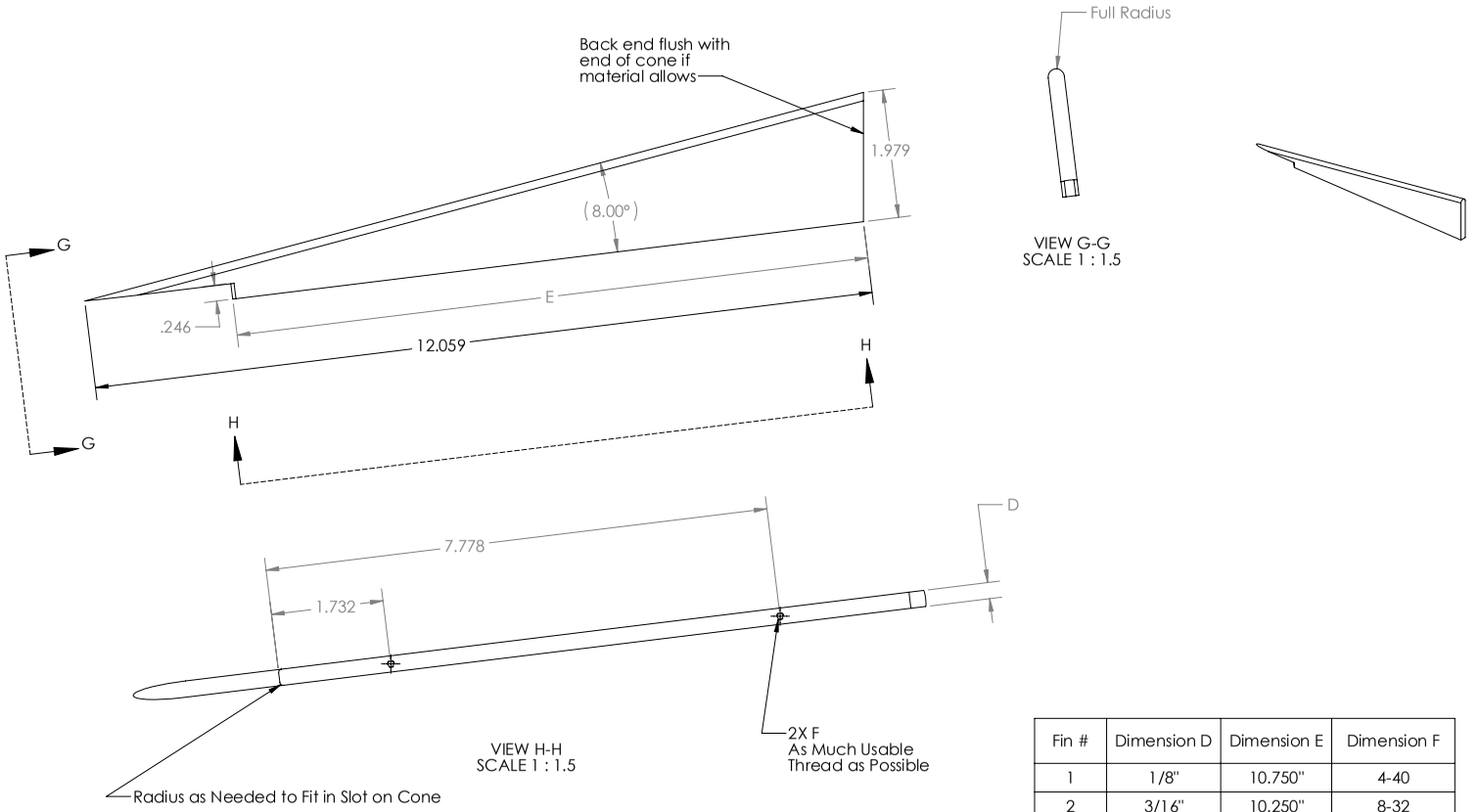

Fin #	Dimension D	Dimension E	Dimension F
1	1/8"	10.750"	4-40
2	3/16"	10.250"	8-32
3	1/4"	9.750"	10-24

ALL DIMENSIONS IN INCHES

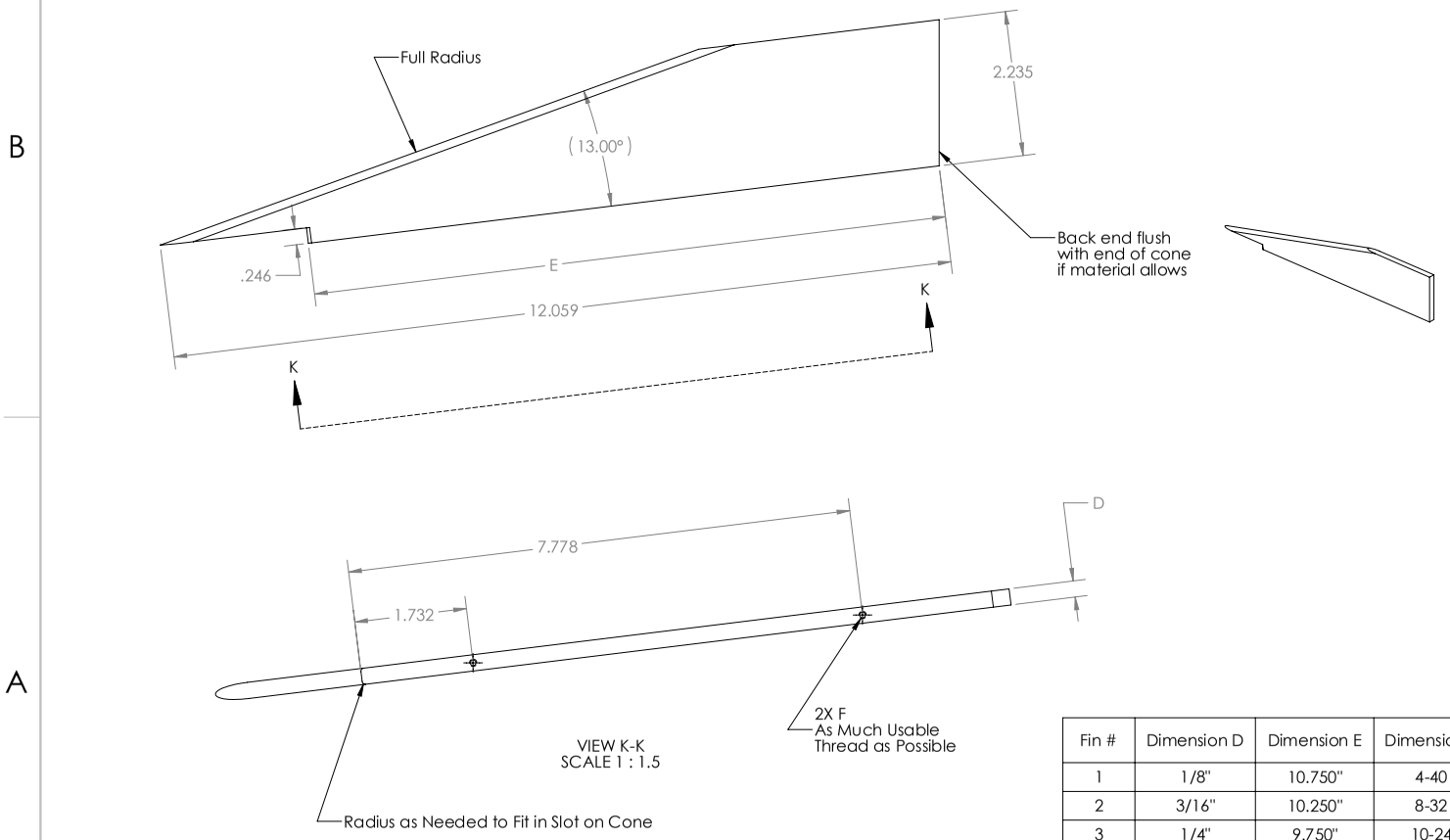

Fin #	Dimension D	Dimension E	Dimension F
1	1/8"	10.750"	4-40
2	3/16"	10.250"	8-32
3	1/4"	9.750"	10-24

ALL DIMENSIONS IN INCHES

B. Data Reduction Codes

B.1 PCB Code

```
%% Code to Process PCB Power Spectra
% By: Drew Turbeville
% Modified: 14 March 2017

clear all; clc; fclose all; close all;

entry = 7;
%%%%%%%Specify Main Folder File Path%%%%%%%
fin_cone_path = ['C:\Users\drewturbeville\Documents\Fin
   Cone\'];
path_to_Main = ['C:\Users\drewturbeville\Documents\Fin
   Cone\Entry ',num2str(entry),'\'];

%%%%%%%Grab Run Conditions and PCB Calibrations from Excel
   %%%%%%%
T0_init = xlsread([path_to_Main,'\Data_Processing.xlsx'],'
   RunLog','D2:D40'); %finds recorded initial stag temp
QN = xlsread([path_to_Main,'\Data_Processing.xlsx'],'
   RunLog','B2:B40'); %determines whether run was quiet or
    noisy
PCB_Cal = xlsread([path_to_Main,'\Data_Processing.xlsx'],'
   PCB_Calibrations','B3:B40'); %retrieves pcb
   calibrations
```

```
m = xlsread([fin_cone_path,'\Kulite_Calibration.xlsx'],['
   Entry ',num2str(entry)],'C2'); %kulite calibration
   slope
b = xlsread([fin_cone_path,'\Kulite_Calibration.xlsx'],['
   Entry ',num2str(entry)],'D2'); %kulite calibration y-
   intercept

%%%%%%%Specify whether figures should be by run (0) or by
   PCB (1)%%%%%%%
sel = 0;

i = 1;

% Enter the Desired Run Numbers
for Run_num = [3 3 3];
    % Enter the time in each run to process
    t2 = [1 2 3];

    % Reads in the contraction kulite data
    [Con_Kul,t1] = tekread(char(strcat(path_to_Main,'
       Tunnel_Conditions\Run',num2str(Run_num),'
       _Contraction.wfm')));

    % Calculate the initial stagnation pressure
    t_pre = round(1/(t1(2)-t1(1)))*.25; %finds time index
       roughly .25 seconds before burst
    P0_init = m*Con_Kul(t_pre)+b; %Kulite calibration

    % Sets Mach number to 6 if quiet and 5.8 if noisy
```

```
if QN(Run_num)==1
    M = 6;
else
    M = 5.8;
end

j = 1;

% Enter PCB Numbers For Processing
for PCB_num = [4 5 6];

    if sel == 1
        figNum = PCB_num;
    elseif sel == 0
        figNum = i;
    end

    PCB = num2str(PCB_num);
    Run = num2str(Run_num);
    filename_PCB = char(strcat(path_to_Main,'PCB_Data\
       Run',Run,'\Run',Run,'_PCB',PCB,'.wfm'));
    [Vall,t] = tekread(filename_PCB);
    Pall = 1000*Vall./PCB_Cal(PCB_num); % Converts
       voltage to pressure

    % Starting PCB Processing using Fast-Fourier
       Transforms
    % Program has been modified so sampling rate is
       read in from the
```

```
% PCB_Info file
% Find the offset from trigger
t_offset = -round(t(1)*100)/100;
sample_rate = round(1/(t(2)-t(1)));
data_offset = t_offset*sample_rate;
% The following is used to make sure that data is
   taken 0.5 seconds
% after the trigger of the oscilloscopes (time can
    be altered if
% necessary)
desired_time = t2(i); % In seconds
process_time = 0.1; % In seconds time to process
run_in = data_offset+desired_time*sample_rate; %In
    samples

time_index =  find(abs((t1-desired_time)/
   desired_time)<0.000000005);
P0 = m*Con_Kul(time_index)+b;
[Re_ft, Re_m, T0, mu] = Re_Calc(P0,P0_init,T0_init
   (Run_num),M);

Astart = run_in;

sample_length = sample_rate*process_time;
Aend   = sample_length + Astart; % Sets length of
   the sample window
A = Pall(Astart:Aend);    % Gets data to be
   analyzed
```

```
Freq_Reso = 2000;
WindowSize = sample_rate/Freq_Reso;
nfft = WindowSize;
PercentOverlap = nfft/2;

A_less_mean = A-mean(A);
A_norm = A_less_mean/(1.2449058E-03*P0);
[ppsd,fpsd] = pwelch(A_norm,WindowSize,
   PercentOverlap,nfft,sample_rate);
%%%%%%%%%%%%%%%%%%%%%%%%%Plotting
   %%%%%%%%%%%%%%%%%%%%%%%%%%%%%%%%%%

figure(figNum)
semilogy(fpsd/1000,ppsd)
hold on
xlim([0,500])
set(gca,'FontSize',12)

deg = [15 30 45];
if sel == 1
    if t2(i)<0
        Re{i} = sprintf('Run %d, Electronic Noise'
           ,entry*100+Run_num);
        hline = findobj(gcf,'type','line');
        set(hline(end),'LineStyle','--','Color','k
           ');
    else
        Re{i} = sprintf('Run %d, Re=%.2d/m',entry
           *100+Run_num,Re_m);
```

```
            end
            title(sprintf('PCB %d, %d%c from fin',PCB_num,
               deg(j),char(176)),'FontSize',18);
            legend(Re,'FontSize',12)
        elseif sel == 0
            Re{j} = sprintf('PCB %d',PCB_num);
        end

        xlabel('Frequency [kHz]','FontSize',18)
        ylabel('PSD (P''/P_{TM})^2/Hz','FontSize',18)

        j = j+1;
    end

    if sel == 0
        if t2(i)<0
            title(sprintf('Run %d, Electronic Noise',entry
               *100+Run_num),'FontSize',18);
        else
            title(sprintf('Run %d, Re = %.2d/m, P_{0} =
               %.1f psia',entry*100+Run_num,Re_m,P0),'
               FontSize',18);
        end
        legend(Re,'FontSize',12)
    end

    i = i+1;
end
```

B.2 TSP Slicing Code

```
%% inputs
ax_pos = 14.7; %inches
tilt = 30; % degrees
thck = .125; %inches -- nose radius
crnAng = 180/pi*asin(thck/(2*ax_pos*tan(7*pi/180))); %
   degrees
hgt = 2.2; %inches

% corner coordinates
crnr = [1551 410;
        1340 436;
        1150 460;
        921 491;
        642 524;
        412 556];

% coordinates of the PCBs at 15.25 in and their degrees
pcb = [1464 411 crnAng;
 1469 450 15;
       1475 496 30;
       1482 559 45
         1490 628 60];

% schmidt-boelter coordinate
sb = [939 628];

% coordinates of aft edge of fin
```

```
fin = [1555 386;
       1559 345;
       1565 305;
       1570 258];


%% unwrap cone
% find nosetip x-pixel
nstp = round(sb(1)-11*.0254*pix_per_m); %assumes 60 deg
   ray is level

figure(3)
hold on
plot([1 1611],[sb(2) sb(2)],'y--','LineWidth',3)

% corner pixels
P2 = polyfit(crnr(:,1),crnr(:,2),1);
crnrY = round(P2(1)*(1:1611)+P2(2));

figure(3)
hold on
plot(1:10:1611,crnrY(1:10:1611),'y--','LineWidth',3)

% find azimuthal angle versus 2d angle
tdang = zeros(1,5);
for i=1:5
```

```
    tdang(i) = -180/pi*atan((pcb(i,2)-sb(2))/(pcb(i,1)-
       nstp));

end

P3 = polyfit(pcb(:,3)',tdang,2);
az = linspace(crnAng,60);
ang = P3(1)*(az).^2+P3(2)*(az)+P3(3);
L = ax_pos*0.0254*pix_per_m;
x_pix = round(L*cos(pi/180*ang)+nstp);
y_pix = round(-L*sin(pi/180*ang)+sb(2));

for j=1:length(az)
    figure(3)
    hold on
    plot(round(L*cos(pi/180*ang(j)))+nstp,round(-L*sin(pi
       /180*ang(j)))+sb(2),'r*')
end
figure(5)
hold on
plot(xaxis(round(L*cos(pi/180*ang))+nstp),-yaxis(round(-L*
   sin(pi/180*ang))+sb(2)),'r','LineWidth',2)

%% unwrap the fin (adjust for tilt)

P4 = polyfit(fin(:,2),fin(:,1),1);
ydel = .02; %inches
H = hgt*cosd(tilt)*pix_per_m*.0254;
```

```
yfin = [round((y_pix(1)-H):(ydel*.0254*pix_per_m):y_pix(1)
   ) y_pix(1)];
xint = x_pix(1) - P4(1)*y_pix(1);
xfin = round(yfin*P4(1)+xint);

figure(3)
hold on
plot(xfin,yfin,'g*')
figure(5)
hold on
plot(xaxis(xfin),-yaxis(yfin),'r','LineWidth',2)

%% grab heat xfer values and average

%cone
Qa = 0;
for k=1:length(x_pix)

    Qa(k) = mean(mean(QMatrix((y_pix(k)-1):(y_pix(k)+1),(
       x_pix(k)-1):(x_pix(k)+1))));

end

%fin
Qy = 0;
for r=1:length(xfin)

    Qy(r) = mean(mean(QMatrix((yfin(r)-1):(yfin(r)+1),(
       xfin(r)-1):(xfin(r)+1))));
```

```
end
fhght = sqrt((xfin-xfin(1)).^2+(yfin-yfin(1)).^2)/
   pix_per_m/.0254/cosd(tilt); %inches

figure(6)
subplot(1,2,1)
plot(az,Qa)
hold on
set(gca,'xdir','reverse')
xlabel('Azimuth [deg]')
ylabel('Heat Transfer [kW/m^2]')
title('Cone Surface')
axis([0 60 0 6])
subplot(1,2,2)
plot(fhght,flip(Qy))
hold on
axis([0 2.2 0 6])
xlabel('Fin Height [in]')
ylabel('Heat Transfer [kW/m^2]')
title('Fin Surface')

save('C:\Users\drewturbeville\Documents\TSP Code\temp\
   Run518','az','Qa','fhght','Qy')
```

C. Sensor Calibrations and Locations by Entry

C.1 Entry 1

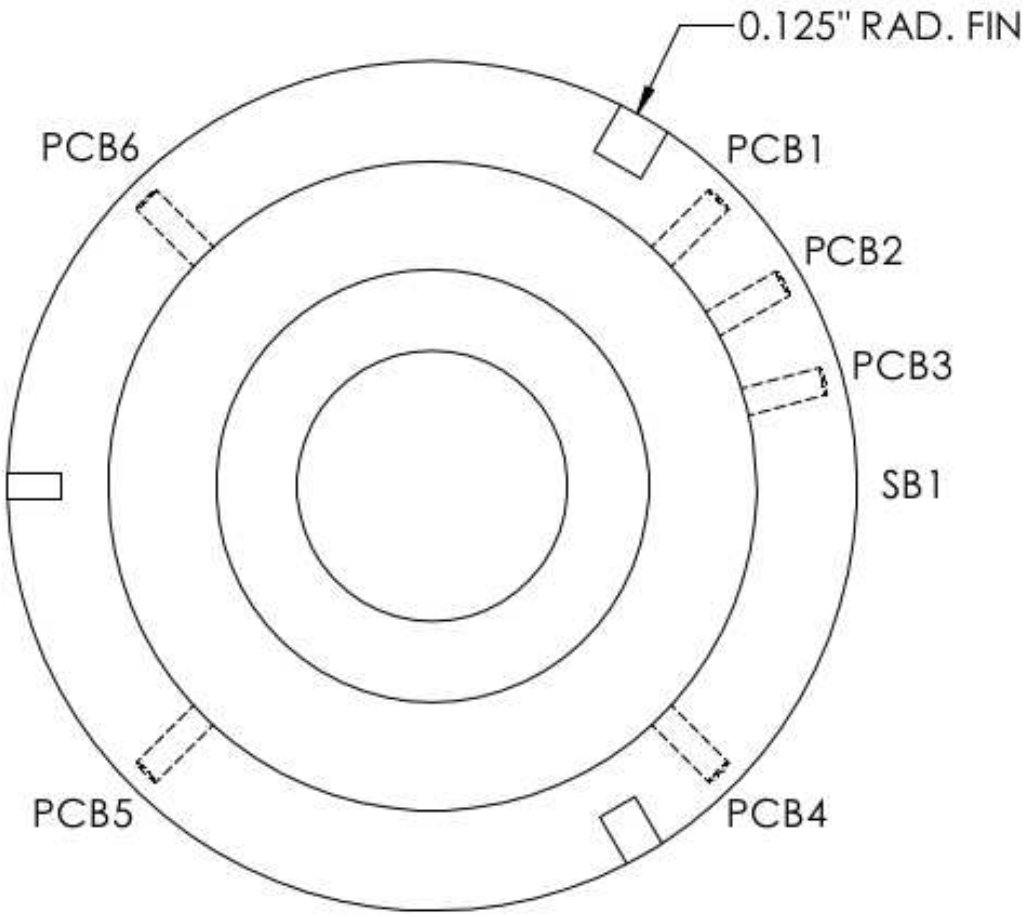

Figure C.1. Entry 1 PCB and SB locations. View from back end of cone.

Table C.1. Entry 1 sensor positions and sampling rates.

Sensor Code	Serial Number	Position	Axial Station	Sampling Rate
SB1	191193	60° from 1/8” radius fin	x = 11 in	200 kHz
PCB1	6601	15° from 1/8” radius fin	x = 15.75 in	5 MHz
PCB2	6773	30° from 1/8” radius fin	x = 15.75 in	5 MHz
PCB3	6613	45° from 1/8” radius fin	x = 15.75 in	5 MHz
PCB4	6662	90° from PCB1	x = 15.75 in	5 MHz
PCB5	6884	90° from PCB4	x = 15.75 in	5 MHz
PCB6	6842	90° from PCB5	x = 15.75 in	5 MHz

Table C.2. Entry 1 sensor calibrations.

Sensor Code	Sensor Type	Serial Number	Calibration
SB1	8-1-0.25-48-20835TBS Schmidt-Boelter	191193	1.486 $\frac{kW}{m^2 mV}$
PCB1	PCB132A31	6601	181.4 $\frac{mV}{psia}$
PCB2	PCB132A31	6773	111.7 $\frac{mV}{psia}$
PCB3	PCB132A31	6613	172.0 $\frac{mV}{psia}$
PCB4	PCB132A31	6662	158.0 $\frac{mV}{psia}$
PCB5	PCB132A31	6884	161.3 $\frac{mV}{psia}$
PCB6	PCB132A31	6842	120.0 $\frac{mV}{psia}$

C.2 Entry 2

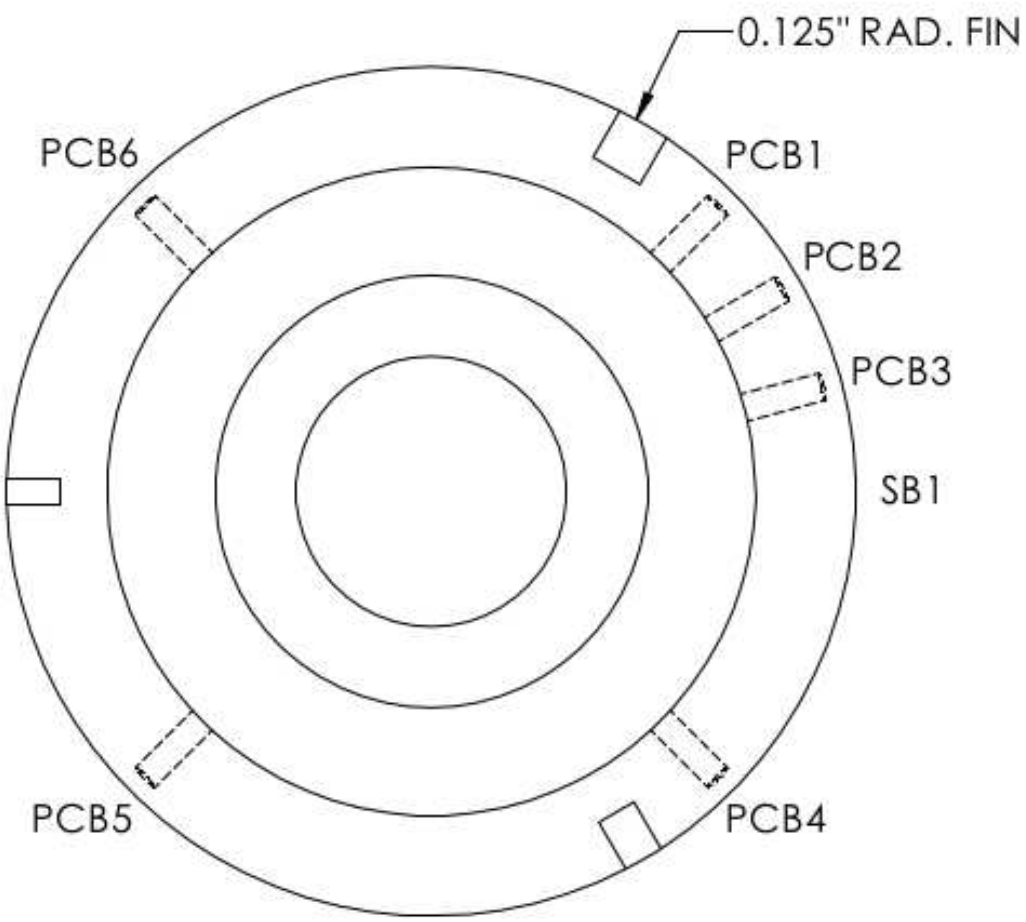

Figure C.2. Entry 2 PCB and SB locations. View from back end of cone.

Table C.3. Entry 2 sensor positions and sampling rates.

Sensor Code	Serial Number	Position	Axial Station	Sampling Rate
SB1	191791	60° from 1/8” radius fin	x = 11 in	20 kHz
PCB1	6896	15° from 1/8” radius fin	x = 15.75 in	5 MHz
PCB2	7313	30° from 1/8” radius fin	x = 15.75 in	5 MHz
PCB3	6661	45° from 1/8” radius fin	x = 15.75 in	5 MHz
PCB4	6879	90° from PCB1	x = 15.75 in	5 MHz
PCB5	7090	90° from PCB4	x = 15.75 in	5 MHz
PCB6	7318	90° from PCB5	x = 15.75 in	5 MHz

Table C.4. Entry 2 sensor calibrations.

Sensor Code	Sensor Type	Serial Number	Calibration
SB1	8-1-0.25-48-20835TBS Schmidt-Boelter	191791	1.667 $\frac{kW}{m^2 mV}$
PCB1	PCB132A31	6896	141.9 $\frac{mV}{psia}$
PCB2	PCB132A31	7313	142.9 $\frac{mV}{psia}$
PCB3	PCB132A31	6661	163.8 $\frac{mV}{psia}$
PCB4	PCB132A31	6879	105.3 $\frac{mV}{psia}$
PCB5	PCB132A31	7090	157.4 $\frac{mV}{psia}$
PCB6	PCB132A31	7318	180.0 $\frac{mV}{psia}$

C.3 Entry 3

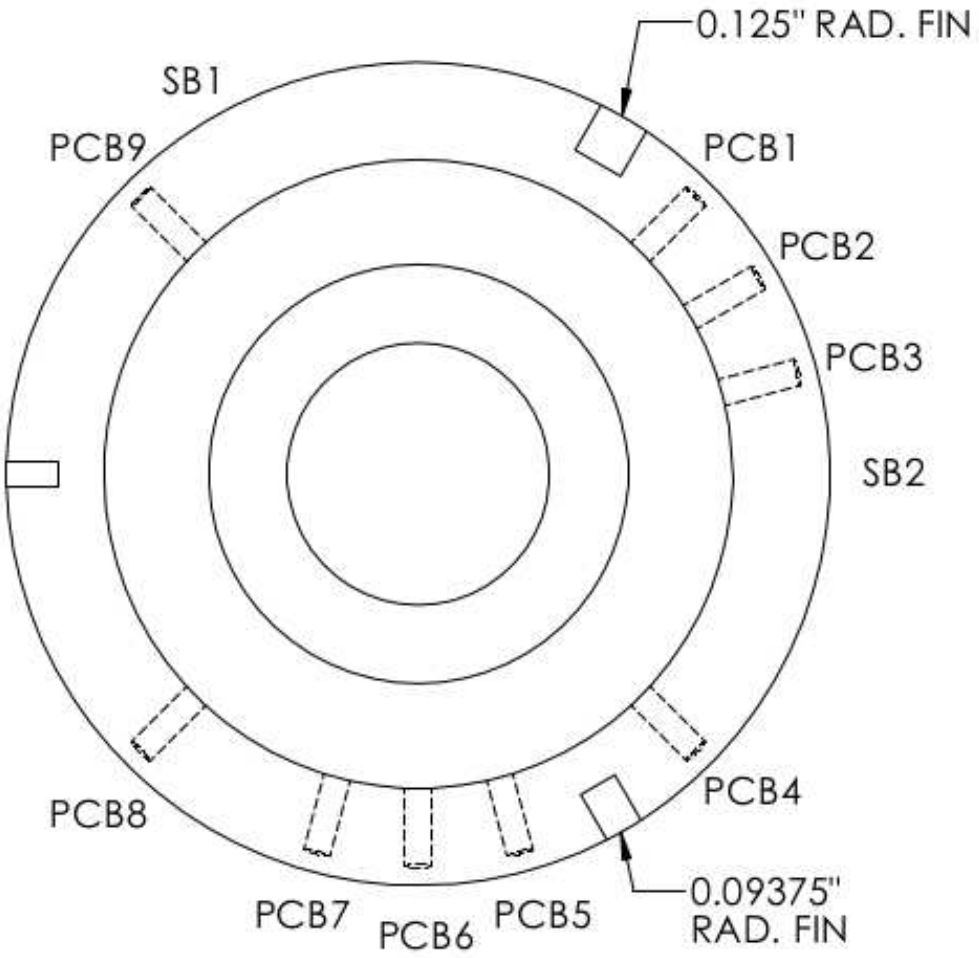

Figure C.3. Entry 3 PCB and SB locations. View from back end of cone.

Table C.5. Entry 3 sensor positions and sampling rates.

Sensor Code	Serial Number	Position	Axial Station	Sampling Rate
SB1	191193	60° from 1/8” radius fin	x = 11 in	20 kHz
SB2	191791	60° from 1/8” radius fin	x = 11 in	20 kHz
PCB1	7506	15° from 1/8” radius fin	x = 15.75 in	2 MHz
PCB2	7502	30° from 1/8” radius fin	x = 15.75 in	2 MHz
PCB3	7514	45° from 1/8” radius fin	x = 15.75 in	2 MHz
PCB4	7503	90° from PCB1	x = 15.75 in	2 MHz
PCB5	7513	15° from 3/32”” radius fin	x = 15.75 in	2 MHz
PCB6	7512	30° from 3/32”” radius fin	x = 15.75 in	2 MHz
PCB7	7515	45° from 3/32”” radius fin	x = 15.75 in	2 MHz
PCB8	7507	90° from PCB4	x = 15.75 in	2 MHz
PCB9	7499	90° from PCB8	x = 15.75 in	2 MHz

Table C.6. Entry 3 sensor calibrations.

Sensor Code	Sensor Type	Serial Number	Calibration
SB1	8-1-0.25-48-20835TBS Schmidt-Boelter	191193	1.486 $\frac{kW}{m^2 mV}$
SB2	8-1-0.25-48-20835TBS Schmidt-Boelter	191791	1.667 $\frac{kW}{m^2 mV}$
PCB1	PCB132A31	7506	165.7 $\frac{mV}{psia}$
PCB2	PCB132A31	7502	166.3 $\frac{mV}{psia}$
PCB3	PCB132A31	7514	165.3 $\frac{mV}{psia}$
PCB4	PCB132A31	7503	173.3 $\frac{mV}{psia}$
PCB5	PCB132A31	7513	179.8 $\frac{mV}{psia}$
PCB6	PCB132A31	7512	171.2 $\frac{mV}{psia}$
PCB7	PCB132A31	7515	173.9 $\frac{mV}{psia}$
PCB8	PCB132A31	7507	151.4 $\frac{mV}{psia}$
PCB9	PCB132A31	7499	157.5 $\frac{mV}{psia}$

C.4 Entry 5

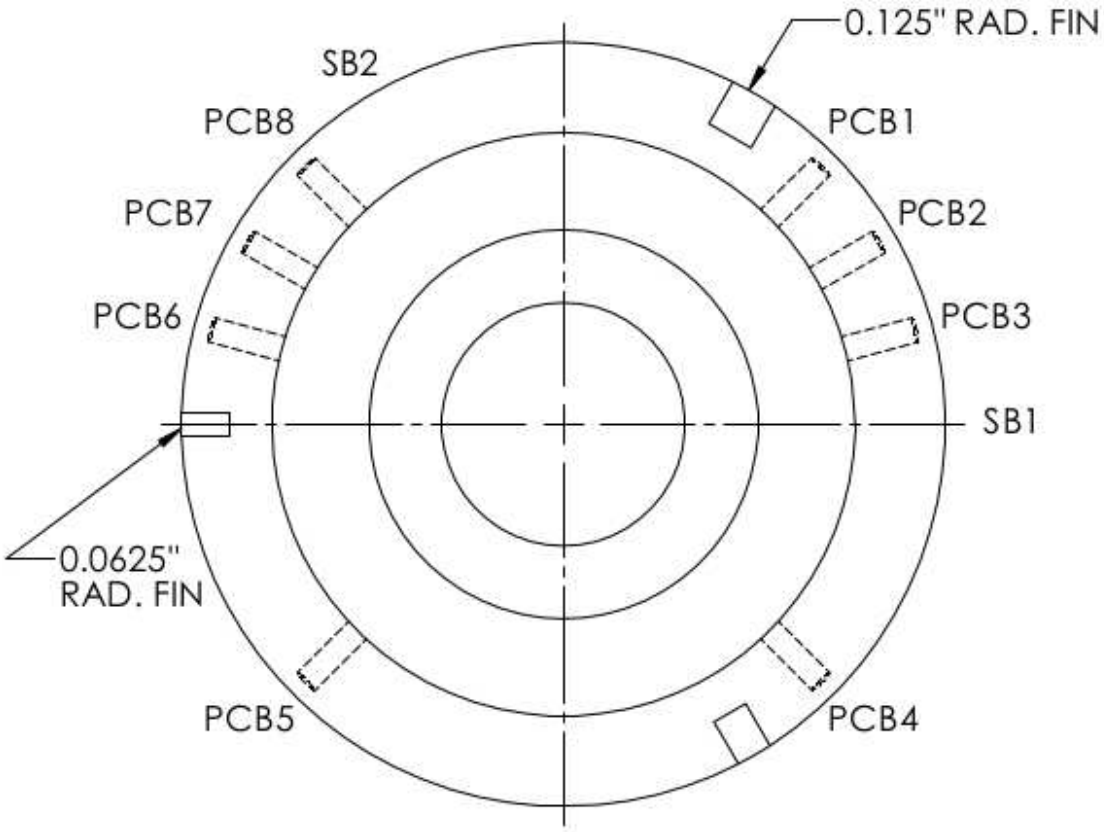

Figure C.4. Entry 5 PCB and SB locations. View from back end of cone.

Table C.7. Entry 5 sensor positions and sampling rates.

Sensor Code	Serial Number	Position	Axial Station	Sampling Rate
SB1	191193	60° from 1/8” radius fin	x = 11 in	20 kHz
SB2	191791	60° from 1/8” radius fin	x = 11 in	20 kHz
PCB1	7506	15° from 1/8” radius fin	x = 15.75 in	2 MHz
PCB2	7515	30° from 1/8” radius fin	x = 15.75 in	2 MHz
PCB3	7512	45° from 1/8” radius fin	x = 15.75 in	2 MHz
PCB4	7514	90° from PCB1	x = 15.75 in	2 MHz
PCB5	7502	90° from PCB4	x = 15.75 in	2 MHz
PCB6	7503	15° from 1/16”” radius fin	x = 15.75 in	2 MHz
PCB7	7507	30° from 1/16”” radius fin	x = 15.75 in	2 MHz
PCB8	7499	45° from 1/16”” radius fin	x = 15.75 in	2 MHz

Table C.8. Entry 5 sensor calibrations.

Sensor Code	Sensor Type	Serial Number	Calibration
SB1	8-1-0.25-48-20835TBS Schmidt-Boelter	191193	1.486 $\frac{kW}{m^2 mV}$
SB2	8-1-0.25-48-20835TBS Schmidt-Boelter	191791	1.667 $\frac{kW}{m^2 mV}$
PCB1	PCB132A31	7506	165.7 $\frac{mV}{psia}$
PCB2	PCB132A31	7515	173.9 $\frac{mV}{psia}$
PCB3	PCB132A31	7512	171.2 $\frac{mV}{psia}$
PCB4	PCB132A31	7514	165.3 $\frac{mV}{psia}$
PCB5	PCB132A31	7502	166.3 $\frac{mV}{psia}$
PCB6	PCB132A31	7503	173.3 $\frac{mV}{psia}$
PCB7	PCB132A31	7507	151.4 $\frac{mV}{psia}$
PCB8	PCB132A31	7499	157.5 $\frac{mV}{psia}$

C.5 Entry 6

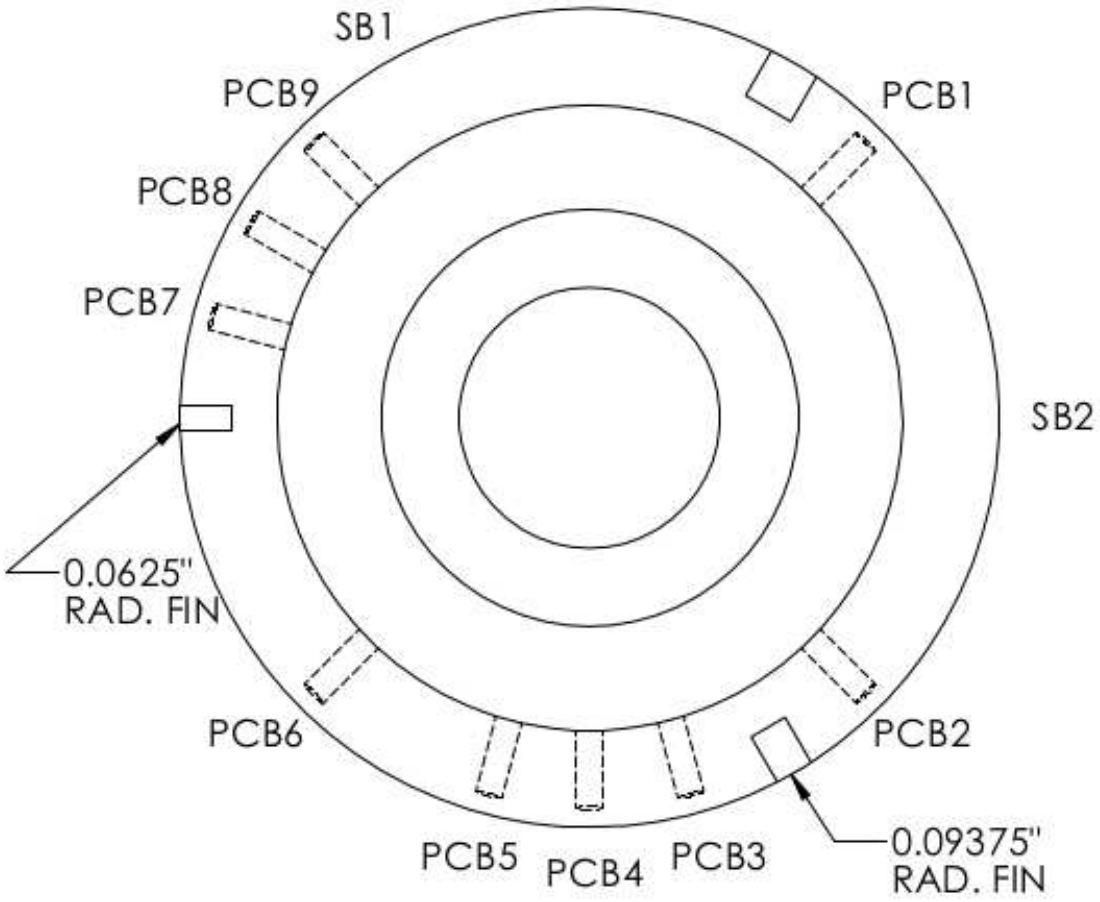

Figure C.5. Entry 6 PCB and SB locations. View from back end of cone.

Table C.9. Entry 6 sensor positions and sampling rates.

Sensor Code	Serial Number	Position	Axial Station	Sampling Rate
SB1	191193	60° from 1/16” radius fin	x = 11 in	20 kHz
SB2	191791	60° from 3/32” radius fin	x = 11 in	20 kHz
PCB1	7502	90° from PCB2	x = 15.75 in	2 MHz
PCB2	7506	90° from PCB6	x = 15.75 in	2 MHz
PCB3	7507	15° from 3/32”” radius fin	x = 15.75 in	2 MHz
PCB4	7503	30° from 3/32”” radius fin	x = 15.75 in	2 MHz
PCB5	7512	45° from 3/32”” radius fin	x = 15.75 in	2 MHz
PCB6	7499	90° from PCB9	x = 15.75 in	2 MHz
PCB7	7513	15° from 1/16”” radius fin	x = 15.75 in	2 MHz
PCB8	7514	30° from 1/16”” radius fin	x = 15.75 in	2 MHz
PCB9	7515	45° from 1/16”” radius fin	x = 15.75 in	2 MHz

Table C.10. Entry 6 sensor calibrations.

Sensor Code	Sensor Type	Serial Number	Calibration
SB1	8-1-0.25-48-20835TBS Schmidt-Boelter	191791	1.667 $\frac{kW}{m^2 mV}$
SB2	8-1-0.25-48-20835TBS Schmidt-Boelter	191193	1.486 $\frac{kW}{m^2 mV}$
PCB1	PCB132A31	7502	166.3 $\frac{mV}{psia}$
PCB2	PCB132A31	7506	165.7 $\frac{mV}{psia}$
PCB3	PCB132A31	7507	151.4 $\frac{mV}{psia}$
PCB4	PCB132A31	7503	173.3 $\frac{mV}{psia}$
PCB5	PCB132A31	7512	171.2 $\frac{mV}{psia}$
PCB6	PCB132A31	7499	157.5 $\frac{mV}{psia}$
PCB7	PCB132A31	7513	179.8 $\frac{mV}{psia}$
PCB8	PCB132A31	7514	165.3 $\frac{mV}{psia}$
PCB9	PCB132A31	7515	173.9 $\frac{mV}{psia}$

C.6 Entry 7

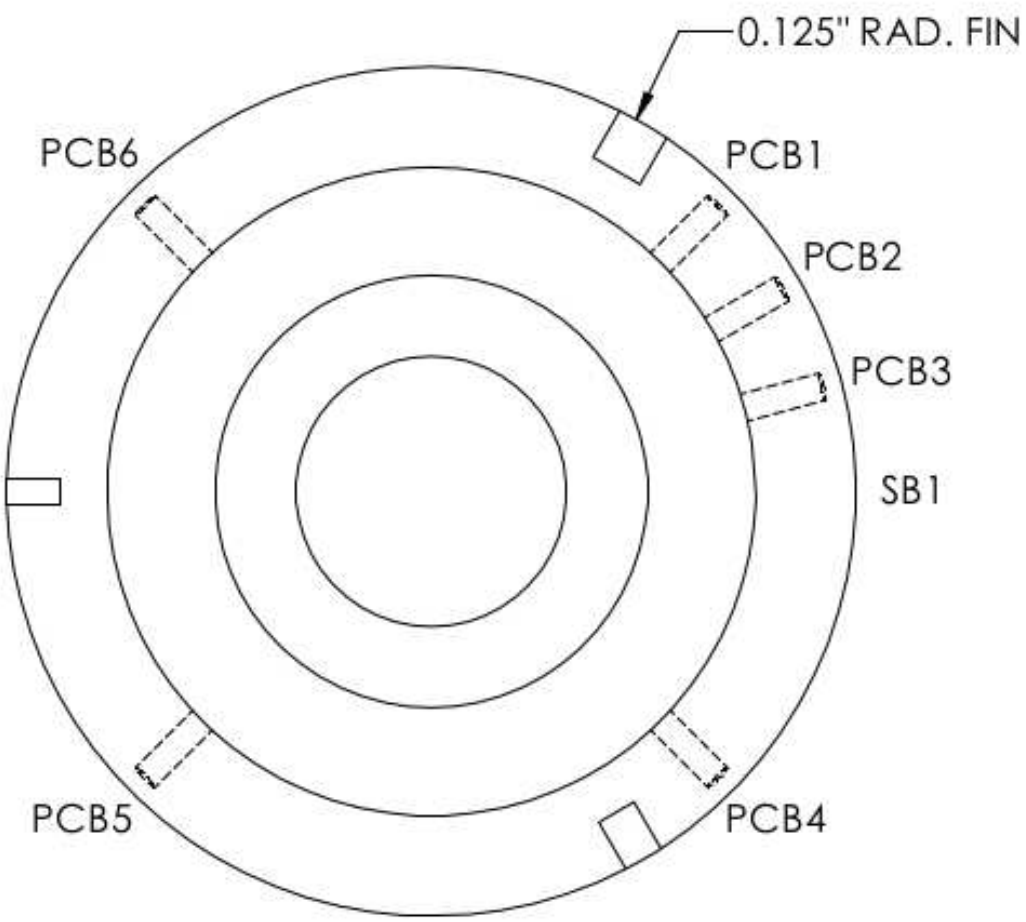

Figure C.6. Entry 7 PCB and SB locations. View from back end of cone.

Table C.11. Entry 7 sensor positions and sampling rates.

Sensor Code	Serial Number	Position	Axial Station	Sampling Rate
SB1	191791	60° from 1/8” radius fin	x = 11 in	20 kHz
PCB1	7503	15° from 1/8” radius fin	x = 15.75 in	2 MHz
PCB2	7286	30° from 1/8” radius fin	x = 15.75 in	2 MHz
PCB3	7309	45° from 1/8” radius fin	x = 15.75 in	2 MHz
PCB4	7492	90° from PCB1	x = 15.75 in	2 MHz
PCB5	7496	90° from PCB4	x = 15.75 in	2 MHz
PCB6	7506	90° from PCB5	x = 15.75 in	2 MHz

Table C.12. Entry 7 sensor calibrations.

Sensor Code	Sensor Type	Serial Number	Calibration
SB1	8-1-0.25-48-20835TBS Schmidt-Boelter	191791	1.667 $\frac{kW}{m^2 mV}$
PCB1	PCB132A31	7503	173.3 $\frac{mV}{psia}$
PCB2	PCB132A31	7286	148.0 $\frac{mV}{psia}$
PCB3	PCB132A31	7309	160.0 $\frac{mV}{psia}$
PCB4	PCB132A31	7492	153.8 $\frac{mV}{psia}$
PCB5	PCB132A31	7496	167.6 $\frac{mV}{psia}$
PCB6	PCB132A31	7506	165.7 $\frac{mV}{psia}$

D. Tunnel Conditions and Model Configurations

Table D.1. Entry 0 run matrix.

Run	$P_{0,i}$ [psia]	$T_{0,i}$ [°C]	P_0 [psia] @ 1 s	Re [/m] @ 1 s	R_{NT} [mm]	Λ [°]	R_{LE} [in]
028	120.0	153.4	111.9	8.69 x 10^6	Sharp	75	0.175
032	109.8	150.4	104.7	8.69 x 10^6	Sharp	75	0.175

Table D.2. Entry 1 run matrix.

Run	$P_{0,i}$ [psia]	$T_{0,i}$ [°C]	P_0 [psia] @ 1 s	Re [/m] @ 1 s	R_{NT} [mm]	Λ [°]	R_{LE} [in]
109	170.5	151.1	157.7	12.4 x 10^6	Sharp	75	1/8

Table D.3. Entry 2 run matrix.

Run	$P_{0,i}$ [psia]	$T_{0,i}$ [°C]	P_0 [psia] @ 1 s	Re [/m] @ 1 s	R_{NT} [mm]	Λ [°]	R_{LE} [in]
231	111.1	151.5	105.1	8.23 x 10^6	Sharp	70	1/8

Table D.4. Entry 3 run matrix.

Run	$P_{0,i}$ [psia]	$T_{0,i}$ [°C]	P_0 [psia] @ 1 s	Re [/m] @ 1 s	R_{NT} [mm]	Λ [°]	R_{LE} [in]
314	169.7	157.6	105.1	12.1 x 10^6	Sharp	75	1/8
316	140.0	130.4	105.1	10.1 x 10^6	Sharp	75	1/8
321	140.0	158.5	130.6	9.97 x 10^6	Sharp	75	1/8

Table D.5. Entry 5 run matrix.

Run	$P_{0,i}$ [psia]	$T_{0,i}$ [°C]	P_0 [psia] @ 1 s	Re [/m] @ 1 s	R_{NT} [mm]	Λ [°]	R_{LE} [in]
508	100.4	154.7	93.2	7.23 x 10^6	2	75	1/8
518	113.8	149.9	105.8	8.36 x 10^6	Sharp	70	1/16
520	101.5	152.6	94.3	7.37 x 10^6	Sharp	70	1/16

Table D.6. Entry 6 run matrix.

Run	$P_{0,i}$ [psia]	$T_{0,i}$ [°C]	P_0 [psia] @ 1 s	Re [/m] @ 1 s	R_{NT} [mm]	Λ [°]	R_{LE} [in]
605	126.7	156.2	118.9	9.16 x 10^6	Sharp	75	3/32
608	116.1	152.0	109.1	8.53 x 10^6	Sharp	75	3/32
609	99.3	160.8	93.1	7.04 x 10^6	Sharp	75	3/32

Table D.7. Entry 7 run matrix.

Run	$P_{0,i}$ [psia]	$T_{0,i}$ [°C]	P_0 [psia] @ 1 s	Re [/m] @ 1 s	R_{NT} [mm]	Λ [°]	R_{LE} [in]
703	113.2	156.5	105.6	8.12 x 10^6	Sharp	75	1/8
705	94.0	154.3	87.8	6.80 x 10^6	Sharp	75	1/8
706	82.9	153.5	77.3	6.02 x 10^6	Sharp	75	1/8
707	103.2	153.4	96.1	7.49 x 10^6	Sharp	75	1/8
709	119.6	154.2	111.5	8.67 x 10^6	1	75	1/8
711	101.2	154.2	94.3	7.32 x 10^6	1	75	1/8
715	127.2	157	118.7	9.12 x 10^6	2	75	1/8
719	95.6	152.2	89.2	6.98 x 10^6	Sharp	70	1/8
724	93.6	155.7	87.4	6.75 x 10^6	1	70	1/8
729	93.0	154.5	86.8	6.74 x 10^6	2	70	1/8